

**A LABORATORY STUDY OF DEPOSIT REMOVAL
BY DEBONDING AND ITS APPLICATION TO
FIRESIDE DEPOSITS IN
KRAFT RECOVERY BOILERS**

By

Seyed Abdolreza Ebrahimi-Sabet

A thesis submitted in conformity with the requirements

For the degree of Philosophy Doctorate (Ph.D.)

Department of Chemical Engineering and Applied Chemistry

University of Toronto

© Copyright by Seyed Abdolreza Ebrahimi-Sabet 2001



National Library
of Canada

Acquisitions and
Bibliographic Services

395 Wellington Street
Ottawa ON K1A 0N4
Canada

Bibliothèque nationale
du Canada

Acquisitions et
services bibliographiques

395, rue Wellington
Ottawa ON K1A 0N4
Canada

Your file Votre référence

Our file Notre référence

The author has granted a non-exclusive licence allowing the National Library of Canada to reproduce, loan, distribute or sell copies of this thesis in microform, paper or electronic formats.

The author retains ownership of the copyright in this thesis. Neither the thesis nor substantial extracts from it may be printed or otherwise reproduced without the author's permission.

L'auteur a accordé une licence non exclusive permettant à la Bibliothèque nationale du Canada de reproduire, prêter, distribuer ou vendre des copies de cette thèse sous la forme de microfiche/film, de reproduction sur papier ou sur format électronique.

L'auteur conserve la propriété du droit d'auteur qui protège cette thèse. Ni la thèse ni des extraits substantiels de celle-ci ne doivent être imprimés ou autrement reproduits sans son autorisation.

0-612-58923-4

Canada

A Laboratory Study of Deposit Removal by Debonding and its Application to Fireside Deposits in Kraft Recovery Boilers

Doctor of Philosophy 2001

Seyed Abdolreza Ebrahimi-Sabet

Department of Chemical Engineering and Applied Chemistry

University of Toronto

ABSTRACT

The accumulation of fireside deposits on heat exchange surfaces in a kraft recovery boiler drastically reduces the boiler thermal performance, restricts the flue gas flow, and in severe cases plugs the flue gas passages leading to unscheduled boiler shutdowns for cleaning. High-pressure steam sootblower jets are used to remove these deposits.

Deposits may be brittle or "plastic", depending on their temperature, and may be removed by sootblowers by two main mechanisms: brittle fracture and debonding. Brittle fracture has been previously studied and applies only to brittle and low-strength deposits. Debonding is likely to be the main mechanism by which strong deposits are removed by breaking the weak bond between the deposit and the tube surface. Deposit removal by a debonding mechanism is the main subject studied in this thesis.

To study the effects of aerodynamic drag and lift forces and flow induced vibrations on deposit debonding, the instantaneous drag and lift forces generated by a supersonic jet impinging on artificial deposits were measured in laboratory experiments. By numerical analysis, the fluctuation components of the drag and lift forces were decoupled from the flow-induced vibrations.

Results showed that the lift force fluctuations and flow-induced vibrations acting on deposits increased and reached maxima at a distance of about 45-50 nozzle diameters downstream. The flow-induced vibrations were found to be much larger in the lateral direction than in the flow direction. These vibrations increase the lift force fluctuations by a maximum factor of $0.872/\beta^{0.5}$, where β is the damping coefficient of the tube-deposit assembly. This is in good agreement with the results of the experiments, where the fluctuating lift forces were observed to be as effective as the mean drag force in removing artificial deposits.

An analysis of the dimensionless power spectra of lift forces exerted on cylindrical deposits showed a high degree of similarity under a broad range of operating conditions. The information can be used to estimate the power spectra of lift forces exerted on deposits in full-scale boilers. The results would provide a basis for estimating the role of vibration in deposit removal in full-scale boilers.

To my late parents,

Azzam and Fazlollah,

who have never "abondened" me.

abandoned

*for quite a long time
my green hands have turned yellow
wilted flowers have grown in my heart
my mind has had just frozen meats
and I cannot find food
in the garden or sky*

*I am too tired to trim shrubs and hedges
no one shovels the soil
new clothes are still in moth-balls
old newspapers are all over the floor
and I have lost interest in my mailbox*

*the alarm clock has lost its voice
the scarecrow has lost its dignity
while no bird still builds a nest
in the weeping willow*

*I give up
hang my soul in the closet
and close the door to spring*

© *Abdolreza Ebrahimi-Sabet (Syavash Shaghayegh)*

ACKNOWLEDGEMENTS

I am indebted to Professors Donald Cormack and Honghi Tran for their excellent supervision throughout the course of this work. Their professional guidance and passionate encouragement have been invaluable.

I wish to express my gratitude to Professors David Kuhn, Mark Kortschot and Andy Jones for serving in my Ph.D. committee. Their constructive criticism is highly appreciated. I am grateful to Dr. Andrei Kaliazine for his technical advice and valuable discussion. Special thanks are due to Professor Doug Reeve who has been playing as a role model for my personal development. I have benefited tremendously from his direction and leadership.

This work was financially supported by the members of the research consortium on Improving Recovery Boiler Performance, Emissions and Safety, and by Natural Science and Engineering Research Council of Canada. To them I am deeply grateful.

Last but the most, I owe my dearest thanks to my late parents, Azzam and Fazlollah, my sisters, Parvaneh, Parivash and Parinaz, and my brothers, Alireza and Gholamreza, whose unconditional love, continuous support and passionate encouragement through my life, have made me the person I am today. Without them I would have never made through dissipative and diffusive time.

TABLE OF CONTENTS

ABSTRACT	ii
ACKNOWLEDGEMENTS	iv
TABLE OF CONTENTS	v
LIST OF TABLES	viii
LIST OF FIGURES	ix
NOMENCLATURE	xiii
1. INTRODUCTION	1
2. THESIS OBJECTIVE	4
3. LITERATURE SURVEY	6
3.1. Deposition in Kraft Recovery Boilers	6
3.2. Sootblowing	9
3.3. Theoretical Considerations	11
3.3.1. The Mean Forces	12
3.3.2. Force Fluctuation Components	16
3.3.3. Effect of the Flow Confinement	18
3.3.4. Tube Bundle Forces	20
3.3.5. Lift Forces in Tube Bundles	21
3.4. Deposit Removal Mechanism by Brittle Fracture	21

3.5.	Deposit Removal by Debonding Mechanism	22
3.5.1.	Debonding Criteria	24
3.6.	Main Conclusions from Literature Review	30
4.	DEPOSIT BLOW-OFF EXPERIMENTS	32
4.1.	Experimental Apparatus and Procedure	32
4.2.	Results and Discussion	36
4.2.1	Effects of the Deposit Shape and the Jet Angle of Attack	38
5.	MEASUREMENTS OF THE MEAN DRAG FORCE	41
5.1.	Results and Discussion	42
5.1.1.	Effect of the Deposit Shape	43
5.1.2.	Effect of the Deposit Size	43
5.2.	Measurements of the Mean Lift Force	44
6.	MEASUREMENTS OF LIFT AND DRAG FORCE FLUCTUATIONS	46
6.1.	Measurements of Lift Force Fluctuations using a Torque Meter	47
6.2.	Flow-induced Vibration Forces Exerted on Deposits	49
6.2.1.	Analysis of the Response of a Vibrational System to a Randomly Fluctuating Force	50
6.3.	Lift Force Fluctuation Measurement Experimental Assembly	55
6.4.	Separation of the Lift Force Fluctuations from the Flow-Induced Vibrations	58
6.5.	Results and Discussion	59
6.6.	Measurements of Drag Force Fluctuations	60

7. IMPLICATIONS	62
7.1. Implication of Mean Drag Force Measurement Results	63
7.2. Implication of Force Fluctuation Measurement Results	64
7.2.1. Similarity of Force Spectra	64
7.2.2. Comparison with Blow-Off Results	69
7.2.3. Stress Generated at Tube-Deposit Interface in Recovery Boilers	73
7.3. Transition Time	77
8. CONCLUSIONS	79
9. RECOMMENDATIONS FOR FUTURE WORK	82
REFERENCES	84
TABLES	87
FIGURES	89
APPENDICES	141

LIST OF TABLES

Table 1. Comparison between the fully expanded sootblower nozzle and the laboratory nozzle.

88

LIST OF FIGURES

Figure 1. The schematic diagram of a kraft recovery boiler.	90
Figure 2. A sootblower in a machine shop.	91
Figure 3. A sootblower in action at the inlet of a boiler bank.	92
Figure 4. Condensed material deposited on screen tubes.	93
Figure 5. Plugging at the entrance of the boiler bank.	94
Figure 6. Characteristic dimensions of a deposit and aerodynamic forces.	95
Figure 7. Deformation of a deposit in debonding.	96
Figure 8. Distribution of tensile stresses at the flat and cylindrical interface.	97
Figure 9. Type A model deposit.	98
Figure 10. Type B model deposit.	99
Figure 11. The schematic diagram of how the adhesion strength of gypsum was measured using a strength tester.	100
Figure 12. Deposit removal (blow-off) experiment apparatus.	101
Figure 13. Definition of the jet attack angle.	102
Figure 14. Blow-off experimental data for type A deposit.	103
Figure 15. Blow-off experimental data for type B deposit.	104
Figure 16. PIP required to debond Type A deposit as a function of the adhesion strength.	105

Figure 17. PIP required to debond Type B deposit as a function of the adhesion strength.	106
Figure 18. Torque Meter Experimental Apparatus for the measurements of the mean drag force.	107
Figure 19. Model deposits.	108
Figure 20. Signal conditioning and data collection procedure.	109
Figure 21. The calibration curve for the torque meter.	110
Figure 22. Drag force profiles for 1.5" deposits.	111
Figure 23. Drag force profile for 0.75" deposits.	112
Figure 24. Comparison between the calculated maximum stress generated at the deposit-tube interface, based on the drag force experiment, with the previously obtained results from blow-off experiment.	113
Figure 25. Comparison between drag forces for elongated deposits with 1.5" and 0.75" diameters.	114
Figure 26. Comparison between drag forces for cylindrical deposits with 1.5" and 0.75" diameters.	115
Figure 27. Torque meter experimental apparatus for the measurements of the lift force.	116
Figure 28. Comparison between mean drag force decay and mean lift force (1-cm offset) for type A deposit.	117
Figure 29. The torque meter signals for 0° attack angle measured at 6-cm and 60-cm from the nozzle, respectively.	118
Figure 30. Comparison between the mean drag force and flow-induced vibrations (0° attack angle), measured by the torque meter.	119
Figure 31. Torque meter signal for 0° attack angle measured at 60-cm from the nozzle.	120
Figure 32. Load cell experimental apparatus: lift force measurement deposit orientation.	121
Figure 33. Load cell calibration curve.	122
Figure 34. The power spectra of the load cell signals at 20-cm and 57-cm, respectively.	123
Figure 35. Typical power spectrum of the lift force measured by the torque meter.	124

Figure 36. Power spectra of the raw signal and the lift force.	125
Figure 37. Comparison between the lift force fluctuations and the raw signal exerted on 3.8-cm cylindrical deposits (the effect of vibration is included).	126
Figure 38. Comparison between the lift force fluctuations and the raw signal exerted on 1.9-cm cylindrical deposits (the effect of vibration is included).	127
Figure 39. The profiles of the root mean square (r.m.s.) of lift force fluctuations exerted on 1.9-cm (0.75-inch) and 3.8-cm (1.5-inch) cylindrical deposits.	128
Figure 40. Load cell experimental apparatus: drag force measurement deposit orientation.	129
Figure 41. Comparison between the drag force fluctuations and the raw signal exerted on 3.8-cm cylindrical deposits (the effect of vibration is included).	130
Figure 42. Comparison between the drag force fluctuations and the lift force fluctuations exerted on 3.8-cm (1.5-inch) cylindrical deposits	131
Figure 43. The estimated drag force decay exerted on 15.2-cm (6") deposits in a boiler.	132
Figure 44. The estimated drag force decay exerted on 7.6-cm (3") deposits in a boiler.	133.
Figure 45. The dimensionless power spectra of the lift force exerted on 3.8-cm cylindrical deposit at different distances.	134
Figure 46. The dimensionless power spectra of the lift force exerted on 1.9-cm cylindrical deposit at different distances.	135
Figure 47. Free vibrations of the torque meter experimental apparatus with type A model deposit.	136
Figure 48. Comparison between the estimated effect of maximum vibration amplification on the stress generated by the lift force and the blow-off data.	137
Figure 49. Comparison between the estimated effect of the maximum vibration amplification on the stress generated by the drag force and the blow-off data.	138
Figure 50. The comparison between the maximum stress generated at the 90° and 0° attack angle orientations at the tube-deposit interface of a 15.2-cm (6-inch) thick deposit in a recovery boiler.	139

Figure 51. The comparison between the maximum stress generated at the 90° and 0° attack angle orientations at the tube-deposit interface of a 5-cm (2-inch) thick deposit in a recovery boiler.

140

NOMENCLATURE

A_e	area at the nozzle exit
A_t	throat area
$A_T(\omega)$	Fourier transform of the function $f_T(t)$
A_v	the vibrational amplification coefficient
a	dimensionless transverse spacing
B	assembly damping
$\overline{C_D}$	mean drag coefficient
C_{Dmax}	the maximum value of the mean drag coefficient
C'_D	drag fluctuation coefficient
$\overline{C_L}$	mean lift coefficient
C'_L	lift fluctuation coefficient
C_p	the gas specific heat at constant pressure
C_v	gas specific heat at constant volume
D	total damping coefficient
D_e	nozzle exit diameter
D_{ef}	effective jet diameter
d	characteristic body width
E	Young's modulus

Eu	Euler number
F	force, linear force density
$F(t)$	fluctuating force
$\overline{F_D}$	mean drag force
F'_D	drag fluctuations
$f_d(t)$	dimensionless lift force
$\overline{F_L}$	mean lift force
F'_L	lift fluctuations
F_{Tester}	tester force
f_0	peak frequency of the lift spectrum
$f_T(t)$	truncated force
H	characteristic body width, total enthalpy
H_x	<i>local</i> enthalpy
G	the shear modulus of elasticity
I	moment of inertia
K	rigidity of the system
k_h	the coefficient turbulent transfer of energy
k_s	height of surface roughness
k_v	the coefficient for turbulent transfer of momentum
L	body length
M	moment
M_e	free jet momentum flux at the nozzle exit
M_0	free jet momentum flux

m	mass
Ma	Mach number
M_x	local Mach number
n	number of samples
P	jet peak impact pressure
PIP	jet peak impact pressure
P_{cr}	jet peak impact pressure critical value
$p_F(\omega)$	power spectrum
$p(s)$	dimensionless power spectrum
R	tube radius
Re	Reynolds number
r_e	radius of the nozzle exit
r_x	radial distance at the axial location x from the nozzle
s	transverse spacing between tube axes, dimensionless frequency
S_{tu}	ultimate torsional strength
s_t	deposit tensile strength
Str	Strouhal number
T	transition time
Tu	turbulence intensity
T_x	local temperature at the jet centerline
U	fluid mean velocity, unconfined approaching velocity
U_m	dimensionless maximum confined velocity
U_{max}	maximum confined velocity

$\overline{u'^2}$	mean square value of the velocity fluctuation component
V_x	the axial profiles of velocity
x	the axial distance along the jet centerline
$y(t)$	instantaneous deflection
y_s	system response to a constant force
$Z(i\omega)$	system impedance
z	number of rows in the bundle

Greek Symbols

α	the attack angle
α_0	the angle proportional to the tube area covered by the deposit
β	damping coefficient
ΔP	the pressure drop across a bundle exposed to a flow of fluid
δ	thickness of the elastic adhesion layer
$\varepsilon_{rr}, \varepsilon_{r\theta}, \varepsilon_{\theta\theta}, \varepsilon_{zz}$	strain deformation components
φ	sample angular deflection around the tube axis
λ	Lame's constant
ν	Poisson's ratio
θ	the angle between the jet axis and the axis perpendicular to the tube axis
ρ	fluid density
ρ_e	gas density at the nozzle exit

ρ_x	gas density at axial location x from the nozzle
σ	normal stress
σ_D	normal stress generated by the drag force
σ_{Deb}	bond strength
σ_L	normal stress generated by the lift force
σ_{max}	maximum principal stress
τ	shear stress
ψ_{max}	dimensionless stress coefficient
ω	circular frequency
ω_{St}	Strouhal frequency

1. INTRODUCTION

Black liquor is burned in kraft recovery boilers to recover cooking chemicals and to produce power and steam (Figure 1). Black liquor, on a dry basis contains about 40-50% inorganic material. During the burning process, a portion of inorganic material is entrained in the flue gas and forms fireside deposits on heat transfer surfaces in the boiler [1-2]. Deposit accumulation is one of the most important factors limiting the boiler thermal efficiency. The accumulation drastically reduces the heat transfer efficiency, resulting in high flue gas temperatures and accelerated plugging of flue gas passages [1-3]. The production loss of a kraft mill caused by an unscheduled boiler shutdown for deposit cleaning can be substantial depending on the boiler capacity. Due to this high cost, kraft pulp mills management continuously attempts to avoid a boiler shutdown due to flue gas passage plugging, particularly where there is only one recovery boiler.

Deposits are removed from tube surfaces using sootblowers which blast deposits with high-pressure turbulent steam jets from the pair of nozzles at the end of the sootblower lance (Figure 2). Sootblowers consume approximately 5-10 % of the boiler steam production.

Deposits in recovery boilers are either brittle or "plastic", depending on whether the flue gas temperature is below or above the first melting temperature of the deposit [4], the temperature above which a liquid phase is present [1]. The two main deposit removal mechanisms are: brittle fracture and debonding [5]. Deposit removal by brittle fracture applies only to brittle, low-strength deposits, such as those in the region downstream of the generating bank. In the superheater region, deposits are usually dense, strong, may have a liquid surface due to the high flue gas temperature; they cannot be fractured by a sootblower jet.

High-strength and/or plastic deposits may be removed by a sootblower if there is a low-strength adhesive bond at the deposit/tube interface. This removal mechanism is called debonding. A low interfacial adhesive bond results when there is a powdery fume layer, or porous black liquor char between the hard deposit and the tube surface. Weak bonding may also be a result of thermal shock and/or tube vibration.

Debonding can be an important deposit removal mechanism. A deposit is removed from a tube surface, not because of its overall mechanical strength but because of its weak bond at the interface. This adhesion strength of the deposit/tube interface is generally much smaller than the overall mechanical strength in the regions where the flue gas temperature is above 350 °C. The ability of a sootblower jet to debond a deposit from a tube surface depends on many factors, including the jet characteristics, the bond strength at the deposit/tube interface, the size and shape of the deposit, and the area of the tube covered by the deposit.

To date, no study has been performed to examine the debonding mechanism. A better understanding of this removal mechanism may help improve the sootblower efficiency with a reduction in sootblower steam consumption.

2. THESIS OBJECTIVE

The study of debonding mechanism can be divided in two different sub-studies: the aerodynamic aspects of a sootblower jet and its interaction with deposits, and the bonding characteristics at the deposit-tube interface. This work is focused on the aerodynamic aspects of a sootblower jet and its interaction with deposits. To study the deposit removal by debonding, the following must be considered:

- (i) From an aerodynamic perspective, the effectiveness of a sootblower jet in the removal of deposits from tube platens or tube banks depends on the ability of the jet to exert sufficiently large forces on deposits accumulated at different locations inside the tube banks or platens (Figure 3). These forces generate stress at the deposit/tube interface. If the generated stress exceeds the adhesion strength between deposits and tubes, deposits will be debonded from tube surfaces.
- (ii) The penetration of a sootblower jet into a tube bank depends on tube arrangements and the deposit accumulation. The aerodynamic forces exerted by the jet on deposits with a tube bank would be different for other tube banks.

- (iii) As a sootblower moves into the boiler, it rotates and the jet hits deposits at different attack angles.
- (iv) The shape and dimensions of deposits may affect the jet profile. Therefore, the forces exerted on deposits by the jet may also be affected by the deposit shapes and dimensions.
- (v) It is difficult to conduct an experimental study on deposit debonding in actual boilers.

The objective of the present work is to conduct a laboratory study on deposit debonding from the tube surfaces and to investigate the effects of major aerodynamic and geometric parameters on the debonding mechanism. Parameters to be studied include the jet peak impact pressure (PIP), and the resulting drag and lateral forces produced by a jet on a deposit, deposit shape and dimensions; and deposit orientation with respect to the jet (jet attack angle). Since no study has been performed to examine the effects of these parameters, this work focuses on experimental investigation of a model sootblower jet interaction with a deposit accumulated on a single tube. Attempts are made to use the experimental results to make quantitative predictions about the removal of fireside deposits by sootblower jets in boilers.

3. LITERATURE SURVEY

This section provides a brief background on fireside deposit formation, the principles of sootblower operation, as well as theoretical considerations and detailed review of the literature related to aerodynamic forces exerted on a single tube covered by a deposit, the effect of flow confinement on these forces, the forces in tube bundles and the deposit break up mechanism.

3.1 Deposition in Kraft Recovery Boilers

Deposition at various locations in a boiler has been the subject of careful investigation. There are many publications on the deposit chemistry, deposit thermal properties and the formation mechanism [1-12]. Deposit accumulation may occur heavily at some locations, and may not occur at other locations in the boiler. Massive deposit accumulation on tube surfaces may plug the flue gas passages. Plugging is very complex and unpredictable. This has been attributed to almost everything related to recovery boilers: high flue gas temperature, high air flow rates, poor air distribution, poor boiler design, poor sootblowing efficiency, poor bed conditions and upset of liquor properties. The rate of fouling in the boiler bank is a function

of boiler bank inlet gas temperature. If this temperature is above the sticky temperature of the deposit, rapid fouling and plugging may occur.

Deposits are derived from three distinct sources: carryover, intermediate sized particles (ISP) and fume [2]:

- (i) **Carryover:** Relatively large, partially burned, black liquor and/or smelt particles, which leave the furnace cavity and are entrained in the flue gas.

- (ii) **Intermediate Sized Particles (ISP):** Also known as "ejecta", these particles are apparently formed by the ejection of material out of the black liquor droplet surface during the black liquor combustion process.

- (iii) **Condensed Material:** Dust or fume is fluffy white sub-micron particles, resulting from the condensation of compounds volatilized from the lower furnace. The condensation may occur directly on cooled surfaces or indirectly in the flue gas stream.

The most critical locations in the boiler that plugging may occur are the upper superheater regions upstream of the boiler bank inlet, and the boiler bank inlet itself. To prevent plugging and deposit accumulation in these regions, sufficient sootblowing must be provided. In these regions, deposits are mainly plastic and the dominant removal mechanism is deposit debonding.

In the upper superheater and the region upstream from the boiler bank, the flue gas temperature may range from 700 °C to 800 °C, and condensation takes place on cooled tube surfaces, where carryover deposition also takes place (Figure 4). This condensation forms a layer of fluffy, white deposits. Condensation may also take place in the flue gas stream, forming dust, which can be transported to tube surfaces. Meanwhile, the flue gas temperature range of 550 °C to 800 °C is considered to be the sticky temperature zone for typical deposits. In this temperature zone, carryover particles are above their sticky temperature, above which the deposit contains enough liquid phase to be sticky. Thus, carryover particles entrained in the flue gas stick to tube surfaces and continue to grow because the deposit surface temperature is lower than the radical deformation temperature. In this region, plugging may not be prevented unless sootblowing is sufficient. The deposit accumulation usually occurs on the tube leading edge due to the impaction of partially or completely molten carryover particles. If sootblowing is insufficient, the deposit eventually bridges the spacing between adjacent platens [2].

At the boiler bank inlet, the flue gas temperature is close enough to the minimum deposit sticky temperature, in the range of 550 to 700 °C. Depending on their composition and the presence of condensed particles, carryover particles may or may not stick to tubes. At these locations sootblowing is usually the least effective because the tube spacing in the boiler bank is much narrower than in the superheater region (Figure 5). Thus, if the carryover particles are sticky, severe plugging at the boiler bank region is highly likely. Furthermore, as the deposit thickness grows, its outer surface temperature rises and sintering occurs. The outer layer would become hard after about an hour if its temperature exceeds 500 °C, whereas the

cooler inner layer adjacent to the tube remains unsintered and soft [1-2]. Due to the weak bonding between the soft inner layer and the tube surface, these deposits might be debonded from tubes by sootblowers.

3.2. Sootblowing

Sootblowers are used to remove deposits from tube surfaces by multiple impacts of superheated steam jets ejected through a pair of nozzles, located at the end of a long translating, rotating lance tube. For typical sootblowers used in recovery boilers, the path of each nozzle is helical. Helices of 10.2, 15.2 or 20.3 cm (4", 6", or 8") may be used depending on the length of the sootblower and the intended service. When the sootblower reverses, the lance indexes enable the nozzles to return in a helical path that bisects the helical path of the forward travel. This provides a more uniform coverage of tube surfaces.

In recent years, attempts have been made to improve the cleaning effectiveness of the sootblower by redesigning the lance tube nozzles [13-16]. The cleaning efficiency of a sootblower is a function of nozzle size, blowing pressure and lance rotational and translational speeds. The jet peak impact pressure (PIP) of the steam flow through sootblower nozzles is one of the main parameters affecting the ability of the jet to remove deposits [13-17]. This pressure is defined as the stagnation pressure P , measured along the nozzle centerline downstream of the nozzle outlet:

$$P = \frac{\rho U^2}{2} \quad (1)$$

where ρ and U are the fluid (steam) density and the fluid mean velocity, respectively.

The further downstream from the nozzle outlet the more the PIP decreases due to the fluid deceleration associated with flow dispersion downstream of the nozzle exit. The stronger the deposit, the higher the PIP required to remove it. Thus, a minimum cleaning energy is required to remove a deposit of a given strength, and the higher the PIP of the jet, the more deposits can be removed.

The lance tube rotates during both the insertion and retraction passes through the boiler. Conventional lance tubes have two, diametrically opposed nozzles installed, whereas in the advanced lance tubes, the axes of these nozzle couples have a small offset with each other [16]. The axes of nozzles are typically perpendicular to the axis of the lance tube, although in some designs angled nozzles are also used to allow the jet to reach and clean spaces behind the tubes. In the latter design, the tube bundle depth penetration is drastically reduced [17].

Jameel et al. [13] developed a mathematical model, based on theory and experimental results to predict the axial decay of the PIP delivered by a sootblower. They showed that conventional sootblower nozzles produce an under expanded jet resulting in a dissipative shock wave at the nozzle exit, irreversibly converting a substantial portion of kinetic energy of the jet into internal energy and heat. This reduces the available PIP for deposit removal. They designed a new nozzle, which allows the jet to achieve full expansion before exiting the nozzle, resulting in the elimination of the shock wave and a 56% increase in the area that the jet is effectively able to remove the deposits.

The new types of sootblower nozzles are fully expanded nozzles. To allow the jet to achieve full expansion, the distance between the throat and the nozzle exit in fully expanded nozzles is much greater than that of a conventional nozzle. In addition, the contour of the divergent section of a fully expanded nozzle is precisely designed to prevent any flow separation or occurrence of shock waves within the nozzle. These features allow the steam pressure at the nozzle exit to be adjusted to the ambient pressure, minimizing the occurrence of shock waves downstream of the nozzle. A comparison of PIP of the improved nozzle and that of a conventional nozzle shows that the new nozzle increases PIP up to 103% at a radius of 76 cm. Alternatively, the new nozzle design can make up to a 40% increase in cleaning radius [13, 14,16].

For a given nozzle design, an increase in the lance pressure results in a proportional increase in steam flow rate and hence steam consumption. Since for a given lance pressure, the fully expanded nozzle produces a much higher PIP than that produced by a conventional sootblower nozzle; the new nozzle is able to produce the required PIP while using a substantially lower steam flow rate. This can decrease the overall steam consumption by 40% [16].

3.3. Theoretical Considerations

In order to understand the jet-deposit interaction, knowledge of the forces exerted on deposits by the jet is required. When a fluid jet flows over a body, it exerts two major aerodynamic fluctuating forces on the body: the drag force, F_D , and the lift force, F_L , acting

parallel and perpendicular to the flow direction, respectively (Figure 6) [18,19,22,25-29].

Each of these forces consists of a mean component and a fluctuation component.

3.3.1. The Mean Forces

The mean drag force, $\overline{F_D}$, and the mean lift force, $\overline{F_L}$, acting on an immersed body are generally expressed in terms of the mean drag and the mean lift coefficients $\overline{C_D}$ and $\overline{C_L}$, defined as:

$$\overline{C_D} = \frac{\overline{F_D} / Ld}{\rho U^2 / 2} \quad (2)$$

$$\overline{C_L} = \frac{\overline{F_L} / LH}{\rho U^2 / 2} \quad (3)$$

where U is the mean jet velocity approaching the body, L is the body length, d and H are characteristic body width, customarily defined as the body dimension normal to the flow direction.

These coefficients are functions of many parameters and conditions including boundary geometry, the turbulence intensity, Tu , the height of surface roughness, k_s , the Reynolds number, Re , and the Mach number, Ma [20]. The turbulence intensity Tu characterizes the degree of turbulence in the approaching flow and is defined as:

$$Tu = \frac{(\overline{u'^2})^{1/2}}{U} \quad (4)$$

where $\overline{u'^2}$ is the mean square value of the approaching flow velocity fluctuation component.

For bodies immersed in turbulence-free flows, the dependence of the mean drag coefficient on the Reynolds number differs for bodies with different shapes [20]. While the mean drag coefficient profile for a flat plate immersed in turbulence-free flow is independent of the Reynolds number, the mean drag coefficient profile for a circular cylinder depends on the Reynolds number. The mean drag coefficient profile for a circular cylinder can be divided into different regions: it ranges from purely viscous resistance at low Reynolds numbers region, extends through the region of laminar boundary layer separation at moderately high Reynolds numbers, to the region of turbulent boundary layer separation as the Reynolds number passes its critical value and reaches a very high value. An increasing deviation from each of these values occurs as the cylinder decreases in length. In other words, "*end effects*" tend to reduce the mean positive pressure and the mean negative pressure at the front and at the rear, respectively [21].

The typical conditions in a recovery boiler are $d=0.05\text{m}$, $U=10\text{m/s}$, $\nu=10^{-4} \text{ m}^2/\text{s}$ and $Re=5000$ at locations where the flue gas temperature is 500-600 °C. Sootblower jets may hit the deposit with velocities in the range of 100-500 m/s, which corresponds to a Reynolds number of $Re=10^5\text{-}2 \times 10^5$. The total drag coefficient of a long single circular tube reaches a constant value $\overline{C_D} \approx 1.2$ for Re from 1000 to 2×10^5 . At $Re_{cr} \approx 2 \times 10^5$ the locus of boundary layer

separation is shifted downstream for a cylinder with a smooth surface, as the boundary layer changes from laminar to turbulent. This is accompanied by a reduction of $\overline{C_D}$ to approximately 0.32. This phenomenon is called aerodynamic resistance crisis. It is associated with a reduction of wake behind the cylinder caused by the shift of boundary layer separation as the boundary layer changes from laminar to turbulent.

With a further increase in the Reynolds number to supercritical values, the locus of the transition to a turbulent boundary layer shifts upstream. Therefore, the value of $\overline{C_D}$ at supercritical Re is slightly higher than at critical Re , and it increases to an average value of 0.42. However, this is true only for cylinders with very smooth surface and for turbulence-free approaching flow.

As previously mentioned, the occurrence of turbulence in the boundary layer on a cylinder causes a dramatic decrease in the drag coefficient. For a turbulence-free flow over a smooth cylinder, this decrease in the drag coefficient occurs at a critical Reynolds number $Re_{cr} \approx 2 \times 10^5$. If the cylinder has a rough surface, the roughness disturbs the flow near the surface, the transition to turbulence occurs at smaller Reynolds numbers and the corresponding decrease in the drag coefficient shifts accordingly. The larger the equivalent roughness k_s , the greater the shift. However, the decrease in the drag coefficient becomes smaller with an increase in the relative roughness k_s/d , and the phenomenon of aerodynamic resistance crisis is less pronounced: the drag coefficient drop is smaller, and the recovery of the drag coefficient is more complete for a tube with a rough surface. If $k_s/d > 0.01$, the drag coefficient varies within the limits 0.9-1.2 for all $Re > 1000$.

The turbulence intensity, Tu , has an effect similar to surface roughness. An increase in Tu also causes the variations in drag to decrease in magnitude in the vicinity of the aerodynamic crisis. Turbulence decreases $\overline{C_D}$ in the subcritical Reynolds number range, but increases $\overline{C_D}$ in the supercritical Reynolds number range. At $Tu=9.1\%$, the mean drag coefficient $\overline{C_D}$ is approximately 0.8 over a very wide range of Reynolds numbers, and decreases by less than 15% at the critical Reynolds number [20]. The turbulence intensity in turbulent jets is very high (about 40%). Thus this factor also should be taken into account in a study of jet-tube interaction.

For compressible flows, the drag force and pressure distribution also depend on Mach number [19]. Ferri [23] and Fage [24] have measured drag force and pressure distribution on cylinders over a wide range of Reynolds and Mach numbers. Their experimental data show that even for moderate $Ma>0.4$ there is no drop in the drag coefficient, which takes place at $Re\approx 20,000$ for incompressible flows ($Ma\rightarrow 0$). For $Ma>0.4$, the drag coefficient reaches a constant value of $\overline{C_D}\approx 1.2$ for all $Re>10^4$.

In recovery boilers, sootblower jet-tube aerodynamic interaction is characterised by very high turbulence intensities, large Mach numbers, large Reynolds numbers and very rough boundary surfaces. Thus, for the operating conditions under these large Reynolds numbers the mean drag coefficient $\overline{C_D}$ is independent of Reynolds number variations.

The amplitude of the mean lift coefficient depends strongly on deposit geometry and orientation. It would be zero for symmetrical deposits with respect to the jet axis.

3.3.2. Force Fluctuation Components

Even under conditions of steady, laminar cross flow running over a cylindrical body, the flow pattern and, hence, the force, affecting the body, experiences periodic or quasiperiodic variations. As the Reynolds number increases beyond 40, the wake behind a cylinder becomes unstable and eddies start separating from the tube surface and vortex shedding starts. At moderate Reynolds numbers the resulting eddy wake, or so-called von Karman street, is laminar and stable at a sufficient distance from the tube.

At a Reynolds number equal to 150, irregular periodic perturbations occur in the wake of the tube and these continue up to $Re = 300$, at which point the wake becomes fully turbulent. This wake flow pattern prevails until the onset of the critical flow ($Re = 2 \times 10^5$) which is characterized by the steep drop in the drag coefficient followed by an increase as the Reynolds number increases.

The dominant frequency of vortex shedding is generally described in terms of the Strouhal number, which is the ratio of the product of vortex shedding frequency and body reference dimension to flow velocity, $Str = f_0 d / U$ where f_0 represents the peak frequency of the lift spectrum. In a wide subcritical region of Reynolds numbers, $Str \approx 0.20$ for an isolated single

cylinder. This non-steady flow pattern behind a cylinder is accompanied by drag force fluctuations. The coefficients of fluctuating drag and lift are defined by the root mean square (r.m.s.) of the drag F'_D and lift F'_L fluctuations:

$$C'_D = \frac{\left(\overline{(F'_D)^2}\right)^{1/2} / Ld}{\rho U^2 / 2} \quad (5)$$

$$C'_L = \frac{\left(\overline{(F'_L)^2}\right)^{1/2} / LH}{\rho U^2 / 2} \quad (6)$$

For $5 \times 10^3 \leq Re \leq 10^6$ drag fluctuation coefficients vary with the Reynolds number similar to $C_D (Re)$: They are approximately constant in the subcritical region, and decrease steeply at $Re \approx 2 \times 10^5$ [25]:

$$C'_D \approx 0.1 \quad C'_L \approx 0.5 \quad \text{at} \quad Re < 2 \times 10^5$$

$$C'_D \approx 0.03 \quad C'_L \approx 0.15 \quad \text{at} \quad Re > 2 \times 10^5$$

The drag and lift fluctuation coefficients are more sensitive to flow turbulence than are the mean drag and mean lift coefficients. This can be easily seen from the scattered experimental data on the lift fluctuation coefficient [24].

3.3.3. Effect of the Flow Confinement

The mean and fluctuation lift and drag coefficients discussed in the previous sections are related to the case when the fluid flows over a single tube (body). In recovery boilers, heat exchanger tubes are arranged in the form of tube bundles (boiler banks) or platens (superheaters). Deposits accumulated on these tubes, especially tubes behind the first row, would be considered to be confined by other tubes. In this section the available literature discussing the effect of flow confinement on drag and lift coefficients are reviewed.

Richter and Naudasher [27] experimentally studied mean and fluctuation lift and drag coefficients acting on a cylinder of diameter d placed symmetrically in a narrow rectangular duct of width h . They plotted the mean drag coefficient $\overline{C_D}$ profile as a function of the Reynolds number, and found that an increase in flow confinement leads to larger values of the mean drag coefficient. The maximum value of the coefficient at subcritical Reynolds numbers $\overline{C_{D_{\max}}}$ varies from 1.23 for an unconfined flow to 1.9 for $d/h=1/2$. $\overline{C_{D_{\max}}}$ may be expressed as a power function of the maximum confined velocity $U_m = U_{\max} U = h/(h-d)$:

$$\overline{C_{D_{\max}}} = 1.27 U_m^{0.61} \quad (7)$$

where U_{\max} and U are the maximum confined velocity and the unconfined approaching velocity, respectively.

Zukauskas et al. [25] and Richter and Naudascher [27] showed that the intensity of drag fluctuations becomes smaller with flow confinement and is always several times smaller than that of the lift fluctuations. Based on their plot of the lift fluctuation coefficient profile versus the Reynolds number and confinement ratio, they concluded that flow confinement decreases the magnitude of the drag fluctuation coefficient, but increases the lift fluctuation coefficient. For a confinement ratio $d/h=1/2$, the lift fluctuation coefficient reaches a value of up to eight times that of unconfined flow. C'_{Lmax} may be presented as a function of U_m by the following relationship:

$$C'_{Lmax} = 0.49U_m^{3.07} \quad (8)$$

An increase in flow confinement produces a distinct increase in the Strouhal number which reaches 0.33 in the subcritical region of the Reynolds number, for $d/h=1/2$. Thus, the lift fluctuation coefficient in confined flows may exceed the mean drag coefficients. This conclusion is important for the understanding of how deposits may be removed by a debonding mechanism. Since deposits normally grow in the direction of flue gas flow in the boiler, they are easier to remove by a force in the lateral direction than by a drag force, which pushes them against the tube surface.

The data from the above literature refer to the case of rigidly fixed tubes, which were not allowed to oscillate. There are some experimental indications that tube vibration may cause an additional increase in the lift fluctuation coefficient. For example, a relative amplitude of tube oscillation y/d even as small as 0.003 - 0.004 may increase C'_L 2 to 3 times [20]. Hence, increasing the deposit debonding probability.

3.3.4. Tube Bundle Forces

The hydraulic drag on a tube bundle is the sum of all drag forces exerted on individual tubes in the bundle. It is approximately proportional to the number of tube rows. An average drag force on tubes in a bundle can be described either by an average drag coefficient $\overline{C_D}$ or by an average Euler number [25]. The Euler number is defined as the ratio of pressure forces to flow inertia forces:

$$Eu = \frac{\Delta P}{\rho U^2 z} \quad (9)$$

where ΔP is the pressure drop across a bundle exposed to a flow of fluid and z is the number of rows in the bundle. The total pressure drop is the sum of all drag forces acting on tubes:

$$\Delta P s L = \overline{F_D} z \quad (10)$$

where F_D is the mean drag force on a tube in a bundle, and s is the transverse spacing between tube axes. Equations (2), (3), (9) and (10) may be combined to obtain:

$$Eu = \frac{\overline{C_D}}{2\alpha} \quad (11)$$

where $a=s/d$ is the dimensionless transverse spacing.

3.3.5. Lift Forces in Tube Bundles

Oengoeren and Ziada [28] carried out experiments to measure drag and lift fluctuation coefficients for an airflow over square tube bundles with a pitch ratio of 1.95. They concluded that an increase in the number of rows in a tube bundle leads to an increase in the lift fluctuation coefficient. They also suggested that when a gas flows through a tube bundle, it experiences strong transverse fluctuations, which may result in vortex shedding. Therefore, the lift fluctuation coefficient depends on the location of the tube in the bundle, and may differ from that of an isolated single tube [27,29,30].

The data reported in reference [27] (§1.3.3) shows that fluctuating lift forces, acting in the transverse direction are comparable with steady drag, and for confined flows, may even exceed it. Therefore, this is further evidence that lift forces may play the dominant role in the removal of asymmetrical deposits on tube bundle surfaces.

3.4. Deposit Removal Mechanism by Brittle Fracture

As mentioned in the introduction, brittle and low-strength deposits are removed by sootblower jets through brittle fracture mechanism. These deposits are accumulated in the

regions in which flue gas temperatures are low, such as regions downstream of the generating bank. When a jet hits a brittle deposit, it shatters the deposit into pieces.

Kalianzine et al. [15] studied the brittle fracture mechanism and showed that the important parameter is the deposit mechanical strength, which varies from location to location within a boiler because of variations in deposit chemistry, formation mechanism and flue gas temperature [1,30]. They showed that for a wide range of deposit geometry a sootblower jet is able to break a deposit only if the jet PIP exceeds a critical value:

$$P \geq P_{cr} = \frac{2s_t}{\cos\theta} \quad (12)$$

where s_t is the deposit tensile strength, and θ is the angle between the jet axis and the axis perpendicular to the tube axis.

They also showed that the brittle deposit failure process is an instantaneous process; that is deposits would be broken up the instant that the jet hits them.

3.5. Deposit Removal by Debonding Mechanism

The deposit debonding mechanism is governed by several factors, such as aerodynamic forces exerted on the deposit, jet attack angle, deposit-tube interface, deposit size and shape. The smaller the deposit-tube interface, the easier to debond the deposit from the tube surface.

Furthermore, a jet pushing the deposit onto the tube surface primarily produces compressive stresses at the tube-deposit interface, which make deposit debonding more difficult rather than easier. However, a force with the same magnitude, but applied from the side, may generate substantial tensile stress at the interface and cause the deposit to debond from the tube.

A deposit debonds from the tube surface if the stress generated by impact of the sootblower jet on the deposit exceeds the adhesion strength at some point at the tube-deposit interface. The stress distribution at the interface can be calculated if the deposit's exact shape and the forces applied to the deposit are known. However, this direct approach is not practical for several reasons:

- (i) The deposit shape is irregular and difficult to characterize.
- (ii) When a sootblower jet hits a deposit, the exact pressure distribution on the surface of the deposit of an arbitrary shape cannot be determined precisely. The velocity fluctuations and, hence, the impact pressure fluctuations of a high-speed turbulent jet hitting a deposit are large. Thus, it is likely that the extremes of turbulent fluctuations may be responsible for deposit debonding.
- (iii) The deposit mechanical properties are not uniform throughout the bulk of the deposit due to the variations in deposit porosity and temperature. Since the deposit outer layer

is exposed to high flue gas temperatures, it is denser and at a higher temperature than the inner layer.

Therefore, it was necessary to take into account the above considerations while designing the experiments to simulate the actual deposit debonding that occurs in boilers.

3.5.1. Debonding Criteria

A deposit would be removed by debonding if the stress generated by the impact of a sootblower jet on the deposit exceeds the adhesion strength at any point at the interface. The stress distribution at the interface can be calculated by means of the theory of elasticity if the deposit shape, the applied forces and the area of the interface are known [31]. The detailed calculation of σ_{max} is described in Appendix A.

Consider a piece of deposit covering the front side of a tube in a sector $\pm \alpha_0$ of the tube circumference (Figure 7). Moments and forces produced by a sootblower jet on the deposit, cause stresses at the tube-deposit interface. The outer layers of the deposit may be too strong to be fractured by the sootblower jet. Therefore, if the deposit is removed by debonding, the adhesion layer should be weaker than the bulk of the deposit. As a reasonable approximation, the bulk of the deposit may be considered as absolutely rigid and the weaker layer at the tube-deposit interface. When the sootblower jet hits the deposit, the distributions of normal (radial) stress σ and shear stress τ along the tube-deposit interface can be calculated:

$$= \frac{F}{R} (2 + \nu) \sin \alpha \frac{\frac{M}{FR} \sin \alpha_0 - \frac{\alpha_0}{2}}{\alpha_0 \left((3 + \nu) \frac{\alpha_0}{2} - (1 + \nu) \frac{\sin(2\alpha_0)}{4} \right) - 2 \sin^2 \alpha_0} \quad (13)$$

$$\tau = \frac{F}{R} \frac{\frac{M}{FR} \left((3 + \nu) \frac{\alpha_0}{2} - (1 + \nu) \frac{\sin(2\alpha_0)}{4} - \sin \alpha_0 \cos \alpha \right) + \frac{\alpha_0 \cos \alpha}{2} - \sin \alpha_0}{\alpha_0 \left((3 + \nu) \frac{\alpha_0}{2} - (1 + \nu) \frac{\sin(2\alpha_0)}{4} \right) - 2 \sin^2 \alpha_0} \quad (14)$$

where $-\alpha_0 < \alpha < \alpha_0$, ν is the Poisson's ratio and R is the tube radius.

Analysis of these equations shows that the maximum principal stress σ_{max} at the tube-deposit interface depends on two dimensionless parameters α_0 and FRM :

$$\sigma_{max} = \frac{\sigma}{2} + \sqrt{\left(\frac{\sigma^2}{4} + \tau^2\right)} \quad (15)$$

or

$$\sigma_{max} = \frac{F}{R} \psi_{max}(\alpha_0, M / FR) \quad (16)$$

where ψ_{max} is a dimensionless function that describes the effect of deposit geometry. Note in Equation (15), we are interested in the maximum tensile stress due to the brittle characteristic

of the interfacial bonding layer. The parameter α_0 defines which part of the tube is covered with deposit; parameter FM/R characterizes the external forces applied to the deposit. The latter parameter is generally about 1 for a relatively thin deposit layers because the bulk of a thin deposit is located at the distance R from the tube axis. This parameter becomes larger for thicker deposits. An example of the calculated stress distribution is shown in Figure 8 for the case $2\alpha_0=180^\circ$ (half of the tube circumference is covered with deposit) and $FM/R=2$, the maximum tensile stress is generated at the edge of the deposit and is about $\sigma=1.5FD$, that is about 2 times smaller than maximum stress at a flat interface (shown for comparison in Figure 8 by a dashed line) [31].

The angle α_0 is proportional to the tube area covered by the deposit. If the jet attack angle is 0° degree, for a given lateral force F or moment M , the smaller α_0 , the greater the stresses generated at the tube-deposit interface. Thus, the deposit is removed more easily [31].

Now consider the case when F is exerted on the deposit along the jet axis (in this case F is the drag force): the distributions of normal (radial) stress σ and shear stress τ along the tube-deposit interface, Equations (13) and (14) become:

$$\sigma = \frac{F}{R} \frac{(2 + \nu) \cos \alpha}{\left((3 + \nu)\alpha_0 + (1 + \nu) \frac{\sin 2\alpha_0}{2} \right)} \quad (17)$$

$$\tau = \frac{F \sin \alpha}{R \left((3 + \nu)\alpha_0 + (1 + \nu)\frac{\sin 2\alpha_0}{2} \right)} \quad (18)$$

The maximum principal stress can be calculated again from Equation (15).

In case that both of these forces are exerted on the deposit, the maximum combined principal stress can be calculated:

$$\sigma_{\max} = \frac{\sigma_L + \sigma_D}{2} + \sqrt{\left(\frac{\sigma_L + \sigma_D}{2}\right)^2 + (\tau_L + \tau_D)^2} \quad (19)$$

where the subscripts L and D represent the stresses generated by the lateral and axial (Drag) forces, respectively. Note in Equation (15), we are interested in the maximum tensile stress due to the brittle characteristic of the interfacial bonding layer.

For any distance from the nozzle, the distribution of the principal stress at the tube-deposit interface over the cover sector $\pm \alpha_0$ can be calculated by Equation (15) or Equation (19). These equations are functions of the angle α , where $-\alpha_0 < \alpha < \alpha_0$. If this stress at any angle α exceeds the adhesion bond strength of the intermediate bonding material, the tube-deposit bond fails and the deposit will be debonded. Thus to investigate the debonding criteria, the principal stress distribution must be calculated by Equations (15) or (19) and the maximum stress of this distribution should be compared with the adhesion bond strength.

When a sootblower jet impacts a piece of deposit, it generates a peak impact pressure P . For a specific nozzle geometry, P is a function of the gas inlet pressure of the sootblower nozzle and the distance between the sootblower nozzle and the deposit. For a constant gas inlet pressure, P can be calculated as a function of the distance from the nozzle. For a deposit, extending laterally to the jet direction (90° jet angle of attack), it can be predicted that debonding mainly occurs by drag forces. Thus, based on the definition of the Peak Impact Pressure P (Equation (1)), the linear density of the drag force \overline{F}_D can be calculated as:

$$\overline{F}_D = \overline{C}_D \rho \frac{U^2}{2} d = \overline{C}_D P d \quad (20)$$

Debonding occurs if:

$$\sigma_{\max} \geq \sigma_{Deb} \quad (21)$$

Considering the case of drag force $F = \overline{F}_D$, from (16), (20) and (21), σ_{Deb} , could be estimated as:

$$\sigma_{\max} = \overline{C}_D P d \psi_{\max} \geq \sigma_{Deb} \quad (22)$$

where σ_{Deb} is the bond strength and $P=P(x)$ is a function of distance from the nozzle outlet. In Equation (22) the effect of any lateral force, such as lift force, is considered to be negligible.

Similarly, for a piece of deposit growing in the direction of the jet, deposit debonding from the tube surface occurs mainly by the lateral (lift) fluctuation components (0° angle of attack), acting at right angles to the major axis of the deposit. In this case, deposit debonding occurs, if:

$$\left(\overline{(F'_L)^2}\right)^{1/2} = C'_L \rho \frac{U^2}{2} H = C'_L PH \quad (23)$$

$$\sigma_{\max} = C'_L PH \psi_{\max} \geq \sigma_{Deb} \quad (24)$$

In Equation (24), the effect of drag force is considered to be negligible. This assumption will be discussed in detail in §7.2.3.

3.6. Main Conclusions from Literature Review

In this section the main observations applicable to this study are summarized:

- (i) In recovery boilers, sootblower jet-tube aerodynamic interaction is characterised by very high turbulence intensities, large Mach numbers and very rough boundary surfaces. Thus, the value of drag coefficient may be different from the literature data.
- (ii) The drag and lift fluctuation coefficients are more sensitive to flow turbulence than are the mean drag and mean lift coefficients.
- (iii) The mean drag coefficient $\overline{C_D}$ for a single tube varies from 0.5–2, whereas the lift fluctuation coefficient C'_L varies from 0.12 to 4 [22,25-29].
- (iv) Flow confinement causes C'_L to increase dramatically to values higher than those for $\overline{C_D}$ [26-29].
- (v) The lift and drag forces on tubes inside tube bundles depend on the location of the tube. These forces for the front tube could be estimated from the data for a single tube.
- (vi) For inner tubes in a tube bundle, the drag and lift forces behave differently. For the inner tubes in a tube bundle, while drag forces are smaller than for the first row, the lift

fluctuations increase as the row number in the bundle increases, reaching a maximum for the third or fourth row [26,28].

(vii) There are no detailed data available on drag and lift forces produced by a jet flow.

To understand the deposit debonding mechanism, debonding of model deposits by a supersonic jet was investigated through laboratory experiments. These experiments and the obtained data are discussed in details in the next section.

4. DEPOSIT BLOW-OFF EXPERIMENTS

In order to conduct a laboratory study of the deposit debonding mechanism, as a first step, it was necessary to conduct experiments that simulate the actual deposit removal by debonding that happens in boilers. The main purpose of these experiments was to determine a correlation between the adhesion strength of deposits and the minimum peak impact pressure (PIP) required to debond them. In this set of experiments, artificial model deposits, with known adhesion strength and attached to a single tube, were debonded by a fully expanded laboratory nozzle jet.

4.1. Experimental Apparatus and Procedure

In order to study the debonding mechanism by an air jet in the laboratory, it is important to use a model deposit that will not be fractured by the jet, and an interfacial bonding material which has a known, controllable adhesion strength. In this study, wood was used as a model deposit, because wood is strong enough not to be fractured by the jet. Two different types of deposit made from wood were examined: type A had a flat, elongated shape and type B had a short, rounded shape (Figures 9 and 10).

Deposits, with a length of 5-cm (2") were attached to a stainless steel tube using gypsum (plaster of Paris) as the bonding material. Gypsum was chosen as a model interfacial bonding material, because its strength could be measured and could be altered easily by changing the water to plaster ratio. All model deposits were air-dried in an oven at 55 °C. The adhesion strength of gypsum was determined using a strength tester (Figure 11). The model deposit-tube assembly acted as a cantilever, with the tube being fixed. The tester force F_{Tester} was increased slowly until the model deposit was debonded from the tube due to the failure of the gypsum bond. The force F_{Tester} at the start of the failure of gypsum bond reached its maximum and was automatically recorded by the tester. By knowing F_{Tester} the maximum normal stress at the tube-deposit stress was calculated using Equation (15). Since gypsum is a brittle material, the maximum-normal-stress theory was used to determine the failure criteria. To determine the failure criteria for brittle materials the following characteristics of these materials should be considered [32]:

- (i) Brittle materials do not have yield strength. A graph of stress versus strain is a smooth continuous line to the failure point and failure occurs by fracture.
- (ii) The compressive strength is usually many times greater than the tensile strength for these materials.
- (iii) The ultimate torsional strength S_{tu} or the modulus of rupture is approximately the same as the tensile strength for brittle materials.

The maximum-normal-stress theory has been used to predict the fracture of brittle materials [32]. Hence, to determine the adhesion strength (bond strength) of model deposits this theory was used.

The ability of an air jet to debond such model deposits was examined using a blow-off apparatus (Figure 12). Compressed air from four compressed air cylinders was supplied to a nozzle with a throat diameter of 7.42 mm (0.125"). The nozzle provided a fully expanded jet with a working inlet air pressure of 6.8 MPa and outlet pressure of 101 kPa.

The results obtained from the scaled-down laboratory nozzle are applicable to a sootblower nozzle operating in a recovery boiler only if a set of geometrical and aerodynamical conditions for the model and the sootblower nozzle are met. The principle of dynamical similarity dictates that not only must the model and the full-expansion sootblower nozzle be geometrically similar, but also their key dimensionless numbers, the Mach and Reynolds numbers, must be identical. Table 1 shows the basic parameters of the model and those of a typical full-expansion sootblower nozzle operating under boiler conditions. The geometrical scale is 1:4 and the Mach and Reynolds numbers differ by only 5% and 6%, respectively. Hence, the nozzle used in these experiments is dynamically and geometrically similar to a typical fully expanded sootblower nozzle operating in a recovery boiler.

The pressure upstream of the nozzle was measured using an Omega PX603 0 – 13.6 MPa (0-2000 psig) pressure transducer. The peak impact pressure (PIP) of the air jet was increased by moving the nozzle toward the model deposit surface until the model deposit was blown

off. The distance between the nozzle and the model deposit surface was used to calculate the minimum jet PIP required for debonding.

Each type of deposit was blown off under mainly two different orientations relative to the jet axis: jet attack angles of 0° (the jet axis is parallel to the characteristic thickness of the deposit) and 90° (the jet axis is perpendicular to the deposit characteristic thickness) (Figure 13). The results of these two extreme cases would help determine the effect of the jet attack angle on the debonding. In a few experiments, type A deposits were blown off under 45° jet attack angle. In each experiment a laser pointer was used to control the orientation of the model deposits with respect to the jet axis.

To ensure that the model deposit would be debonded from the tube at a bonding interface in the gypsum layer, a layer of carpenter white glue was placed between the tube and gypsum, and gypsum and wood. Since glue is a stronger bonding material than gypsum, debonding would occur in the gypsum layer. In order to obtain reproducible results the thickness of the gypsum layer was kept at 3 mm.

As the gypsum slurry hardens, its adhesion strength changes with time. To ensure that model deposits used in each set of experiments have identical adhesion bond strength, there was a time constraint in filling the slots in the wooden model deposits with gypsum. Thus, the number of model deposits used in each set of experiments was restricted to six.

For each experiment, six samples were prepared: three used for adhesion strength measurements and three for blow-off tests. The mean value of the experimentally determined adhesion strength and the average distance to the nozzle at which blow-off was observed, were plotted. To obtain each data point, six measurements were required.

4.2. Results and Discussion

The results obtained for the elongated type A deposit are shown in Figure 14. Each data point shown represents a set of 6 experiments. The actual number of experiments carried-out is four times the number of data points shown. At first, the data were scattered widely due to the various sources of error in the experiments, such as the poor control of gypsum layer thickness. As the study was in progress, several modifications were carried out to increase the reproducibility and to minimize the scatter of data.

The vertical axis of Figure 14 represents the mean value of the adhesion strength of the three samples used in each experiment. These values were obtained based on the maximum of the principal stress distribution at gypsum layer surface calculated by Equation (15). The horizontal axis represents the mean value of the distance from the nozzle, at which blow-off occurred for the other three samples used in each set of experiments. The results show that the higher the adhesion strength, the closer the nozzle needs to be to the target. For an increase in the adhesion strength from 0.05 MPa to 0.4 MPa, the distance between the nozzle and the deposit decreased from 120 cm to 25 cm.

In the 0° attack angle experiments, 20 model deposits with adhesion strength between 0.1 to 0.4 MPa were placed at 35 cm from the nozzle and moved to the 7.5 cm in the vicinity of the nozzle, while the jet was activated. Despite expectations, none of these deposits were debonded by the jet. The gray-shaded box represents the adhesion strength of these deposits and the region where deposits were not removed by the jet. Some of these deposits were placed later further downstream from the nozzle, ranging from 60 cm to 90 cm to the nozzle, and were blown-off by the jet eventually. However due to the possible generation of flaws and cracks in the adhesion bond (gypsum layer) in the closer distance experiments, these blow-off data are not shown in this figure.

In the early stages of these experiments, when generally data were still scattered due to some sources of error, a few type A model deposits were blown off under 45° attack angle. These data are also shown in Figure 14 for comparison.

Similar results obtained for cylindrical type B deposits, as are shown in Figure 15: the higher the adhesion strength is, the closer the jet needs to be to the model deposit to remove it. In the 0° attack angle experiments, 12 model deposits with adhesion strength between 0.1 to 0.4 MPa were placed at 35 cm from the nozzle and moved to the 7.5 cm vicinity of the nozzle while the jet was activated. Despite expectations, none of these deposits were debonded by the jet. The gray-shaded box represents the adhesion strength of these deposits and the region where deposits were not removed by the jet. Some of these deposits were placed later further downstream from the nozzle, ranging from 50 cm to 90 cm to the nozzle, and were blown-off by the jet eventually. However due to the possible generation of flaws and cracks in the

adhesion bond (gypsum layer) in the closer distance experiments, these blow-off data are not shown in this figure.

The PIP of the jet and the effective jet diameter D_{ef} can be calculated based on the nozzle characteristics and the distance from the deposit [13]. The detailed procedure of how to calculate the PIP and D_{ef} at any location along the jet axis is described in Appendix B.

In Figure 16, the PIP required to debond type A deposits is plotted against the adhesion strength. Similarly, the PIP required to debond type B deposits is plotted against the adhesion strength in Figure 17. These figures show that the higher the adhesion strength, the higher the PIP required to debond the deposit from the tube surface.

4.2.1. Effects of the Deposit Shape and the Jet Angle of Attack

From Figures 14 and 15, no significant difference was observed between the results for type A and those for type B deposits. This suggests that the deposit shape does not affect the PIP required to debond deposits with equal adhesion strengths.

For both types of deposits, no significant difference was observed between the data of the 0° attack angle experiments and those of the 90° attack angle experiments (Figures 14 and 15). In case of type A deposits, despite the lack of sufficient number of data for 45° attack angle, the existing data show insignificant difference between the data for 0°, 45° and 90° attack angles. This is surprising, since it suggests that the debonding of deposits by sootblower jets

is independent of the jet angle of attack. This matter was further investigated through experiments described in §5 and §6, and further discussed in §7.

The error bars shown for each set of data in Figures 14 and 15 are equal to $\pm\sigma$ in each experiment:

$$\sigma = \sqrt{\frac{n\sum x^2 - (\sum x)^2}{n^2(n-1)}} \quad (25)$$

where n is the number of samples, which in this case is equal to three, and σ is the standard deviation. These error bars are not the errors of the measurements, but rather they represent the natural scatter of the model deposit adhesion strength. The experimental data obtained by Kaliazine et al. [5] on the adhesion strength of deposits made from actual precipitator dusts show a similar or greater degree of scattering.

Figures 16 and 17 show the jet PIP as a function of adhesion strength. The data deviates from the theoretical curve representing a mean drag coefficient $\overline{C_D} = 0.5$ for jet PIP higher than 0.02 MPa. This is due to the fact that these data were obtained at distances less than 40 cm from the nozzle. At these distances, the jet width is smaller than the width of the deposit, and the jet does not cover the whole deposit surface.

In theory, when a jet hits a deposit, two fluctuating forces will be produced on the deposit surface: F_D in the direction of flow, and F_L in the lateral direction. These forces are expressed in terms of the drag and lift coefficients, $\overline{C_D}$ and C'_L according to Equations (2) and (6),

respectively. The results obtained for both types of deposits suggest that the values of both $\overline{C_D}$ and C'_L are close to 0.5 (Figures 14, 15, 16 and 17). This value is close to $\overline{C_D}$ of a cylinder placed in a uniform flow with Reynolds numbers higher than 10^6 . The theoretical curve $\overline{C_D} = 0.5$ is shown for comparison, using Equation (22).

5. MEASUREMENTS OF THE MEAN DRAG FORCE

The scaled-down nozzle used in the blow-off experiments was designed in such a way that the experiment was practical under the laboratory conditions; thus the forces produced by the jet were limited. The deposit/tube ratio of model deposits used in the blow-off experiments was 3:1. The jet used in this experiment was unable to debond model deposits with larger tube diameter to deposit thickness (d/H) ratios because the forces produced were not large enough.

To overcome the limitations of the blow-off experiments, a new experimental assembly was designed to measure directly the drag and lateral forces acting on model deposits. The drag forces produced by the jet on the model deposits were directly measured by using a torque meter attached to the blow-off test apparatus (Figure 18). In this case, the model deposit was mounted rigidly to the tube and covered the whole length of the tube, to ensure that the total energy of the drag force was measured. The torque produced by the drag force acting on the model deposit along the jet axis was measured. The drag force was then calculated by dividing the torque by the moment arm for each deposit, which is the distance between the center of the deposit to the center of the tube.

As shown in Figure 19, four different types of deposit made from acrylic were used: type A has a flat, elongated shape with a characteristic thickness of 3.8 cm (1.5”), type B has a short, rounded shape with a diameter of 3.8 cm (1.5”), type C is similar to type A but with a characteristic thickness of 1.9 cm (0.75”) and type D is similar to type B but with a diameter of 1.9 cm (0.75”).

The torque meter was a socket extension torque sensor with a maximum capacity of 6 Nm and a frequency response of 10000 Hz. Both pressure and torque signals were 10 kHz low pass filtered and sampled at 20 kHz (Figure 20). The calibration curve for the torque meter is shown in Figure 21.

5.1. Results and Discussion

The mean drag force decay along the jet centerline axis, obtained for type A and type B, is shown in Figure 22. With a decrease in the distance between the nozzle and the deposit from 140 cm to 7 cm, the drag force for both types of deposits increases from 7 N to 59 N.

Similarly, the results for type C and type D deposits are shown in Figure 23.

5.1.1. Effect of the Deposit Shape

In Figures 22 and 23, no significant difference can be observed between results for cylindrical and elongated deposits. This is consistent with the results obtained from the blow-off experiments. The curve $\overline{C_D} = 0.5$ is shown for comparison. This value is close to $\overline{C_D}$ of a cylinder placed in a uniform flow with Reynolds numbers higher than 10^6 .

These data can be used to calculate the maximum stress generated at the tube-deposit interface using Equation (15). If the maximum stress exceeds the deposit adhesion strength, the deposit will be debonded from the tube. The maximum stress at the interface calculated based on the measured drag forces exerted on type A and type B deposits are compared with the adhesion strength obtained from the blow-off experiments for the same types of deposits in Figure 24.

5.1.2. Effect of the Deposit Size

The results for deposits with different thickness, 3.8 cm and 1.9 cm (1.5" and 0.75") for both elongated and cylindrical are shown in Figures 25 and 26.

In the regions close to the nozzle, where the jet diameter is smaller than the deposit thickness, the drag force is identical and constant for all deposits. On the other hand, in the regions where the jet diameter is larger than the deposit characteristic thickness, the drag force is

proportional to the deposit thickness; hence it is two times larger for the larger deposits. However, independent of the deposit dimensions in these regions, the drag force profiles follow the similar trend and the mean drag coefficient is close to 0.5 (where the jet diameter is larger than the deposit characteristic thickness, $x > 15$ cm and $x > 30$ cm for the 1.9-cm thick deposit and 3.8-cm thick deposit, respectively).

5.2. Measurements of the Mean Lift Force

The torque meter apparatus was used to measure the lift forces exerted on the model deposits, while the jet axis had an offset with the axis of the model deposits (Figure 27). In these experiments, the jet axis was not inline with the deposit symmetry axis (jet-deposit offset). Therefore, the velocity distribution, and hence the pressure distribution, over the deposit was not uniform. This generated a mean lift force on the deposit. The torque produced by the mean lift force acting on the model deposit along the jet axis was measured. The mean lift force was then calculated by dividing the torque by the moment arm.

The mean lift force profile along the jet centerline axis obtained for the type A model deposit, while the jet-deposit offset was 1-cm, is compared with the mean drag decay for the same deposit (Figure 28). As expected the mean lift forces are much smaller than the mean drag forces.

In the blow-off experiments, no significant difference was observed between the data of the 0° attack angle experiments and those of the 90° attack angle experiments (Figures 14 and

15). This suggested that lateral forces are as effective to remove the deposits than the drag forces are. This surprising observation could have been due to the possible misalignment of the jet-deposit axis, resulting in a jet-deposit offset, thus exerting mean lift forces on the deposits in the 0° attack angle experiments. However, the comparison between mean drag force and the mean lift force (Figure 28) shows that even with an offset equal to 1 cm, the mean lift force is much smaller than the mean drag force, therefore, a possible misalignment of the jet-deposit axis (jet-deposit offset) cannot be the reason for such a surprising observation.

6. MEASUREMENTS OF LIFT AND DRAG FORCE FLUCTUATIONS

One would expect that when a sootblower jet hits a deposit from the front, as shown in Figure 6, the lift force is much more effective in removing and debonding the deposit from the tube surface than the drag force, which pushes the deposit into the tube surface. In this case, while the contribution of the drag force to deposit debonding is limited to the produced shear stress at the tube-deposit interface; the contribution of lift or any lateral force, in addition to shear stress, extends to the normal stress generated by the torque produced by the lift force at the tube-deposit interface. There are several causes of the lift force:

- (i) **Asymmetry of the deposit shape:** deposits have irregular shapes, and are mostly asymmetric.

- (ii) **Jet-deposit offset:** If the jet axis is not inline with the deposit symmetry axis, the velocity distribution, and hence the pressure distribution, over the deposit would not be uniform. This generates a lift force on the deposit.

- (iii) Eddy vortex shedding: the flow separation from the deposit-tube assembly generates flow circulation and a wake behind the assembly, which produces a lift force acting on the deposit.
- (iv) Turbulent pulsations: the turbulent pulsations in the jet generate flow circulation, and hence, a lift force.

In this section, the attempts to measure the lift force fluctuations exerted on deposits attached to single tubes are discussed. A simple case is considered: the jet hits the deposit from the centerline while there is no offset between the jet axis and the centerline of the deposit. Finally, for theoretical discussions, the drag force fluctuations were measured and compared to the lift fluctuations

6.1. Measurements of Lift Force Fluctuations using a Torque

Meter

In these experiments, the torque meter apparatus was used to measure the lift force Fluctuations acting on model deposits (Figure 24). The jet hit the deposit from the centerline while there was no offset between the jet axis and the centerline of the deposit. The results showed that the measured signal amplitude increases as the distance from the nozzle increases (Figures 29 and 30). The recorded signals were chaotic vibrational responses to the lift fluctuations produced by the jet. However, when examined more carefully, the responses

consisted of both random and regular oscillations. The regular oscillations occurred at dominant frequencies, which were very close to the natural frequencies of the assembly (Figure 31). This suggested that the random oscillations were the lift fluctuations, while the regular oscillations were inertial effects due to the induced vibration in the assembly. This is due to the vibration of the mechanical structure that connects the model deposit (including the deposit itself) to the torque meter. As the distance from the nozzle increases, the width of the jet increases. Thus, the model deposit would be immersed more into the jet and the amplitude of the vibration would be increased as long as the energy of the jet has not dissipated completely.

The flow-induced vibrations increase with the distance mainly because of the intensification of vortex shedding. Vortex shedding is the separation of vortices from the opposite sides of an obstacle in a crossflow. It is effective only when the jet width is comparable to or larger than the obstacle dimensions. Hence, as the jet spreads with distance, vibration excitation by vortex shedding intensifies. These vibrations produce fluctuating forces on the deposit, which are in the same order as the mean drag force at distances far from the nozzle (Figure 30). This increase in vibration continues until the effect of the decrease in the jet velocity counteracts the effect of the jet spreading. Thus, vibration intensity starts to decrease further downstream.

At distances far away from the nozzle, the results obtained in the blow-off experiments showed no difference for different angles of attack (Figures 11 and 12). This is because the model deposits used in that experiment acted as cantilevers. At far distances, where the

deposits are totally immersed in the jet, the flow-induced vibrations are of the same order as the mean drag force. Therefore, the dominant force, which debonds the deposit from the tube, must be produced by these vibrations. This suggests that in kraft recovery boilers, large deposits far from the sootblower nozzle may be removed by the flow-induced vibrations as well.

These inertial forces produced by induced vibration are coupled with the lift force fluctuations. Both, the spectral characteristics of the force fluctuations and analysis of the vibration properties of the assembly are required to separate the vibration forces from the lift force fluctuations.

6.2. Flow-induced Vibration Forces Exerted on Deposits

Flow-induced vibrations may contribute to deposit debonding in the following ways:

- (i) Flexural and torsional vibrations of tubes may cause a break up of deposit-tube adhesion bond and debond deposits.
- (ii) Large deposits may act as a cantilever and vibrate under the fluctuating forces exerted on deposits by sootblower jets.

This study investigated the latter case. A simple case was considered where a large piece of deposit is attached to a fixed tube.

6.2.1 Analysis of the Response of a Vibrational System to a Randomly Fluctuating Force

A deposit-tube system can be considered as a one-dimensional system, if a single parameter, such as the instantaneous deflection $y(t)$ can describe the deformation of the whole system.

For a system with the rigidity of K , y is proportional to the constant force F :

$$K y = F \quad (26)$$

However, if the applied force is a fluctuating force $F(t)$, the deposit starts to vibrate and the governing equation would become [33]:

$$m \frac{d^2 y}{dt^2} + D \frac{dy}{dt} + K y = F(t) \quad (27)$$

where m is the mass of the deposit, D is the damping coefficient.

The vibrational motion of any complex tube-deposit configuration under different tube arrangements can be simplified into a superposition of its different vibrational modes (periodic motions with natural frequencies). Each of these modes is governed by an equation of oscillating motion similar to Equation (27). For instance, the assembly shown in Figure 27,

is subjected to torsional vibrations and the appropriate oscillating variable is the angle φ of sample deflection around the tube axis. The equation of motion has the form:

$$I \frac{d^2\varphi}{dt^2} + B \frac{d\varphi}{dt} + K\varphi = M(t) \quad (28)$$

where I is the polar moment of inertia of the tube with the sample, K is the torsional rigidity of the system (tube and torque meter), B is assembly damping and $M(t)$ is the moment of the force, produced by a fluctuating jet force.

Equation (27) can be further simplified by dividing both sides of this equation by m [33]:

$$\frac{d^2y}{dt^2} + \beta \omega_o \frac{dy}{dt} + \omega_o^2 y = f(t) \quad (29)$$

where $f(t) = F(t)/m$, $\beta\omega_o = D/m$ and $\omega_o = K/m$ are the random force per mass, the damping coefficient per mass and the first natural frequency of the system, respectively. This is the governing equation for an oscillating system under the excitation force $f(t)$. The damping coefficient β corresponds to the fraction of the vibrational energy dissipated by the assembly during one cycle of vibration.

Let us consider force $f(t)$ be a stationary random process, and let $f(t)$ be so truncated that it becomes zero outside the time interval $(-T, T)$. The Fourier integral of the truncated force $f_T(t)$ exists provided that the absolute value of $f_T(t)$ is integrable and $f_T(t)$ can be represented:

$$f_T(t) = \frac{1}{\sqrt{2\pi}} \int_{-\infty}^{\infty} A_T(\omega) e^{i\omega t} d\omega \quad (30)$$

where $A_T(\omega)$ is the Fourier transform of the function $f_T(t)$:

$$A_T(\omega) = \frac{1}{\sqrt{2\pi}} \int_{-T}^T f_T(t) e^{-i\omega t} dt \quad (31)$$

The power spectrum $p_F(\omega)$ is generally used to characterize the force $f(t)$:

$$p_F(\omega) = \lim_{T \rightarrow \infty} \frac{|A_T(\omega)|^2}{T} \quad (32)$$

The power spectrum $p_F(\omega)$ is the distribution of energy of the random force over the frequency range. In other words, the area under the power spectrum represents the mean variance of the random force $f(t)$:

$$\overline{f^2(t)} = \int_0^{\infty} p_F(\omega) d\omega \quad (33)$$

The response of the system is:

$$y(t) = \frac{1}{\sqrt{2\pi}} \int_{-\infty}^{\infty} \frac{A_T(\omega)}{Z(i\omega)} e^{i\omega t} d\omega \quad (34)$$

where $Z(i\omega)$ is the system impedance:

$$Z(i\omega) = \omega_o^2 - \omega^2 + i\beta\omega\omega_o \quad (35)$$

Impedance is a characteristic of the vibrating system, which describes its response to a periodic force. However, since the force of the jet that generates the vibrations is random, it is not possible to estimate the response of a tube or assembly explicitly, as a function of time. Fortunately, there is an effective method to analyze random fluctuating signals.

The mean value of the square of the response signal, $\overline{y^2(t)}$, can be calculated based on the power spectrum of the fluctuating force $p_F(\omega)$:

$$p_y(\omega) = \frac{p_F(\omega)}{|Z(i\omega)|^2} \quad (36)$$

or

$$\overline{y^2(t)} = \int_0^\infty p_y(\omega) d\omega = \int_0^\infty \frac{p_F(\omega)}{|Z(i\omega)|^2} d\omega \quad (37)$$

The variance of the response of a non-vibrational system can be calculated using Equations (29) and (33):

$$\overline{y_s^2} = \frac{1}{\omega_0^4} \int_0^\infty p(\omega) d\omega \quad (38)$$

where y_s is the system response to a constant force.

The vibrational amplification coefficient A_v is defined as:

$$A_v = \left(\frac{\overline{y^2}}{y_s^2} \right)^{1/2} = \left(\frac{\omega_0^4 \int_0^\infty \frac{p_F(\omega)}{|Z(i\omega)|^2} d\omega}{\int_0^\infty p_F(\omega) d\omega} \right)^{1/2} \quad (39)$$

Since the impedance Z is a characteristic of the assembly, and is independent of the excitation force, it can be obtained by simple analysis of the free vibrational response of the assembly.

Thus, β and ω_n of the assembly can be found.

If $p(\omega)$ is flat near ω_n , Equation (37) is reduced to:

$$\overline{y^2} = \frac{\pi}{2} \frac{p(\omega_0)}{\beta \omega_0^3} \quad (40)$$

This is usually the case because the function $1/Z^2$ typically has sharp maximums near natural frequencies. Thus, the power spectrum is a much smoother curve compared to the impedance curve. In this case:

$$A_v = \left(\frac{\overline{y^2}}{y_s^2} \right)^{1/2} = \left(\frac{\pi \omega_0 p(\omega_0)}{2\beta \int_0^\infty p(\omega) d\omega} \right)^{1/2} \quad (41)$$

If the power spectrum of the jet is known as a function of vortex shedding frequency, the vibrational amplification coefficient can be calculated. This coefficient is a good measure of how effective flow-induced vibration forces are compared to non-vibrational forces to remove deposits.

In the following sections, this procedure was used to determine the lift force fluctuations and the effect of flow-induced vibration.

6.3. Lift Force Fluctuation Measurement Experimental

Assembly

The vibrational response interferes with the lift force measurements as long as the first natural frequency of the experimental assembly is less than the characteristic frequency of the vortex shedding or the frequency of eddies in the jet. In addition, if the natural frequencies of the experimental assembly are low, the power spectrum of the measured signal will contain several peaks due to these frequencies. Thus, it would be extremely difficult to separate the power spectra of the lift forces from those of the induced vibration forces. The decoupling of lift forces and induced vibration forces is important because flow-induced vibration forces are

a function of deposit material and damping characteristics of the experimental assembly. Thus, the measured signal cannot be used to estimate directly the forces acting on deposits.

The torque meter assembly used in the previous experiments had a first natural frequency of about 200 Hz, whereas the characteristic frequency of the vortex shedding can be as high as 5000 Hz, depending on the deposit characteristic dimension and the jet velocity. When the jet hit the deposit attached to the torque meter assembly, the assembly vibrated with its resonant frequencies. Thus, the measured signals were couplings of the flow-induced vibration forces and the lift forces rather than purely the lift forces acting on the model deposit.

By modifying the experimental assembly and so that the first natural frequency of the assembly is shifted to a frequency higher than the maximum vortex shedding frequency, the power spectrum of the measured signal would be very close to the actual power spectrum of the lift forces. Also, the measured signal would be very close to the fluctuating lift force.

To overcome the problem of the flow-induced vibrations, a new assembly was designed (Figure 32). Since the natural frequency of axial vibrations is much higher than that of the rotational vibrations, a load cell was used to measure the fluctuating lateral forces. The load cell was a mini high accuracy universal load cell with a maximum load capacity of 450 N (100 lbf) and a frequency response of 10 kHz. A lead brick was used to anchor the apparatus. The calibration curve for the load cell is shown in Figure 33.

Preliminary experiments were carried out to measure the lift force produced by the jet on a 5-cm long type A deposit. The load cell signals were low pass filtered at 10 kHz and sampled at 20 kHz (Figure 20). The power spectra of the lift forces acting on the deposit located at 20 cm and 57 cm from the nozzle, respectively, are shown in Figure 34. Both spectra show two peaks at 1800 Hz and 6500 Hz. These correspond to the first and second natural frequencies of the axial vibration of the structure that connected the deposit to the load cell. The first natural frequency of this experiment assembly was still much higher than of the torque meter set-up (Figure 35). Meanwhile in Figure 35 the spectrum has multiple peaks that represent the natural frequencies of the torque meter assembly, whereas Figure 34 shows a much simpler relationship. Figure 34 demonstrates that the number of natural frequencies of axial vibrations of the structure was only two: 1800 Hz and 6500 Hz.

Compare the recorded power spectra at 20-cm and 50-cm from the nozzle, respectively, in Figure 34. If the area under the power spectra represents the energy of the eddies, a shift of this energy towards the lower frequencies can be observed from the power spectrum recorded at 20 cm from the nozzle to the power spectrum recorded at 50 cm from the nozzle. At 20 cm from the nozzle, the shedding frequency of the dominant eddies is much higher than at 57 cm from the nozzle. As the distance from the nozzle increases, this frequency decreases and the eddies with highest energy are produced with a lower frequency. A similar trend was observed for C_L' [34, 35]. The occurrence of just two peaks in the power spectrum made it possible to decouple the effects of the vibrational forces and lift forces by fitting proper impedance curves and deducting them from the spectrum and resolving the lift force spectra.

6.4. Separation of the Lift Force Fluctuations from the Flow-Induced Vibrations

Similar experiments were conducted to measure the lift forces exerted on 5-cm long cylindrical deposits of types B and D. A typical example of the power spectrum of the registered signal by the load cell for type B deposit is shown in Figure 36. The two distinct peaks at frequencies 1250 Hz and 5800 Hz persisted when the deposit was placed at different distances from the nozzle. Therefore, the peaks were concluded to be vibrational characteristics of the experimental assembly, and correspond to the first two natural frequencies of this assembly. The procedure described in (§5.2.1) was used to calculate the lift force fluctuations. The spectrum shown in Figure 36 is the ratio of $p_F(\omega)/|Z(i\omega)|^2$ (Equation (37)) where $p_F(\omega)$ is the power spectrum of the fluctuating random aerodynamic force exerted by the jet on the assembly and $Z(i\omega)$ is the total impedance of the assembly. The impedance of the assembly is a characteristic of the assembly alone: it is independent of jet flow properties and may be estimated independently. Therefore $p_F(\omega)$ may be restored from the experimental results. Due to the logarithmic scale, to obtain the power spectrum of the lift force $p_F(\omega)$, the impedance was subtracted from the spectrum of the raw signal $p_F(\omega)/|Z(i\omega)|^2$ in Figure 36.

For each deposit, this power spectrum was measured while deposits were placed at different distances from the nozzle (6 to 110 cm). Then, by trial and error the best total damping coefficient $\beta\omega_0$, the impedance of the assembly, was obtained as the value that best fit the

data. By deducting the impedance from the registered power spectrum, the filtered spectrum represented $p_f(\omega)$, the power spectrum of the lift force acting on the deposit. The area under the power spectrum of the lift force yields the mean square of the lift force. Thus the root mean square (r.m.s.) of the lift fluctuation for this deposit at 30-cm from the nozzle can be calculated by using Equation (33). The same procedure was repeated for every measured spectrum of forces acting on each type of deposit while deposits were placed at different distances from the nozzle. The root mean square (r.m.s.) of the lift forces were calculated from the filtered power spectrum (Figures 37, 38 and 39).

6.5. Results and Discussion

As shown in Figures 37 and 38, the restored lift forces are typically several times less than the amplitude of the registered signals. This amplification is due to coupling between fluctuating lift force and the vibrational properties of the assembly. The lift force has a wide spectrum, which is flat in the frequency range from zero to Strouhal frequency $\omega_{st}=0.4\pi U d$ in rad/sec ($f_{st}=0.2U \cdot d$ in Hz). If an assembly has a natural frequency within this range, the corresponding frequency is amplified due to resonance, and the total vibrational response grows bigger in comparison with the applied force. The degree of amplification depends on the damping coefficient and natural frequencies of the assembly.

In the vicinity of the nozzle, despite the decrease in the peak impact pressure, the flow-induced vibration forces grow with increasing distance from the nozzle (Figures 37 and 38).

This phenomenon was previously observed (Figures 29 and 30). Vibrations increase with distance because of the intensification of vortex shedding as the jet spreads with distance. Maximum vibrations were observed at a distance of about 45-50 nozzle diameters downstream of the nozzle (about 40 cm from the nozzle) for both deposits. At this distance, the jet diameter was approximately equal to the thickness of larger deposit. Further downstream, the reduction of the jet PIP and velocity counteract the effect of increased jet width, and the vibration intensity drops. In Figures 37 and 38, curves representing a lift coefficient $C'_L \approx 0.1$ were shown for comparison. The value of $C'_L = 0.5$, reported in the previous section (§4.2.1.), included the effect of flow-induced vibration forces [36]. For large distances, where the samples were completely immersed in the jet, the data are very close to these curves. The fluctuation lift force profiles for both deposits show the same trend: a peak at a distance about 45-50 nozzle diameters downstream (Figure 39).

Since deposits in boilers are built usually on the leading edge of tubes and platens and grow in the jet flow direction, the lateral forces are usually the more effective forces, which debond and remove deposits. This is due to the contribution of moments exerted on deposits by these forces to the maximum principal stress generated at the tube-deposit interface.

6.6. Measurements of Drag Force Fluctuations

To investigate the effects of drag fluctuations and resultant flow-induced vibration forces on debonding, similar experiments were conducted on types B and D deposits using the same load cell assembly (Figure 32). Deposit orientations with regard to the jet axis were changed

in a way that the load cell measured the fluctuating drag forces (Figure 40). The results for type B deposits are shown in Figures 37 and 38. Similar to the lift force measurements, the registered forces are much larger than the restored drag forces (calculated using Equation (33)) (Figure 41). In Figure 38, the r.m.s. of the drag force fluctuations are compared with the r.m.s. of the lift fluctuations. The drag force fluctuation profile is much flatter, and although the maxima of both profiles are located at a distance about 45–50 nozzle diameters downstream (about 40 cm from the nozzle), the maximum of the lift force fluctuation profile is 2.5 times larger than that of the drag force fluctuation profile. This means that the flow-induced vibration forces due to the lift fluctuations must be much larger than those produced by the drag fluctuations.

7. IMPLICATIONS

The experimental data discussed in previous sections were obtained from laboratory experiments that measured the forces exerted on deposits attached to a single tube. The 4:1 scaled-down nozzle used in these experiments is dynamically similar to a fully expanded 1¹/₈-inch exit diameter steam sootblower nozzle, which operates at 350 psig. Therefore, the PIP of this nozzle at a distance x_0 from the nozzle represents the PIP of a full-scale sootblower nozzle at a distance $4 x_0$ from the sootblower nozzle exit. The dimensionless lift fluctuation coefficient C'_L and mean drag coefficient \overline{C}_D should be identical for laboratory conditions and full-scale boiler conditions. Hence, drag and lift fluctuations and mean drag forces measured in the laboratory may be used to estimate the corresponding forces exerted on fireside deposits by sootblower jets under actual boiler conditions. Using these forces, the maximum stress generated at the tube-deposit interface by vibrational effects can be estimated.

In the following sections, the experimental results are used to estimate typical forces exerted on deposits accumulated on tubes of generating banks and platens. Attempts are made to use

these estimates to make quantitative predictions about the removal of fireside deposits by sootblower jets in boilers.

7.1. Implication of Mean Drag Force Measurement Results

Due to geometric and dynamic similarities, the drag force exerted by sootblower jet on a deposit in a recovery boiler can be evaluated based on the results obtained in mean drag force measurements in the laboratory (§5). This can be done using Equation (2) and the geometrical scale factor 1:4, since the dimensionless drag coefficient $\overline{C_D}$ is identical for both laboratory conditions and kraft recovery boiler conditions.

Figures 43 and 44 show the drag force decay of a sootblower jet hitting deposits with characteristic thickness of 15.2 cm and 7.6 cm (6" and 3"), respectively, in a recovery boiler. These results are evaluated based on the laboratory experimental results for model deposits. The distance between a sootblower nozzle and the first and last tubes in a superheater platen is approximately 20 cm and 180 cm, respectively. In the above figures, a 32-tube superheater platen is shown for comparison (the sootblower nozzle is located on the vertical axis). These results suggest that drag forces of 800 to 1000 N would act on deposits with characteristic thickness of 15.2 cm and 7.6 cm (6" and 3"), respectively, if these deposits are built up at the inlet of the superheater platen.

In general, the drag force exerted on deposits with arbitrary thickness and the stresses generated at the interface can be evaluated based on the results obtained from dynamically similar laboratory experiments described in this study. The effectiveness of the sootblower to debond the deposit from the tube can then be predicted if the adhesion strength is known.

The stress generated at the tube-deposit interface by drag forces is discussed and compared with those generated by lift fluctuation forces in the following sections.

7.2. Implication of Force Fluctuation Measurement Results

In the following sections the implication of results of the force fluctuation measurements is discussed.

7.2.1. Similarity of Force Spectra

To apply the laboratory experimental data of fluctuating forces to the conditions relevant to a recovery boiler, the extracted power spectra of the fluctuating forces should be properly scaled. This force spectrum can then be combined with the vibrational characteristics of the boiler tubes to calculate the resulting stresses on the deposits. The scales should be a function only of flow velocity, jet fluid properties and deposit-tube geometry. Equations (6) and (33) suggest that the proper scaling factor for the lift force power spectrum is the kinetic energy of the flow. Hence,

$$\overline{f_d^2(t)} = \left(\frac{2}{\rho U^2 HL} \right)^2 \int_0^\infty p_F(\omega) d\omega \quad (42)$$

where $f_d(t)$ is the dimensionless lift force that should be invariant and L is the length of the experimental deposit. The most appropriate dimensionless time scale arises from the Strouhal frequency, $\omega_{st} = 0.4\pi U/d$, where d is the diameter of the tube-deposit. Hence, the frequency variable in the power spectrum, ω , should be nondimensionalised as $s = \omega / \omega_{st}$. Thus, the power spectrum for the sootblower jet and the laboratory jet should have exactly the same power spectrum when represented in terms of s . Thus, to extrapolate the experimental data to the conditions of boilers, the spectra were plotted in the dimensionless form. The dimensionless power spectrum $p(s)$ was calculated from the following equations:

$$p(s) = p_F(\omega) \frac{0.4\pi \frac{U}{d}}{\left(\frac{\rho U^2}{2} HL \right)^2} \quad (43)$$

$$s = \frac{\omega}{\omega_{st}} \quad (44)$$

the area under the power spectrum $p(s)$ is equal to $(C'_L)^2$. If the dimensionless frequency s is properly scaled, using $p(s)$, one should be able calculate the resultant power spectrum for any size of deposit hit by a jet at any velocity.

Similarly, if the random force $f(t)$ in Equation (33) is a fluctuating drag force acting on a cylinder:

$$p(s) = p_F(\omega) \frac{0.4\pi \frac{U}{d}}{\left(\frac{\rho U^2}{2} dL\right)^2} \quad (45)$$

$$s = \frac{\omega}{\omega_{st}} \quad (46)$$

The extracted (computed) lift force power spectra are relatively smooth functions of frequency (Figure 36). The normalized extracted lift force power spectra $p(s)$ for types B and D deposits are plotted for distances greater than 40 cm from the nozzle in Figures 45 and 46, respectively. At these distances, both of the deposits were fully covered by the jet, and the power spectra were similar. In accordance with theory, the extracted spectra are self-similar functions. This means the dimensionless power spectrum $p(s)$ is a unique function for deposits with different thickness and different jet velocity. This confirms that the dimensionless frequency s is the proper scale. These data show a high degree of similarity. They cover jet velocities from 85 to 245 m/s and Strouhal frequencies from 450 to 1280 Hz. The differences between spectra that can be observed at higher frequencies are instrumental effects caused by the relatively different levels of noise occurring in large and small signals. On the other hand, at very small distances from the nozzle, power spectra are only slightly different and deviate from similarity because the jet diameter was smaller than the thickness of deposits.

The best fitted curves for the dimensionless power spectra for types B and D are $p(s)=177828*\exp(-s^2/1.26^2)$ and $p(s)=316228*\exp(-s^2/0.89^2)$, respectively, while $s<3$. The differences between best fitted-curves and these spectra for $s>3$ do not play an important role in the flow-induced vibration calculations because the energy of lift force fluctuations at these frequencies is negligible.

The maximum energy of the lift force, occurs in the region $s<1$. As shown in Figures 45 and 46, the power spectra are almost flat for the frequencies below $s=1$ ($\omega=\omega_{st}=0.4\pi U d$), and drop drastically at frequencies higher than $s=1$. These spectra could be fitted into $p(s)=p_0*\exp(-\omega^2/\omega_v^2)$, where $\omega_v=0.494\pi U/d$ is a characteristic frequency close to the Strouhal frequency, and p_0 is a constant. Equation (41) shows how to calculate a vibrational response to a random force having known power spectrum. If the system has a natural frequency ω_0 and damping coefficient β , then its vibrational response increases in proportion to amplification A_v :

$$A_v = \left(\sqrt{\pi} \frac{1}{\beta} \frac{\omega_0}{\omega_v} \exp\left(-\frac{\omega_0^2}{\omega_v^2}\right) \right)^{1/2} \quad (47)$$

The maximum amplification A_{vmax} occurs when $\omega_0 = 2^{1/2} \omega_v$ and is equal to:

$$A_{vmax} = \left(\frac{\pi}{2e} \right)^{1/4} \frac{1}{\sqrt{\beta}} = \frac{0.872}{\sqrt{\beta}} \quad (48)$$

This means that flow-induced vibration increases the effect of the lift force by a factor of $0.872/\beta^{1/2}$.

This is an interesting conclusion: the maximum vibration amplification is just a function of the damping coefficient β as long as any of the natural frequencies of the deposits are close to the Strouhal frequency ω_{st} . In this case, the deposit vibration will be amplified in inverse proportion to the damping coefficient of the deposit-tube composite. Since deposit strains are directly proportional to vibration amplitude, an increase in deposit vibration amplitude increases strain. This increase in deposit strain, increases the stress at the tube-deposit interface. Thus, the vibration of a deposit can significantly amplify the stress generated at the deposit-tube interface, as long as one of the deposit-tube assembly natural frequencies is close to the Strouhal frequency of the impinging jet.

Since the power spectrum is flat for frequency less or equal of the Strouhal frequency ($s < 1$), if one of the natural frequencies of the system occurs in this region, it causes a vibration amplification equal to $A_{v_{max}}$. This requirement is not very restrictive. Deposits built on a tube surface, depending how the tube is fixed at its ends, establish different vibrational systems with different degrees of freedom and many natural frequencies. Thus, it is very likely that one of the natural frequencies is lower than the Strouhal frequency ($s < 1$): if one can assume that this condition exists, the maximum stress generated at the tube-deposit interface depends on β , the tube-deposit interface area, the deposit thickness and an estimate of the magnitude of the r.m.s. of lift force fluctuations.

† In fact, as long as one of the natural frequencies of the deposit-tube composite structure is lower than 1.5 times of the Strouhal frequency ($s < 1.5$), vibrations would have a significant effect on the lift fluctuations; because for frequencies less than $s = 1.5$, the area under power spectra contains almost 80% of the lift fluctuation energy, and vibration amplification still could be estimated base on A_{Vmax} .

7.2.2. Comparison with Blow-Off Results

The r.m.s of lift force fluctuations for types B and D deposits are plotted in Figures 37 and 38. Based on these data and by using the dynamic similarity principle, the lift force profiles of a sootblower jet hitting deposits with characteristic thickness of 15.2-cm and 7.6-cm, respectively, can be estimated (similar to Figures 43 and 44). Based on these estimates and by using Equation (19), the profiles of stress generated at the tube-deposit interface can be calculated. Now, if the damping coefficient β is known, the profiles of the maximum stress generated at the tube-deposit interface due to the flow-induced vibrations can be computed by multiplying these profiles by the maximum vibrational amplification factor $A_{Vmax} = 0.872 \cdot (\beta)^{1/2}$. The criterion for deposit debonding indicates that if these stresses exceed the deposit adhesion strength the deposit will be removed.

The damping coefficient β is the energy loss coefficient of the vibrational system, and it is the ratio of the energy dissipated in the system during one cycle of vibration to the total vibrational energy [37, 38]. Damping is sensitive to the structure. Slight differences in

compositions, mechanical features such as mechanical joints in the system, thermal treatment and mechanical processing can lead to significantly different results for damping coefficients of the similar systems made of the same material. A large amount of data on damping properties for test specimens from different materials can be found in reference [37]. The value of β for test specimens made of different materials ranges from 10^{-3} to 0.9.

The damping coefficient β data are very limited and correspond to specific experimental conditions. The exact damping coefficient of the tube-deposit system used in the blow-off experiments is not known. However, an attempt was made to measure the natural frequency and the damping coefficient of the deposit-torque meter assembly (Figure 27). For this purpose, free assembly vibrations were recorded. In the absence of external forces, vibrations gradually died out. Figure 47 shows the registered decay of a free torsional vibration of the assembly. The natural frequency of the assembly was close to 189 Hz. The rate of vibration decay yields a damping coefficient β of approximately 0.018.

Although the tube-deposit system in the blow-off experiments is different from the torque-meter assembly, both systems have similar configuration and go through torsional vibrations under similar fluctuating forces. Thus, for comparison purposes only, the measured damping coefficient β of the deposit-torque meter assembly can be used to compare the generated stress by the lateral flow-induced vibrations at the tube-deposit interface with data obtained from the blow-off experiment.

By using the above values of β , Equations (19) and (48), and following the procedure described in §3.5.1, the maximum stress at the tube-deposit interface calculated based on the measured drag force and computed r.m.s. of lift force exerted on type B deposit are compared with the adhesion strength obtained from the blow-off experiments for the same type of deposit (Figure 48). Despite the relatively large scatter of the blow-off experiment data, a common trend can be observed. At distances less than 35 cm from the nozzle no deposits were blown off, it is speculated that this is because the jet diameter in this region is smaller than the deposit thickness. Hence, the main cause of fluctuating forces, which is vortex shedding, is suppressed, and vibration effects are minimized and vibrational forces are too small to generate enough stress to exceed the adhesion strength of the deposit. In this region, the drag force is mainly pushing the deposit onto the tube. The profiles of stress based on different values of β indicate that the values of generated stress at distances less than 35 cm are on the same order as those at distances greater than 80 cm from the nozzle. In the blow-off experiments, the nozzle was moved from distances far from deposits towards them until they were blown off. At distances between 40 to 60 cm from the nozzle, the lift forces and vibrational forces reach their maximum, and this is where the deposits with higher adhesion strength were removed. As shown in Figure 14 and Figure 15, a few model deposits with adhesion bond strength approximately equal to those blown-off in distances 40 to 60cm, were initially placed at distances less than 35 cm from the nozzle, but were not removed by the jet. Had these samples initially been placed 40-60 cm from the nozzle, they could have been removed by the jet.

Further downstream, at distances larger than 60 cm, as the effect of vibration decreases and the effect of PIP and velocity dominate, the stress decreases. The profile of the stress generated just by the r.m.s. of lift forces are shown for comparison. As shown, this profile cannot in any way explain the deposit removal data. It may be interesting to note that the reported values of β for systems which partially are made of wood and go through torsion or bending stresses due to flow-induced vibrations, are very different and cover a wide range from 6.7×10^{-3} to 1.6×10^{-2} . As mentioned before, the blow-off data are scattered mainly due to the natural scatter of the deposit adhesion strength (§4.).

Similar to Figure 48, the r.m.s. of drag fluctuations along with the registered mean drag forces, and the estimated β of the deposit-torque meter system were used to calculate the maximum stress generated at the tube-deposit interface due to the drag forces and resultant flow-induced vibration forces exerted on type deposits. The results are compared to the blow-off experiments in Figure 49. The calculated stresses are in good agreement with the blow-off experiments. The drag fluctuations and the resultant vibration forces add 20% to the stress generated by the mean drag force (mean drag effect).

As mentioned before, the available data for the damping coefficient β of different vibrational systems reported in the literature cover a wide range from 0.001 to 0.9. Thus, the amplifications of stresses due to vibration for different systems under identical force fluctuations may be very different. Generally if the damping coefficient β is in the range of the range of 0.1 to 0.01, the amplification of stress due to vibration might be expected to be in

the range of 3 to 10. It should be noted that the damping coefficient β is a characteristic of the whole vibrational system, and it is not just a function of material.

7.2.3. Stress Generated at Tube-Deposit Interface in Recovery Boilers

In the laboratory experiments, the forces exerted on deposits attached to a single tube were studied. However, in a boiler the jets remove deposits from different arrangements of tubes, e.g. generating bank or platens. Depending on the tube arrangement, the sootblower jet flow is disturbed by other tubes in many situations. Hence, to estimate the flow-induced vibration under boiler conditions these effects must be taken into account.

There are no data regarding the effect of the flow confinement on the lift fluctuation generated by a supersonic jet. The few available data for uniform flow suggest that the lift fluctuations may increase with distance into a generating bank.

There are also no data reported for tubes covered with fireside deposits in boilers. The damping coefficients of tubes of the generating banks or platens in boilers depend on tube length, type of the suspension and supports, intermediate supports and vibration bars, mass and plasticity of the accumulated deposit on the tube. For 10 to 20-meter long, hanging tubes with no intermediate support, this coefficient can be as small as 0.001 [36]. Although, boiler manufacturers try to minimize the use of intermediate tube supports to avoid the

accumulation of deposits, the addition of intermediate supports and vibrational bars may increase this value to about 0.01. The damping coefficient of tubes covered by deposits might be comparable to the damping coefficient of clean tubes with intermediate supports.

Figure 50 shows the profiles of the maximum stress generated at the tube-deposit interface, when the sootblower jet hits a 15.2-cm (6-inch) thick deposit accumulated on tube in a boiler. These data are estimated based on the measured laboratory data of lift and drag forces for 3.81-cm (1.5-inch) cylindrical model deposits (type B), assuming that the deposits cover half of the tube and using a geometrical scale factor equal to 4. The effect of lateral flow-induced vibrations on the maximum stress generated by lift fluctuations at the tube-deposit interface are plotted for three different values of damping coefficient ($\beta = 0.001, 0.01$ and 0.03). Two jet attack angles are considered: 90° (Mean Drag Force Effect) and 0° (Lift Force Effect). For each jet attack angle, the maximum stress generated at the tube-deposit interface is calculated using both Equation (19) and Equation (16). In the stress calculations using Equation (19) the effects of drag force, lift force fluctuations and their amplification due to flow-induced vibration were taken into account (combined stresses), whereas in the stress calculation using Equation (16) the effects of vibrational forces and the mean drag force are neglected for the 90° and 0° attack angles, respectively.

In each of these calculations the procedure described in §3.5.1 was followed: for each distance from the nozzle, the principal stress distribution at the tube-deposit interface was calculated from either Equation (19) or (16) as a function of α where $\alpha_0 < \alpha < \alpha$, then the maximum value of this stress was chosen as the maximum principal stress. The Poisson's

ratio ν for the fireside deposits is not known. However, for materials similar to fireside deposits, ν is about 0.22 [37]. Hence, this value was used in these calculations.

There is no significant difference between the maximum principal stresses calculated by Equations (19) and (16). At the 90° angle of attack, the effect of taking into account the stress due to lift fluctuations is negligible. At the 0° angle of attack orientation, the stresses generated by the drag force decreases the combined maximum principal stress slightly. This can be explained the following: at the 0° angle of attack, the mean drag force generates compressive normal stress and shear stress (due to the curved surface of the tube) at the tube-deposit interface. The compressive normal stress pushes the deposit onto the tube and resists the debonding, whereas the shear stress helps the deposit to debond from the tube surface. Thus, these two stresses counteract each other. Depending on the size of the covered sector of the tube by the deposit, these shear and compressive stresses may counteract each other effects in the debonding process.

At the 90° attack angle, the dominant force which causes debonding is the mean drag force, whereas at the 0° attack angle, the dominant forces are the lateral forces caused by the flow-induced vibrations. The profile of stress generated by the mean drag force at the tube-deposit interface at the 90° attack angle is similar to the jet peak impact pressure profile; it decays and decreases with distance from the nozzle. However, the force fluctuations increase and reach a maximum value at a location about 160 cm from the nozzle, where the jet becomes subsonic. Further downstream, the fluctuations dissipate and the effect of the mean drag force prevails. As shown in Figure 50, the amplification of the stress generated by the lift force due to flow-

induced vibration can be dramatic, depending on the damping coefficient of the deposit-tube assembly (Vibrational Effect 0°). For a damping coefficient $\beta = 0.001$, the effect of vibration can increase the maximum stress generated by the lift force at the 0° attack angle, to values well above those generated by the mean drag force in the 90° . In other words, under these conditions the fluctuating lift force can remove much stronger deposits than the jet mean drag force. However, as discussed, a damping coefficient of about $\beta = 0.01$ for the deposit-tube assembly seems to be more realistic. In this case, vibrations can be seen to have an effect comparable to the mean drag effect at large distances. This is consistent with the results obtained from blow-off experiments (Figures 14 and 15): in that no significant difference was observed between the data for the 90° and 0° attack angle orientations at distances further than 40 cm from the nozzle.

Similarly, Figure 51 shows the profiles of the maximum stress generated at the tube-deposit interface, when the sootblower jet hits a 5-cm (2-inch) thick deposit accumulated on a tube in a boiler. These data are estimated based on the measured laboratory data of lift and drag forces for 3.81-cm (1.5-inch) cylindrical model deposits (type B), assuming that the deposits cover half of the tube. The effect of lateral flow-induced vibrations on the maximum stress generated by lift fluctuations at the tube-deposit interface is shown for three different values of damping coefficient ($\beta = 0.001, 0.01$ and 0.03). Two jet attack angles are considered: 90° (Mean Drag Force Effect) and 0° (Lift Force Effect). For each jet attack angle, the maximum stress generated at the tube-deposit interface is calculated using Equation (19).

As shown in Figure 51 and similar to the case of the 15.2-cm (6-inch) thick deposit, for a damping coefficient $\beta = 0.001$, the effect of vibration increases the maximum stress generated by the lift force in the 0° attack angle to values well above those generated by the mean drag force in the 90° attack angle. For a damping coefficient $\beta = 0.01$, vibrations can be seen to have an effect comparable to the mean drag effect at large distances.

7.3. Transition Time

The assumption of steady state conditions was used in all the experiments and corresponding previous analysis of vibrational response of a system to a fluctuating force. It was assumed that the fluctuating force affects the system long enough that any influence of the initial conditions disappears and the system responds to the force with random but stationary vibrations. In practice, when a sootblower jet hits deposits accumulated on a tube, it takes some time for vibrations to be developed and reach their stationary amplitudes. The characteristic time required to develop a stationary response is called a transition time. The theory of random vibrations shows that transition time T of a system with characteristic frequency ω_0 and damping coefficient β is [36]:

$$T \approx 1/(\beta\omega_0) \quad (49)$$

When a sootblower jet hits a deposit and generates vibrations, the maximum vibrational response is generated at a frequency close to the Strouhal frequency of the jet flow:

$\omega_0 \approx \omega_s \approx U/d$ where U is the velocity of the jet and d is the deposit thickness. Hence, transition time for a deposit blown by a sootblower is:

$$T \approx d/(U\beta) \quad (50)$$

A typical sootblower has a travel speed of 0.04 m/s, a rotation speed of 25 rpm. A sootblower sweeps deposits from the tube surface, therefore, the jet-deposit interaction time is in the order of seconds. For the typical values of $U=300\text{m/s}$, $d=5\text{ cm}$ and $\beta=0.01$, the transition time is $T=0.016\text{ s}$. This time is much less than a typical time of the interaction of a sootblower jet with the deposit in all locations of the boiler, which is on order of seconds. Therefore, the steady state approach is valid for estimating vibrational responses of tubes to a sootblower jet, and the estimated stresses based on the laboratory data are valid.

8. CONCLUSIONS

Laboratory experiments were carried out to measure fluctuating drag and lift forces exerted on model deposits. The effect of flow-induced vibration and deposit shape were studied also.

The major findings of this can be summarized as follows:

MEAN DRAG FORCE EXPERIMENTS:

- If the jet diameter is larger than the deposit thickness, the mean drag force generated by the sootblower is proportional to the deposit thickness: the larger the deposit the larger the force.

- For elongated and cylindrical deposits with equal thickness, the jet produced the same drag and lateral forces.

FORCE FLUCTUATION EXPERIMENTS:

Flow-induced vibration forces caused by lift fluctuations may be the dominant lateral forces which debond deposits:

- While the jet peak impact pressure and mean drag force decrease as the distance from the nozzle increases, the lift force fluctuations and flow-induced vibrations behave differently: as the distance from the nozzle increases, first lift force fluctuations and flow-induced vibrations increase to reach their maxima at a distance about 45-50 nozzle diameters downstream. This is due to the intensification of vortex shedding as the jet spreads with the distance. Further downstream, the reduction of the jet peak impact pressure and velocity counteract the effect of increased jet width and vibration intensity drops. Thus, lift fluctuation and flow-induced vibrations start to decrease with further increase in the distance from the nozzle.

- To conduct laboratory deposit blow-off experiments, one should take into account the effect of flow-induced vibrations produced by the jet. The damping coefficient β and natural frequencies of the whole deposit/tube system should be known, before any precise comparison between the results of blow-off experiments under different jet attack angles can be made.

- The maximum lift fluctuations are about 2.5 times larger than the maximum drag fluctuations. Therefore, flow-induced vibrations are much larger in the lateral direction than in the flow direction.

- The dimensionless power spectra of the lift forces exerted on cylindrical deposits were plotted. These spectra have a high degree of similarity, and could be fitted into $p(s)=p_0 \cdot \exp(-\omega^2/\omega_v^2)$, where $\omega_v=0.494\pi U/d$ is a characteristic frequency close to the Strouhal frequency, and p_0 is a constant. Furthermore, to predict deposit removal by debonding, these spectra can be scaled to determine the power spectra of lift forces exerted on deposits built on tube surfaces in a boiler.

- The possibility of removal of deposits by debonding is enhanced significantly by flow-induced vibrations: the flow-induced vibration increases the effect of the lift force fluctuations by a maximum factor of $0.872 \beta^{0.5}$. Thus, the vibration of a deposit can significantly amplify the stress generated at the deposit-tube interface, as long as one of the natural frequencies of the deposit-tube assembly is close to the Strouhal frequency of the turbulent jet.

- A procedure has been developed to determine the fluctuating drag and lift forces exerted on deposits by a turbulent jet based on the present laboratory results. Additional data, which define the vibrational characteristics of the deposit-tube system in the boiler, are required to more precisely quantify the effect of vibrations on deposit removal.

9. RECOMMENDATIONS FOR FUTURE WORK

This section provides a list of research activities recommended to improve the understanding of the deposit debonding mechanism.

In the laboratory experiments, the forces exerted on deposits attached to a single tube were studied. Meanwhile, the jet axis was aligned with the centerline of deposits with no offset between the jet axis and deposit centerlines. In addition, just two attack angles were studied: 90° and 0° . However, in a boiler, sootblower jets hit deposits accumulated on generating bank tubes or platen tubes under various attack angles and with an offset from deposit centerlines or axis due to the sootblowers' linear and rotational movements. To have a better understanding of the deposit debonding mechanism and what would be the effects of different conditions of sootblower jets interaction with deposits in boilers the following experiments are recommended:

- Measurement of mean lift force exerted on the model deposit attached to a single tube, while there is an offset between jet axis and deposit centerline. This way the optimum offset between the sootblower nozzle and the deposit can be investigated.

- Measurement of the mean lift and mean drag forces exerted on the model deposit attached to a single tube under different attack angles to calculate the maximum stresses at the tube-deposit interface.

- Measurements of the lift and drag forces on model deposits attached to tubes in generating bank arrangements and platen arrangements, using the torque meter: to determine the effect of flow confinement on drag and lift forces. In this experiment, the effect of jet axis offset with deposit centerline may also be investigated.

- Measurements of the damping coefficient and vibrational characteristics of tube-deposit assemblies under boiler operating conditions.

REFERENCES

1. Tran, H.N., *How does a kraft recovery boiler become plugged*, TAPPI Journal. pp. 102-106, 1986.
2. Adams Terry N., Frederick Wm. James, Grace Thomas M., Hupa Mikko, Lisa Kristiina, Jones Andrew K. and Tran Honghi, ., *Kraft Recovery Boilers*, TAPPI Press, Chapter 9, 1997.
3. Tran H.N., *Kraft Recovery Boiler Plugging and Prevention*, TAPPI Kraft Recovery Operations Short Course, TAPPI Press, pp. 209-217, 1992.
4. Piroozmand, Farshad, Master of Science Thesis, University of Toronto, 1997.
5. Kaliazine A., Cormack D.E., Ebrahimi-Sabet A. and Tran H.N., *The Mechanics of Deposit Removal in Kraft Recovery Boilers*, Journal of Pulp and Paper Science:Vol.25 No. 12, pp. 418-424, December 1999.
6. Reeve D.W., Tran H.N. and Barham D., *The Effluent-Free Bleached Kraft Pulp Mill. Part XI: Chemical and Thermal Properties of Recovery Boiler Superheater Fireside Deposits*, Pulp and Paper Canada, 82 (9) T315, 1981.
7. Tran H.N., Reeve D.W. and Barham D., *Formation of Kraft Recovery Boiler Fireside Deposits*, Pulp and Paper Canada, 84 (1) T7, 1983.
8. Isaak P., Tran H.N., Barham D. and Reeve D.W., *Stickness of Kraft Recovery Unit Fireside Deposits*, Journal of Pulp & Paper Science, Vol. 12, No.3, May, J84, 1986.
9. Isaak P., Tran H.N., Barham D. and Reeve D.W., *Stickness of Kraft Recovery Unit Fireside Deposits – Part II. The Effect of Potassium and Surface Treatment*, Journal of Pulp & Paper Science, Vol. 13, No.5, September 1987.
10. Backman R., Hupa M. and Uppstu P., *Fouling and Corrosion in Recovery Boiler Superheater Area*, TAPPI Journal, 70 (6) 123, 1987.

11. Tran H.N., Barham D. and Reeve D.W., *Sinetering of Deposits and Its Impact on Plugging in Kraft Recovery Units*, TAPPI Journal, 70 (4) 109, 1988.
12. Borg A., Teder A., and Warnqvist B., *Tappi* 57(1): 126, 1974.
13. Jameel, M.I., Cormack, D.E., Tran, H.N., Moskal, T.E., *Sootblower Optimization*, TAPPI Journal, 77(5): pp. 135-142, 1994.
14. Jameel, M.I., Schwade, H., *A field Study on the Operational Impact of Improved Sootblower Nozzles on Recovery Boilers*, Proceedings of TAPPI Engineering Conference, pp. 695-704, 1995.
15. Kaliazine, A, Cormack, D.E., Tran H.N., Piroozmand, F., *Sootblower Optimization- Part 2*, Proceedings of TAPPI Engineering Conference, Chicago. pp. 427-433, 1996.
16. Bunton, Mark A., Moskal, Thomas E., *Increasing Boiler Efficiency through sootblower optimization*, Proceedings of TAPPI Engineering Conference, pp. 707-712, 1995.
17. Chappel, R.E., *A basic Understanding of Sootblowing For Recovery Boiler Cleaning*, Kraft Recovery Operations Seminar, TAPPI Press, pp. 185-189, 1988.
18. Achenbach E., Heincke E. On vortex shedding from smooth and rough cylinders in the range of Reynolds numbers $6 \cdot 10^3$ to $5 \cdot 10^6$. *J. Fluid Mech.* Vol. 109, pp. 239-251, 1981.
19. Mair W.A., Beavan J.A, Flow past airfoils and cylinders. In: *Modern Developments in Fluid Mechanics High Speed Flow*. Ed. Howarth L, Oxford Univ. Press, 1959.
20. Rouse, H, Howe, J.W., *Basic Mechanics of Fluids*. John Wiley & Sons, Inc., New York, 1966.
21. Naudascher E. *Hydrodynamic forces*. A.A. Balkema, Rotterdam, 1991.
22. Chen J.C.K., Melbourne W.H., Turbulence effects on some aerodynamics parameters of a circular cylinder at supercritical Reynolds numbers. *Journal of Wind Engineering and Industrial Aerodynamics*. Vol. 14, p. 399, 1983.
23. Ferri A, Influenza del numero di Reynolds ai grandi numeri di Mach. *Atti Guidonia*, nos. 67, 68, 69, 1942.
24. Fage A, *British Aeronaut. Research Comm. R&M*, 1369, 1931.
25. Zukauskas A., Ulinskas R., Katinas V, *Fluid dynamics and flow-induced vibrations of tube banks*. Hemisphere Publishing Corporation, 1988.

26. Chen Y.N., Fluctuating Forces of the Karman Vortex Streets on Single Circular Cylinders and in Tube Bundles. Part 1-3. *Journal of Engineering for Industry*. Vol. 94, No. 2, pp. 603-630, 1972.
27. Richter A., Naudascher E, Fluctuating forces on a rigid circular cylinder in confined flow. *J. Fluid Mech.* Vol. 78, pt. 3, pp. 561-576, 1976.
28. Oengoeren A., Ziada S., Unsteady fluid forces acting on a square tube bundle in air cross flow. *Symposium on Flow-Induced Vibration and Noise*. Vol. 1, pp. 55-74, 1992.
29. Taylor C.E., Pettigrew M.J., Axisa F., Villard B., Experimental determination of single and two-phase cross flow-induced forces on tube rows. *Trans. ASME*. Vol. 110, pp. 22-28.
30. Tran H.N., Elliot M., Barham D., and Reeve D.W., *Pulp Paper Can.*, 87(7): T278, 1986.
31. Kaliazine A., Cormack D.E., Ebrahimi-Sabet A. and Tran H.N., *The Mechanics of Deposit Removal in Kraft Recovery Boilers*, Proc. Intl. Chem. Rec. Conf., Tampa, FL., Vol. 2: pp. 641-654, 1998.
32. Shigly J.E., Mishke C.R., Standard handbook of machine design, McGraw Hill, N.Y., 1996.
33. Fung Y. C., *An Introduction to The Theory of Aeroelasticity*, Dover Publications Inc., Mineola, N.Y., 1995.
34. Chen S. S. and Jendrzejczyk J. A., *Fluid Excitation Forces Acting on a Square Tube Array*, Journal of Fluids Engineering, Vol. 109, December 1987.
35. Mulcahy T. M., *Design Guides for Single Circular Cylinder in Turbulent Crossflow*, ANL- CT-82-7, Argonne National Laboratory, Argonne, IL, 1982.
36. Belvins, Robert D, *Flow-induced Vibration*, Litton Educational Publishing, Inc., 1990.
37. Lazan, Benjamin J., *Damping of Materials and Members in Structural Mechanics*, Pergamon Press Ltd., London 1968.
38. Kurtze G., *Physik und Technik der Laermbekaempfung*, Verlag G. Braun, Karlsruhe, 1964.
39. Kleinstein G.J., *Space Kraft*, 1 (4): 403, 1964.
40. Witze P.O., *Generalized theory for the turbulent mixing of axially symmetric compressible free jets*, in Fluid Mechanics of Mixing, Proceeding of Joint Meeting of The Fluids Engineering and Applied Mechanics Div., ASME, Atlanta, 1973.

TABLES

Table 1. Comparison between the fully expanded sootblower nozzle and the laboratory nozzle.

	Boiler	Model
Tube diameter, cm	5.08 (2")*	1.27
Nozzle exit diameter, cm	2.85 (1 ¹ / ₈ ")	0.735
Nozzle gas	Steam	Air
Mass flow, kg/s	0.50	0.10
Nozzle pressure, psi	340	800
Nozzle exit velocity, m/s	1095	627
Exit gas density, kg/m ³	0.66	3.79
Exit Mach number, Ma	2.59	2.75
Exit Reynolds number, Re	1.81·10 ⁶	1.65·10 ⁶

*: These data are based on the tubes used in superheater platens.

FIGURES

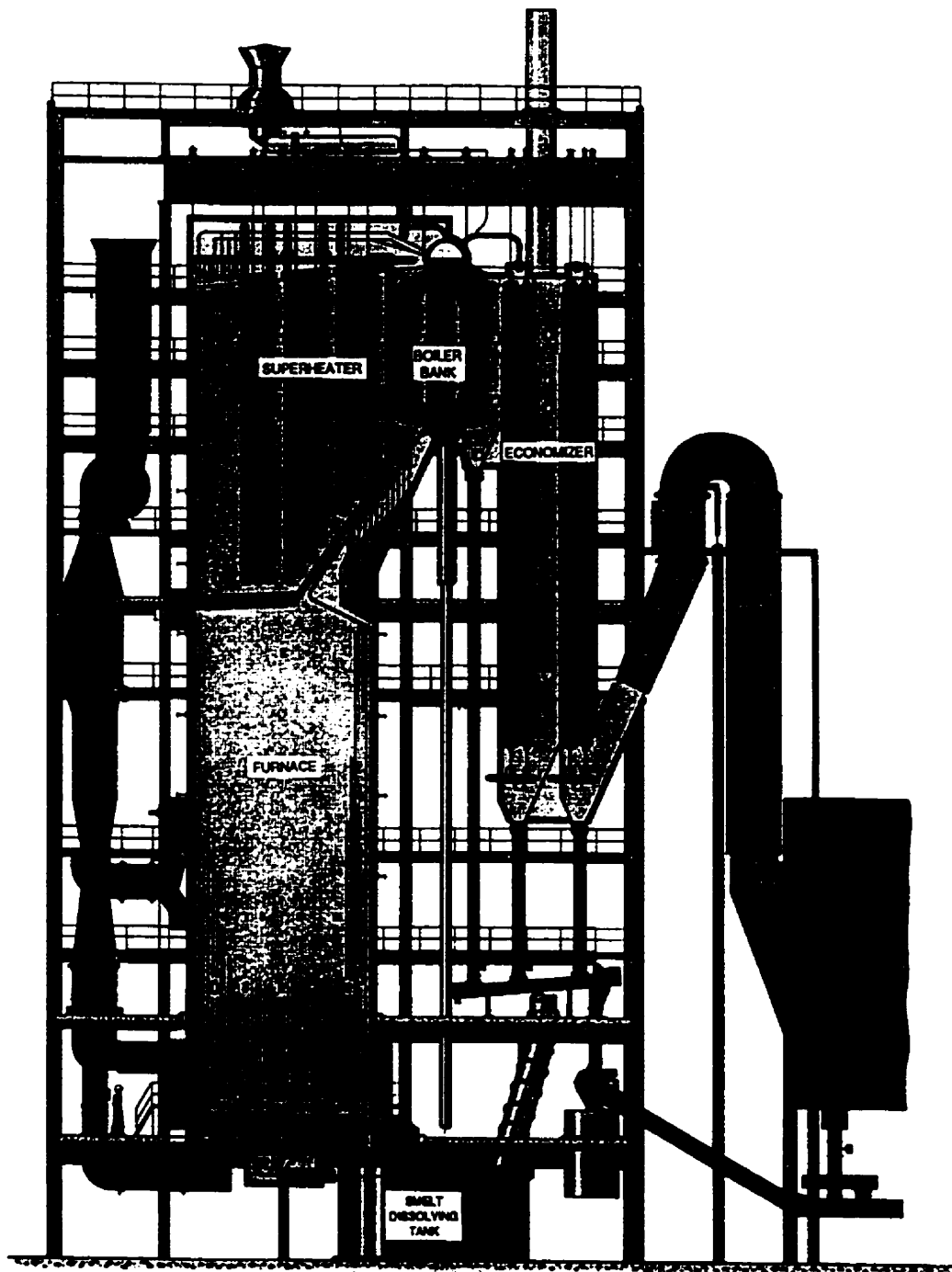


Figure 1. The schematic diagram of kraft recovery boiler.

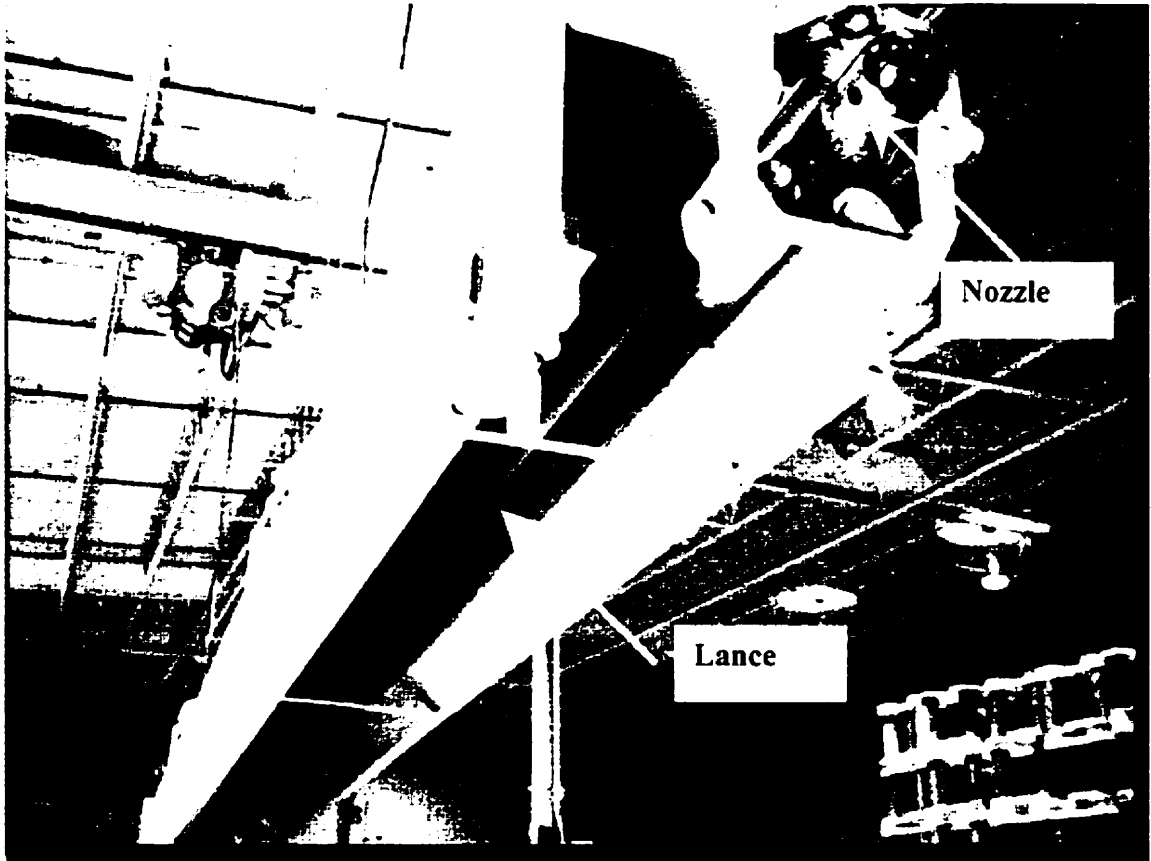


Figure 2. A sootblower in a machine shop.

Superheater Platens

Boiler Bank

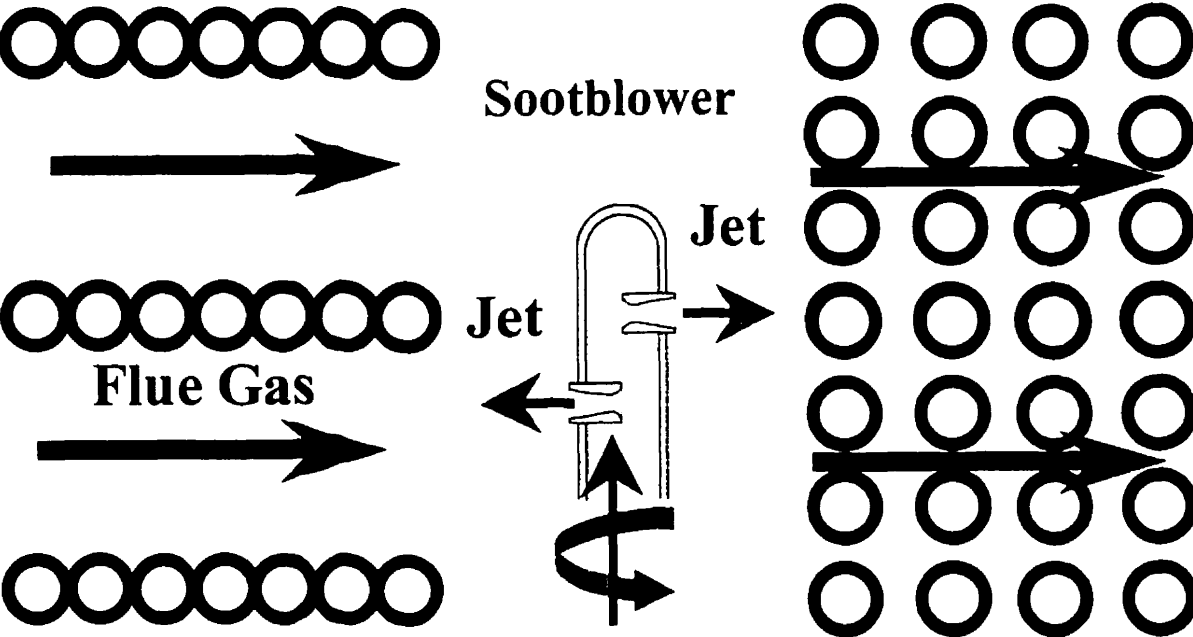


Figure 3. A sootblower in action at the inlet of a boiler bank.

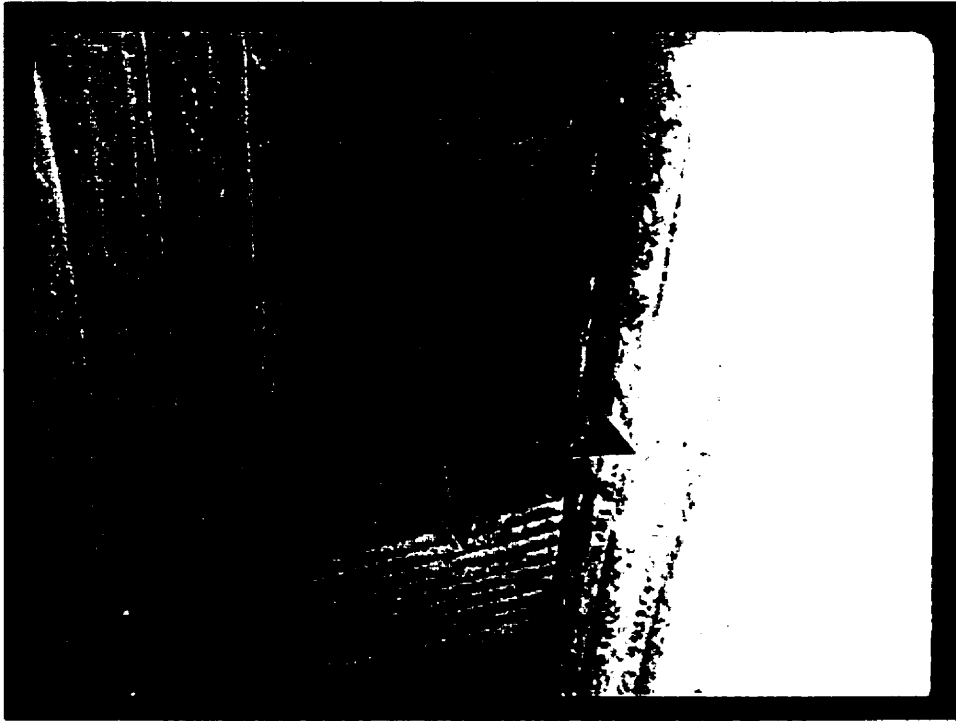


Figure 4. Condensed material deposited on screen tubes. Dark deposits are carryover deposits [2].



Figure 5. Plugging at the entrance of the boiler bank.

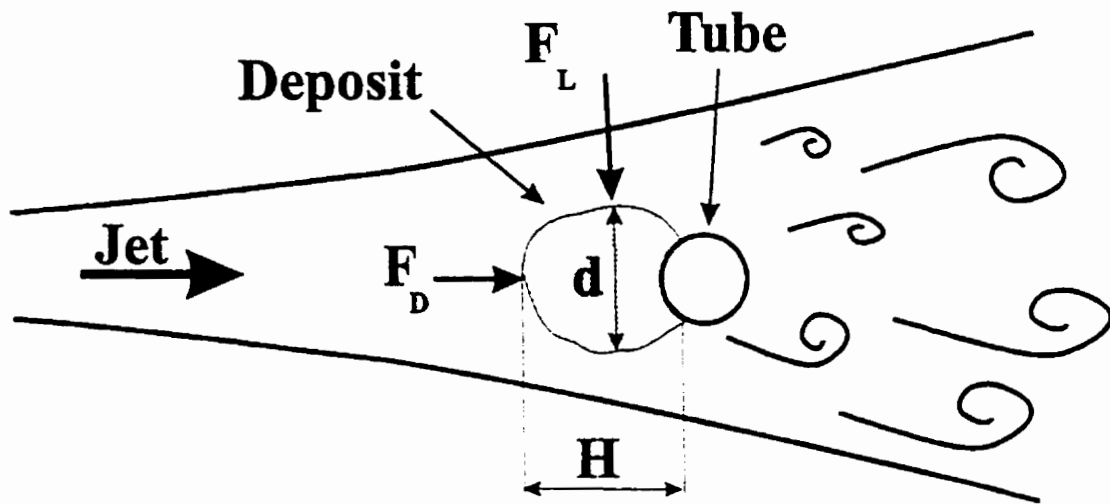


Figure 6. Characteristic dimensions of a deposit and aerodynamic forces.

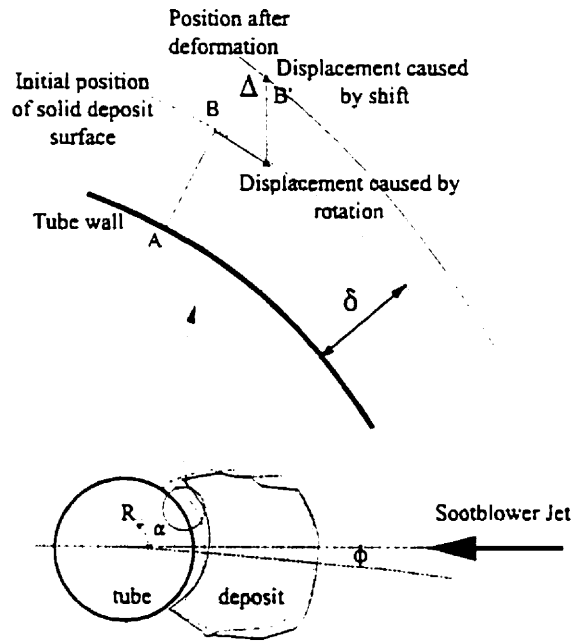


Figure 7. Deformation of a deposit in debonding. [31].

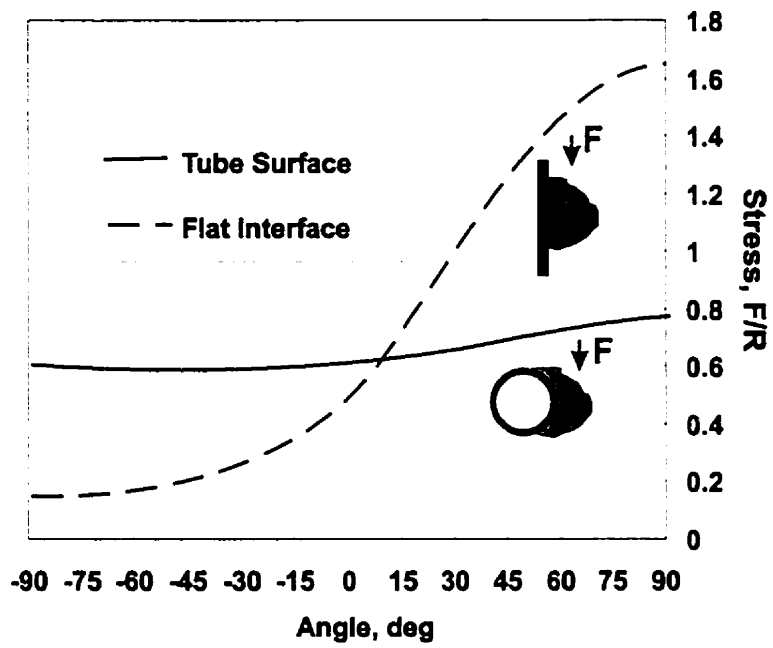


Figure 8. Distribution of tensile stresses at the flat and cylindrical interface [31]. For the cylindrical interface the unit-length interface area is equal to $2 \alpha R$. For every α , an identical unit-length interface area for the flat interface is chosen for comparison.

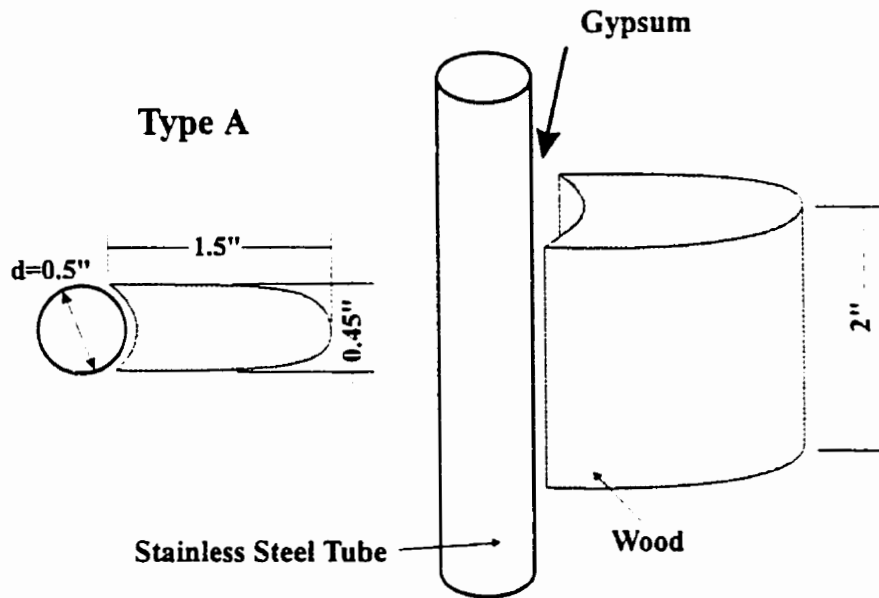


Figure 9. Type A model deposit.

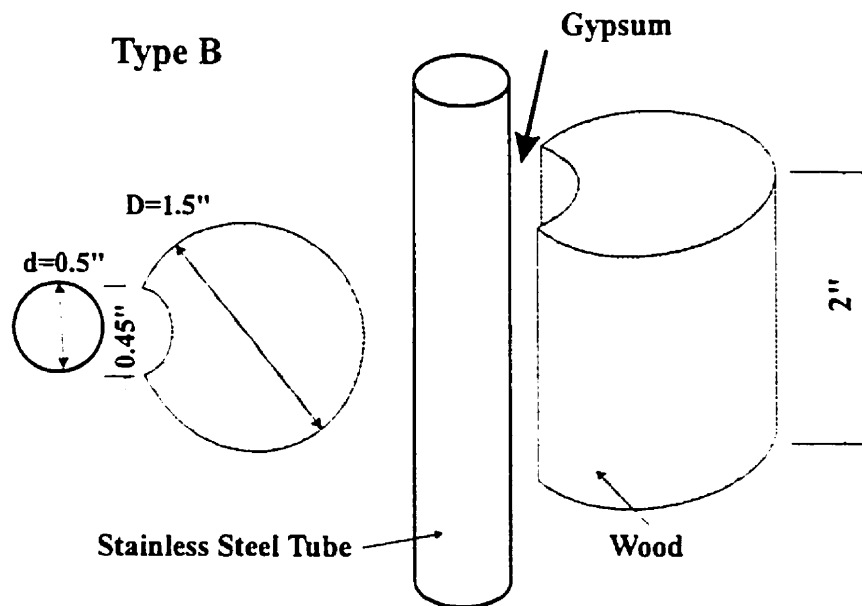


Figure 10. Type B model deposit.

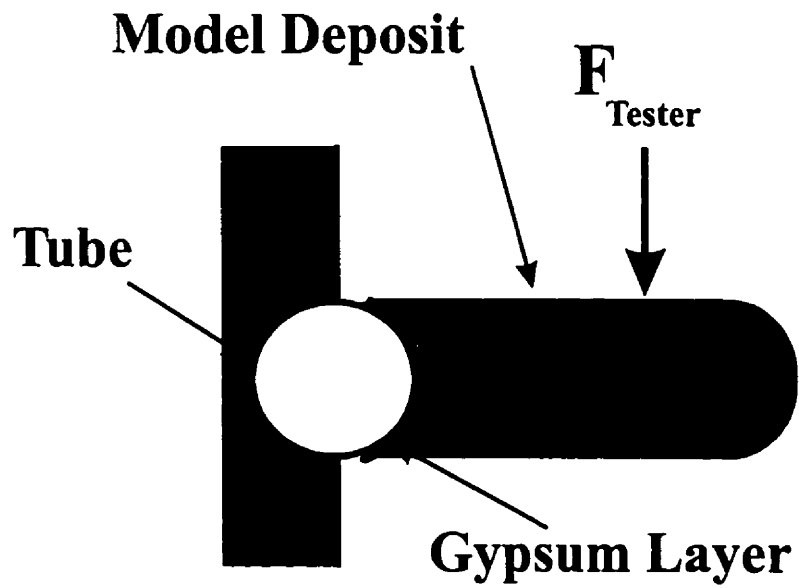


Figure 11. The schematic diagram of how the adhesion strength of gypsum was measured using the strength tester.

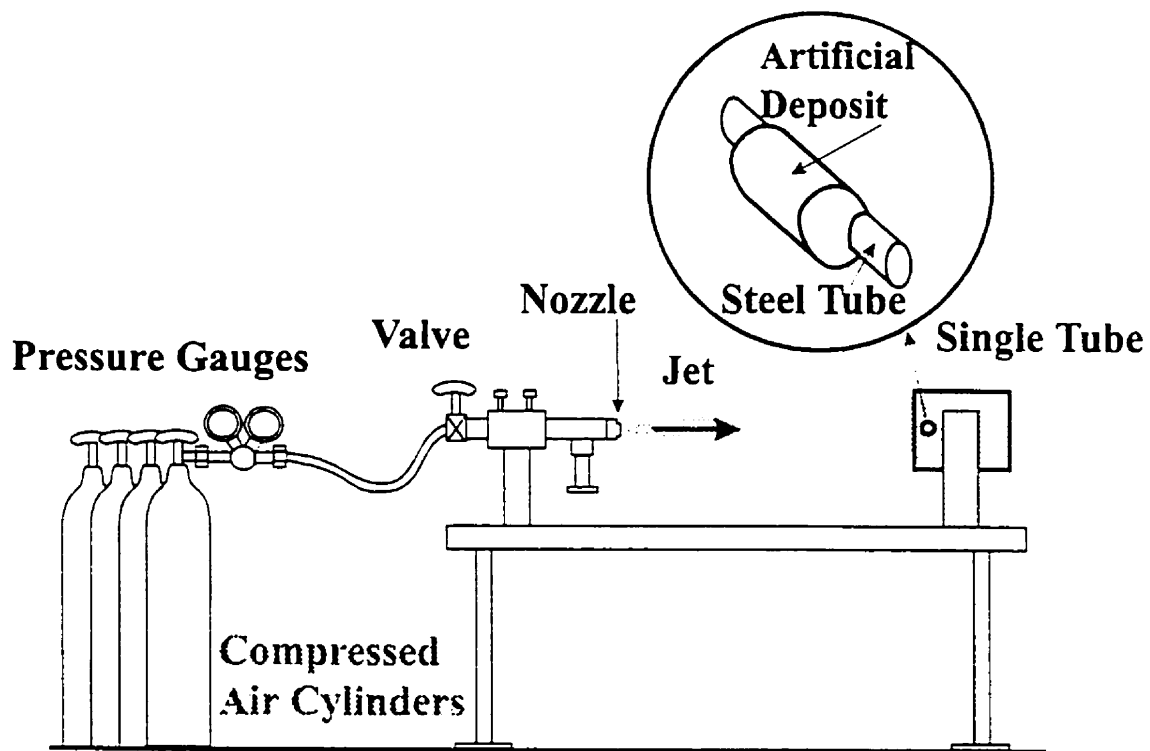
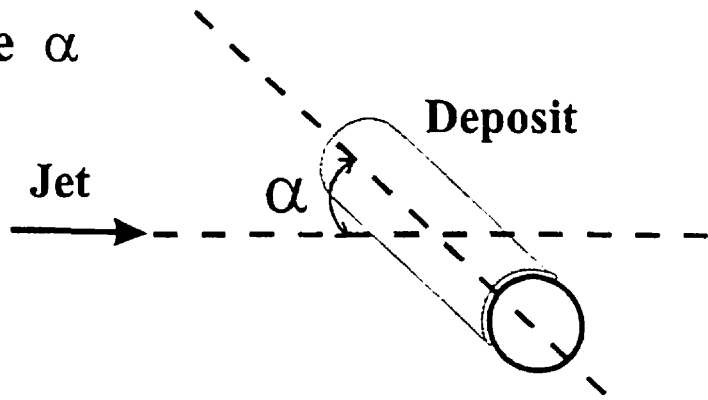
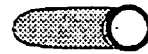
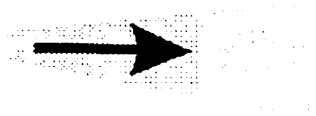


Figure 12. Deposit removal (blow-off) experiment apparatus.

Jet Attack Angle α

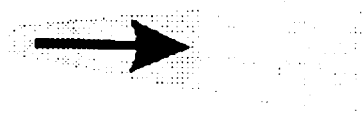


Jet



a) $\alpha = 0^{\circ}$

Jet



b) $\alpha = 90^{\circ}$

Figure 13. Definition of the jet attack angle.

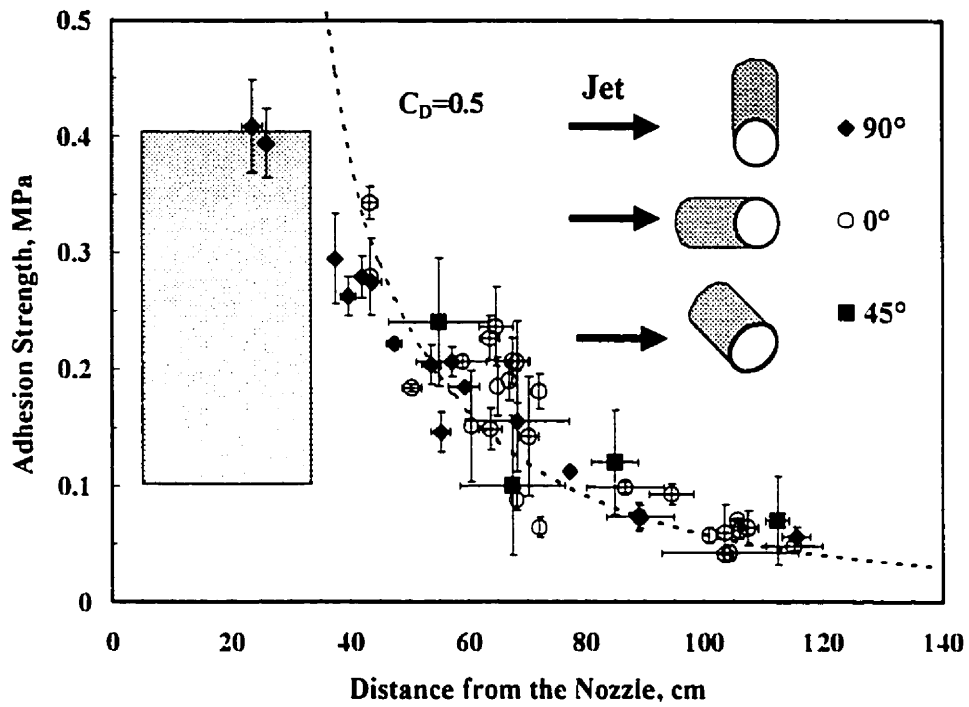


Figure 14. Blow-off experimental data for type A deposit. The gray-shaded box represents the region that 20 samples with adhesion strength between 0.1 to 0.4 MPa were placed from 35 cm from the nozzle and moved to 7.5 cm from the nozzle, but were not debonded from the tube by the jet (0° attack angle experiments).

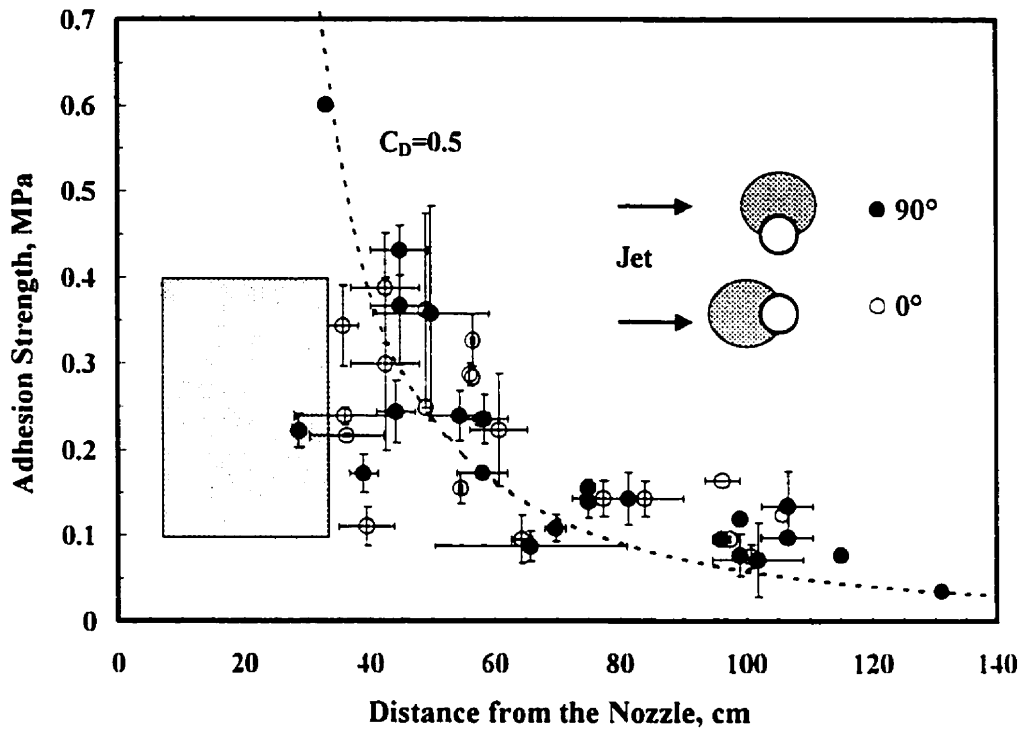


Figure 15. Blow-off experimental data for type B deposit. The gray-shaded box represents the region where 12 samples with adhesion strength between 0.1 to 0.4 MPa were placed from 35 cm from the nozzle and moved to 7.5 cm from the nozzle, but were not debonded from the tube by the jet (0° attack angle experiments).

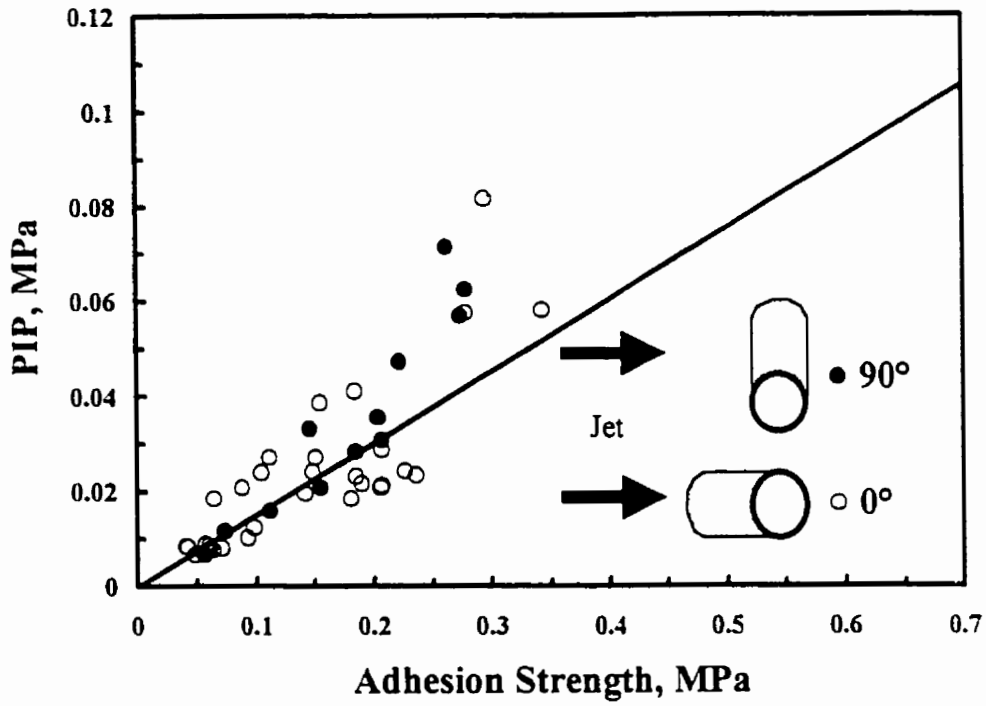


Figure 16. PIP required to debond Type A deposit as a function of the adhesion strength.

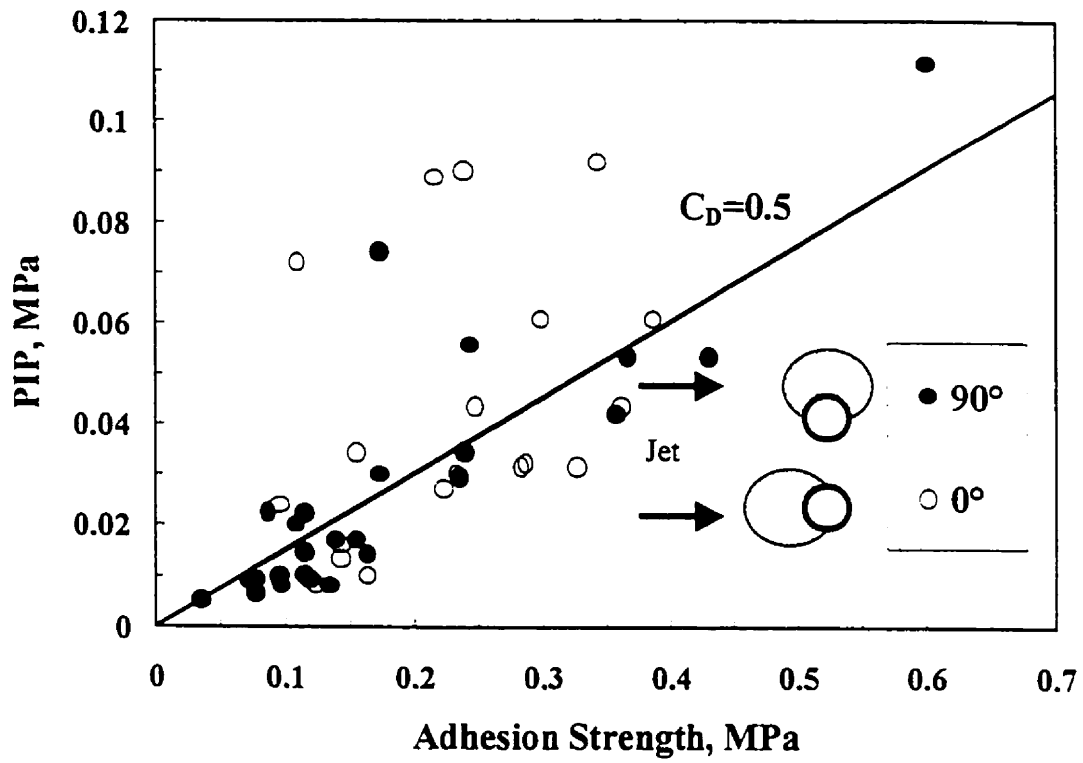


Figure 17. PIP required to debond Type B deposit as a function of the adhesion strength.

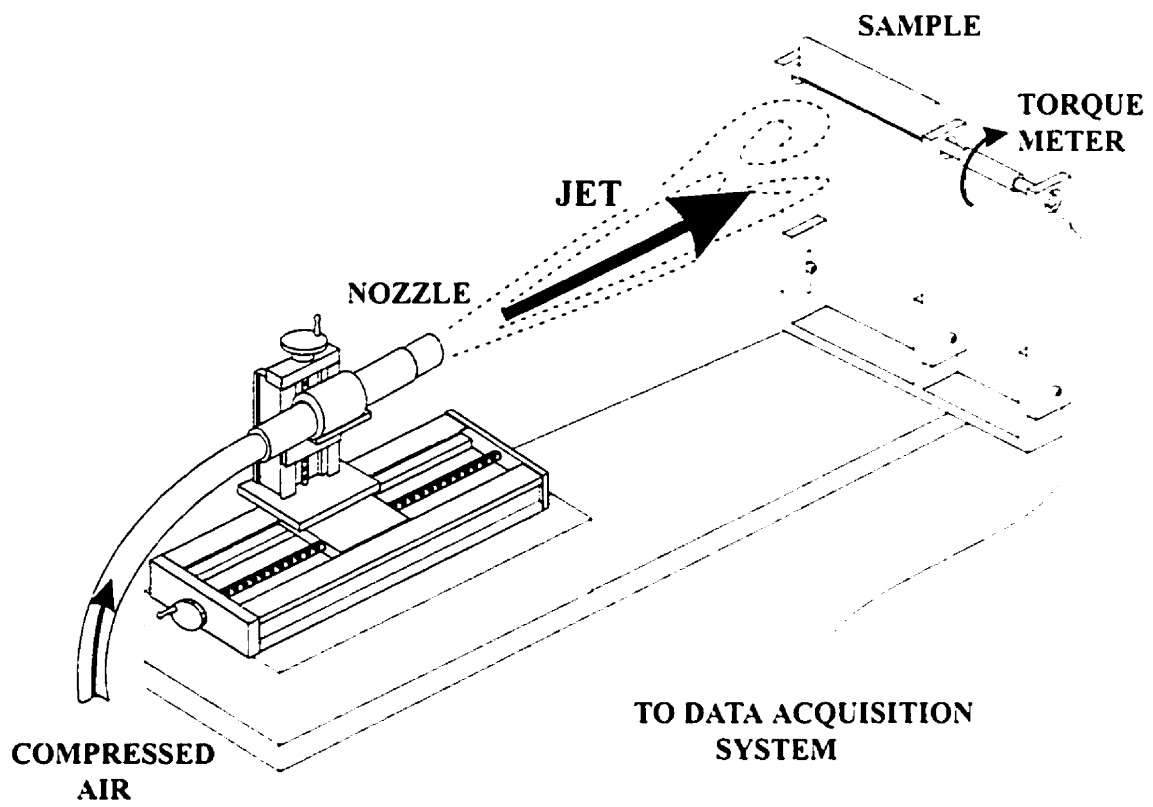
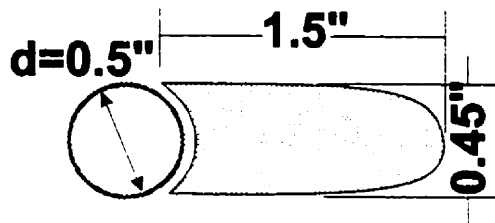
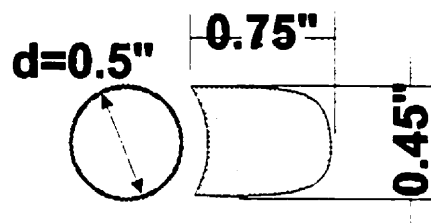


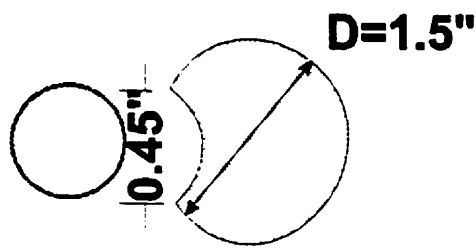
Figure 18. Torque Meter Experimental Apparatus for the measurements of the mean drag force.



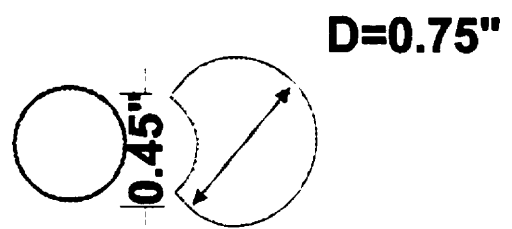
Type A



Type C

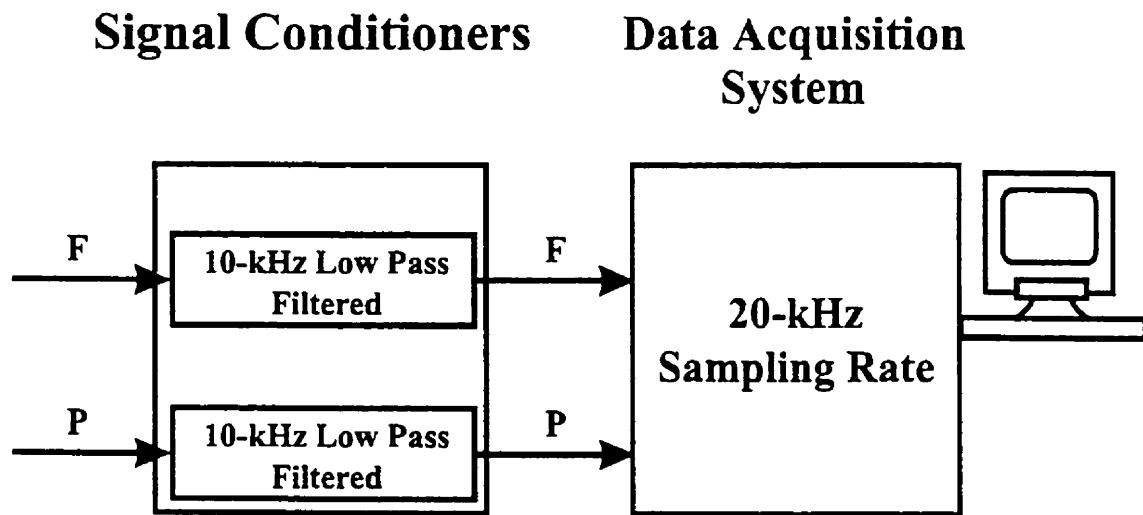


Type B



Type D

Figure 19. Model deposits.



F: Torque / Force Signal

P: Up-Stream Pressure Signal

Figure 20. Signal conditioning and data collection procedure.

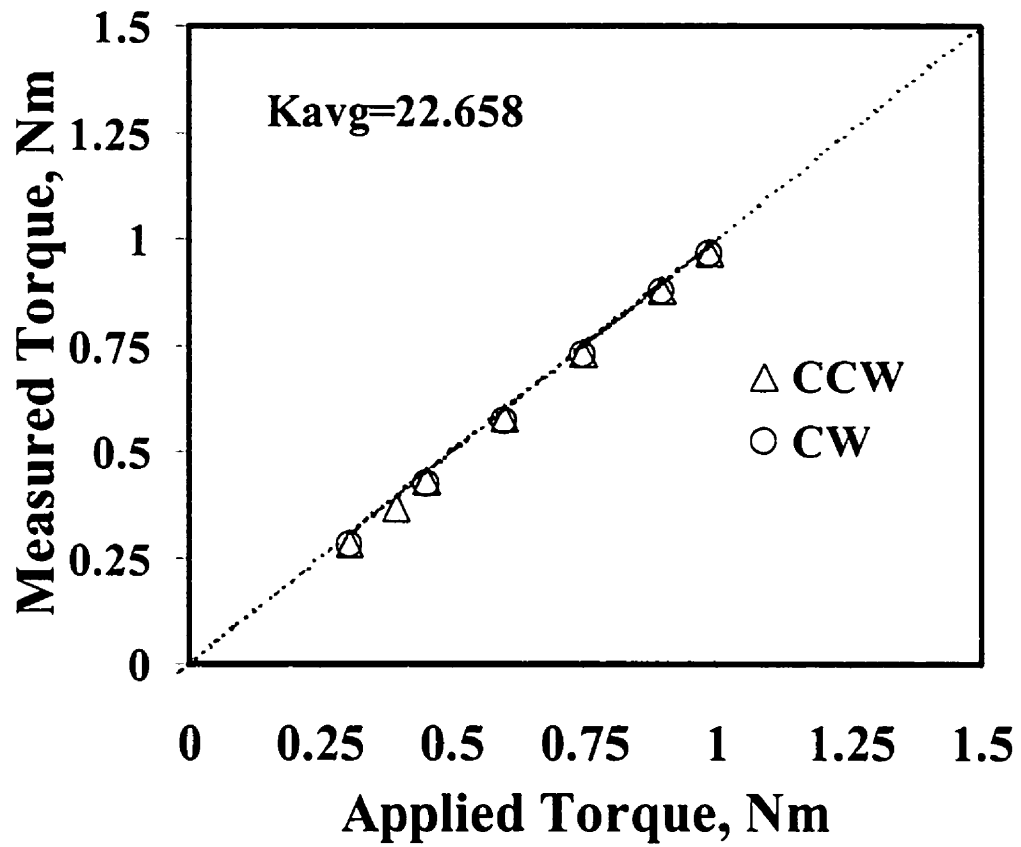


Figure 21. The calibration curve for the torque meter: (CW: clock wise, CCW: counter clock wise, Torque = (Output voltage/ Excitation voltage)*Kavg.)

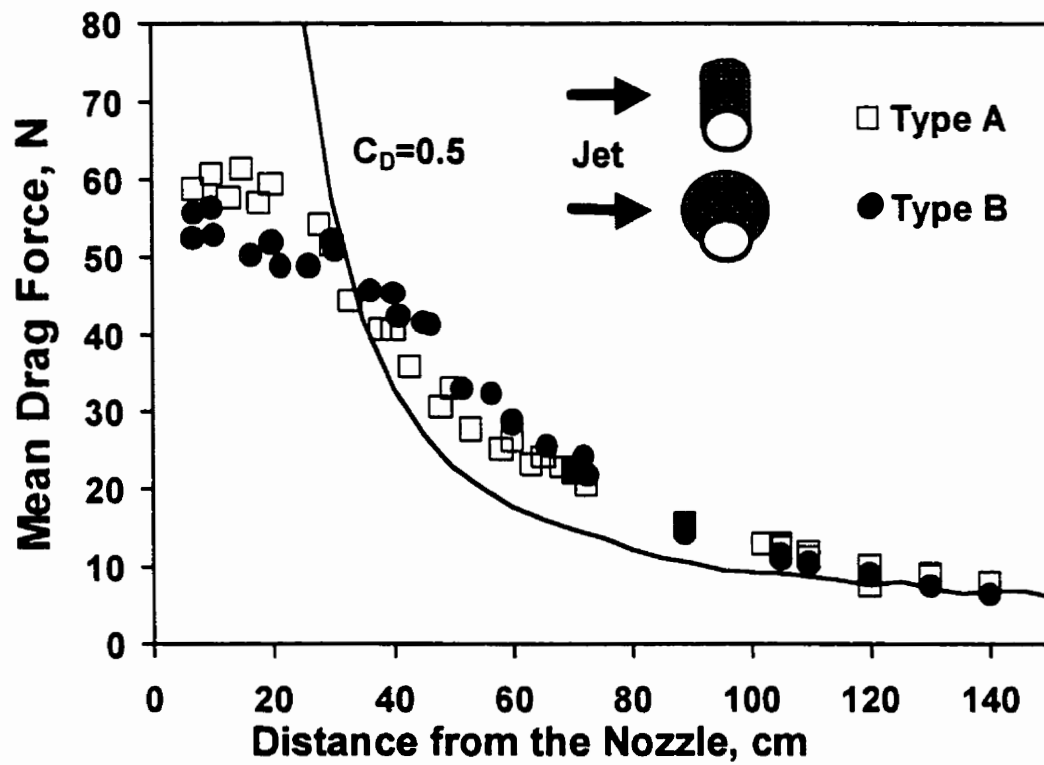


Figure 22. Drag force profiles for 1.5" deposits.

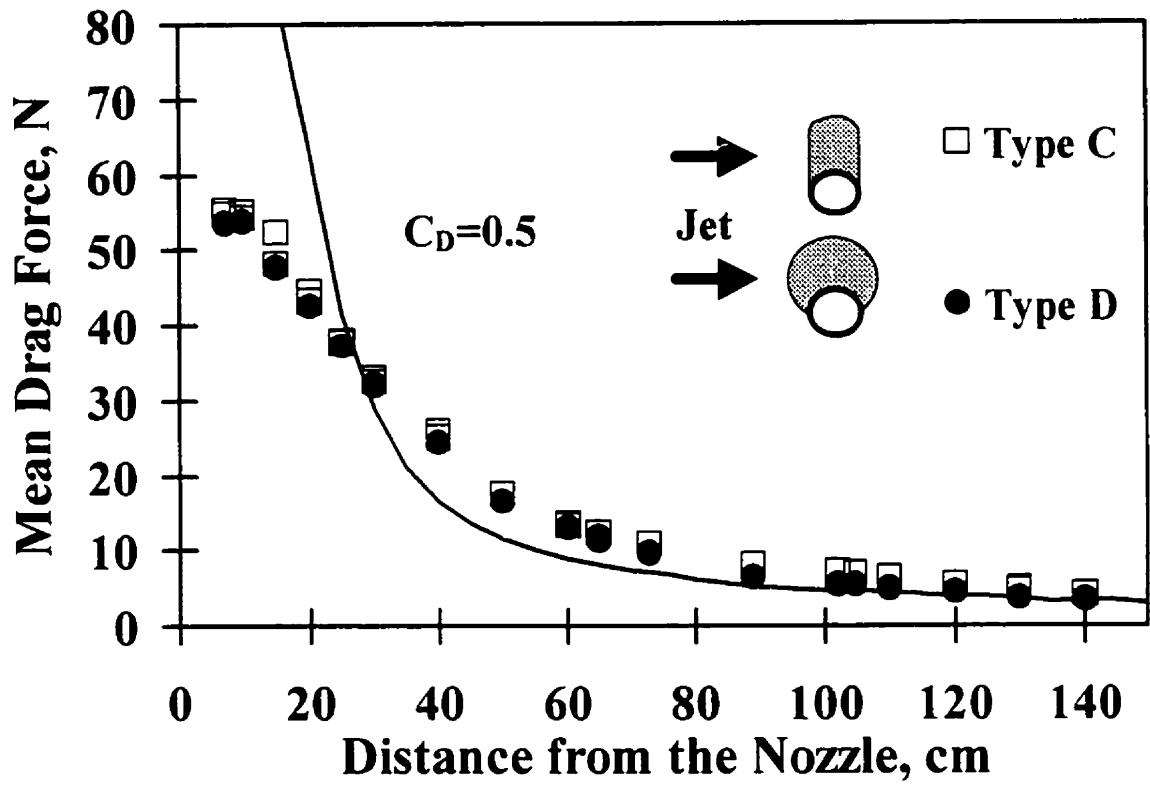


Figure 23. Drag force profile for 0.75" deposits.

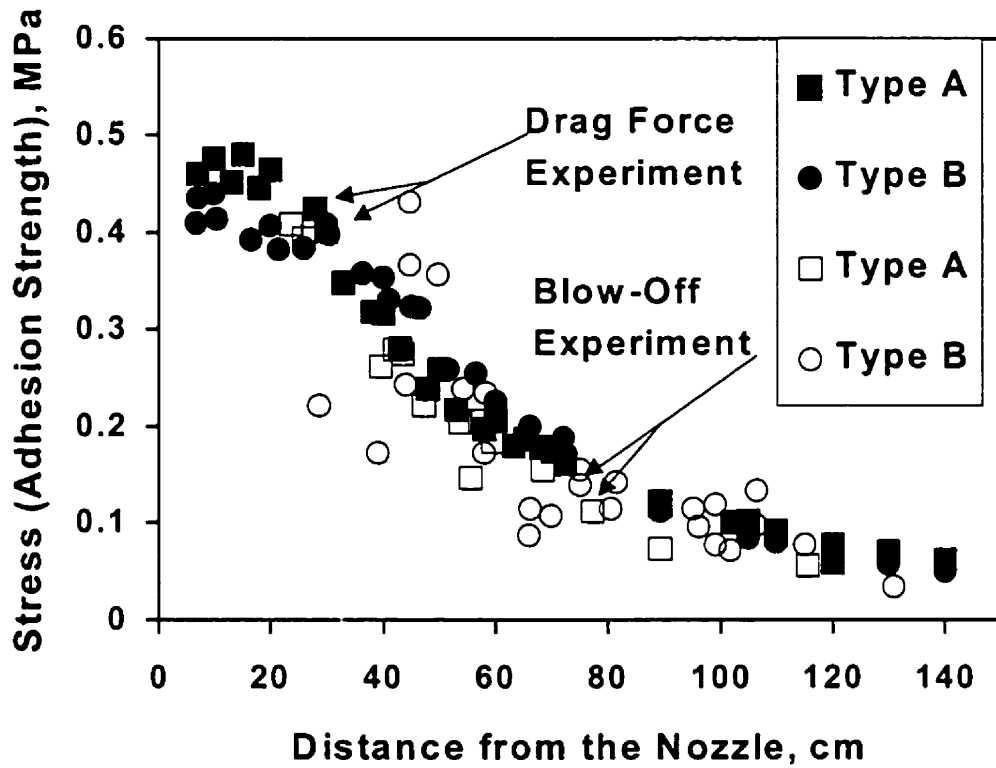


Figure 24. Comparison between the calculated maximum stress generated at the deposit-tube interface based on the drag force experiment, with the previously obtained results from blow-off experiment.

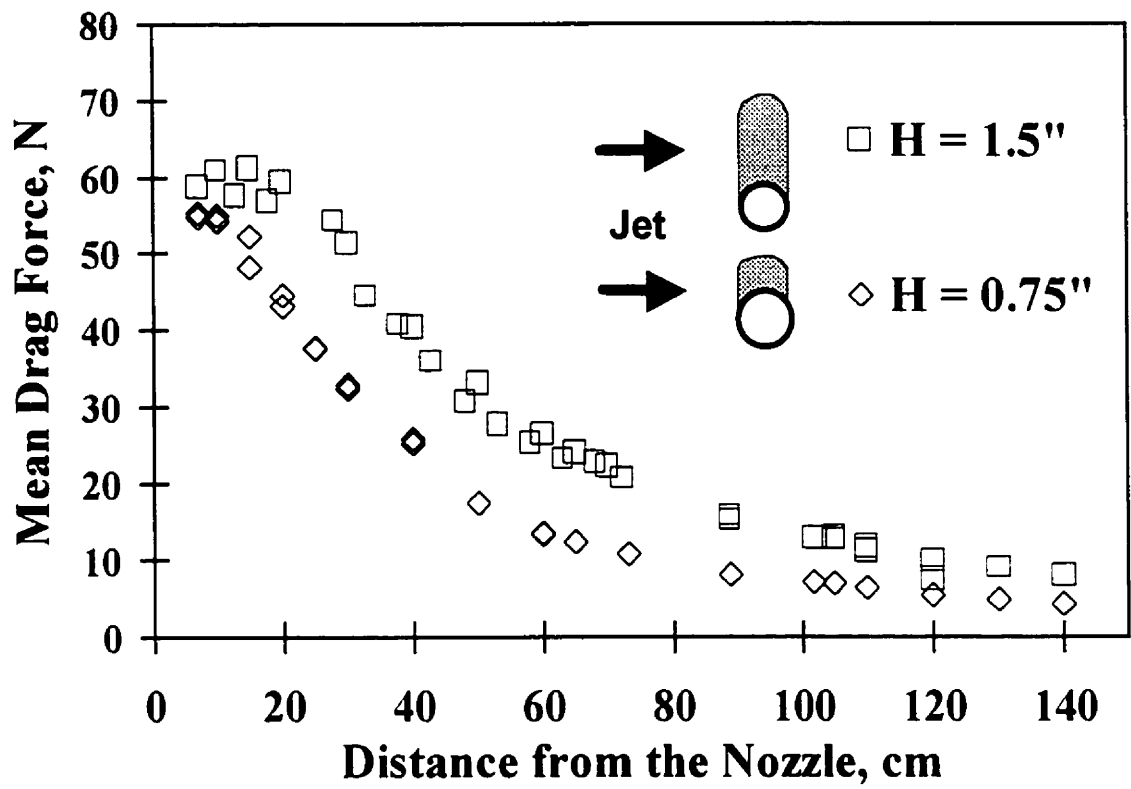


Figure 25. Comparison between drag forces for elongated deposits with 1.5" and 0.75" diameters.

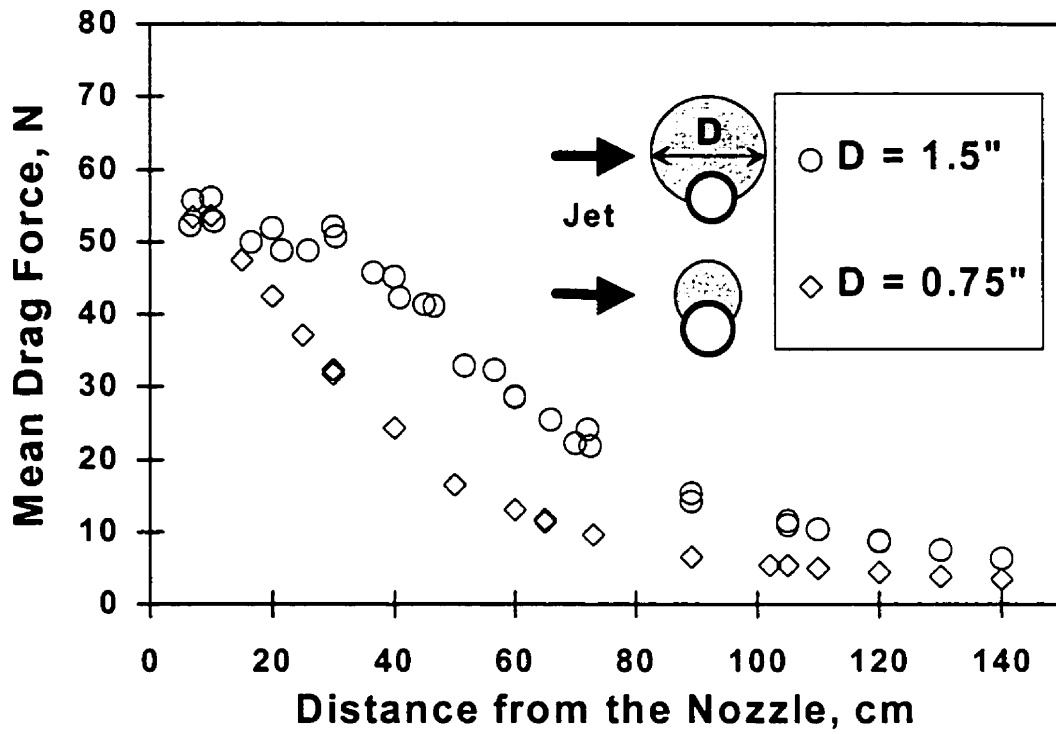


Figure 26. Comparison between drag forces for cylindrical deposits with 1.5" and 0.75" diameters.

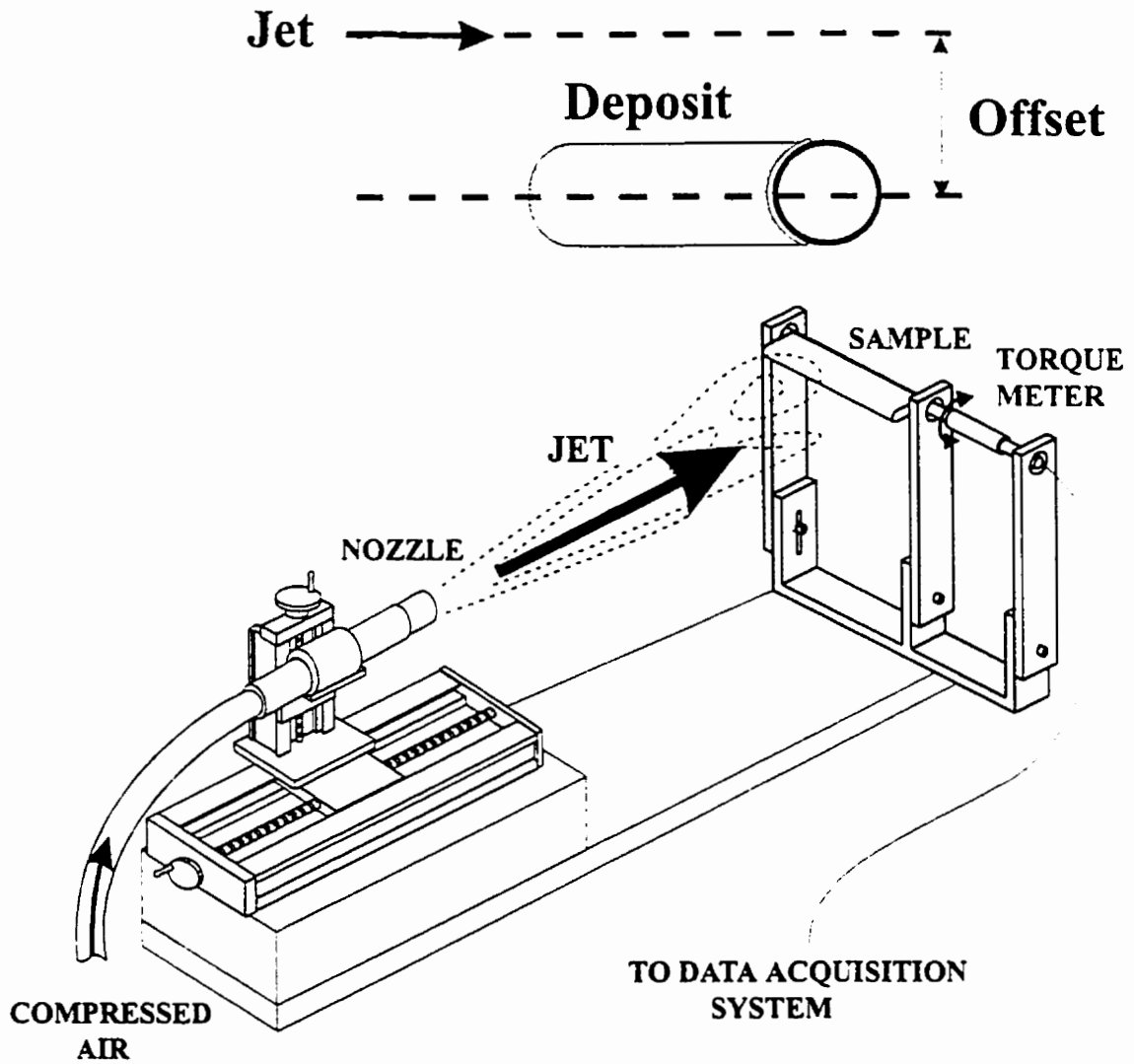


Figure 27. Torque meter experimental apparatus for the measurements of the lift force.

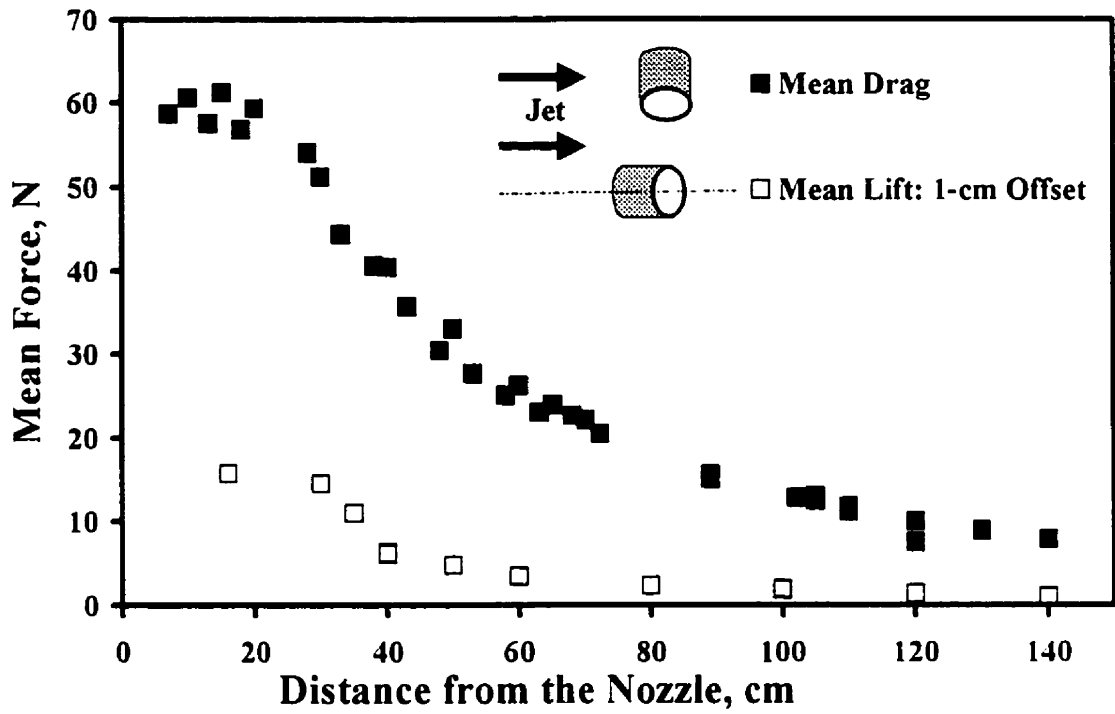


Figure 28. Comparison of mean drag force decay and mean lift force (1-cm offset) for type A deposit.

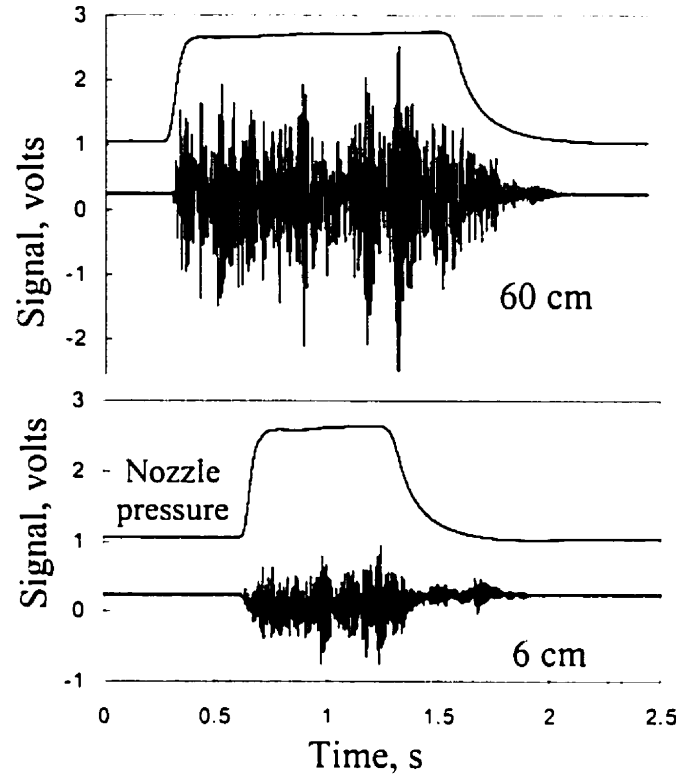


Figure 29. The torque meter signals for 0° attack angle measured at 6-cm and 60-cm from the nozzle, respectively.

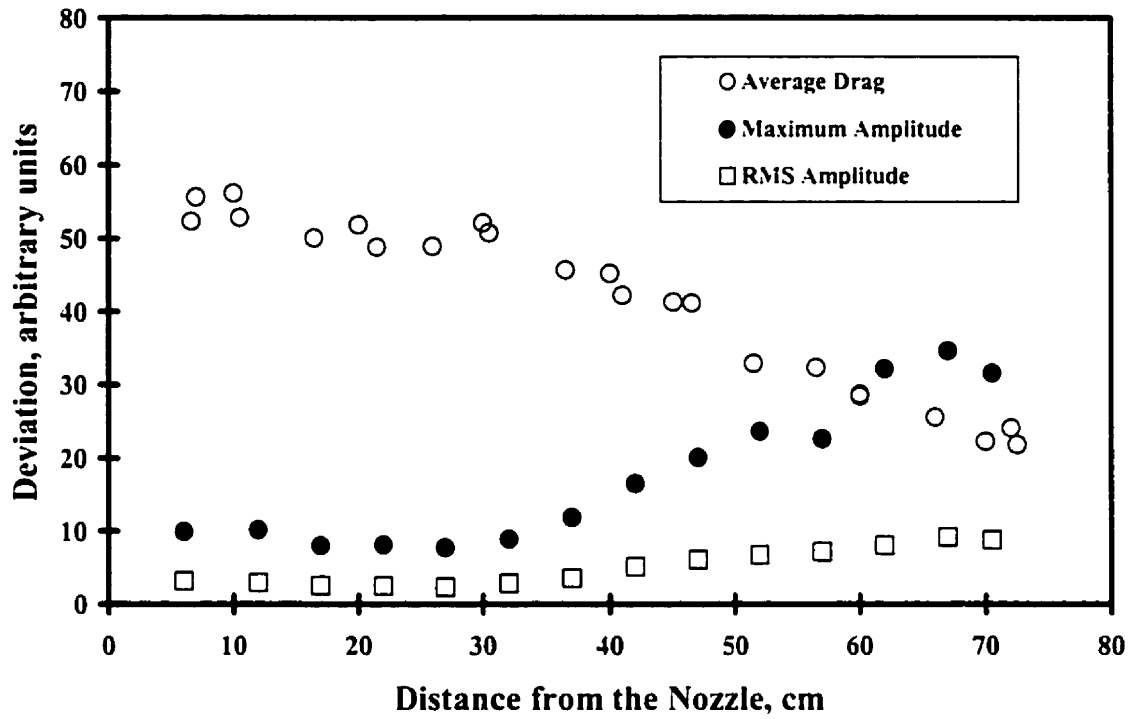


Figure 30. Comparison between the mean drag force and flow-induced vibrations (0° attack angle), measured by the torque meter.

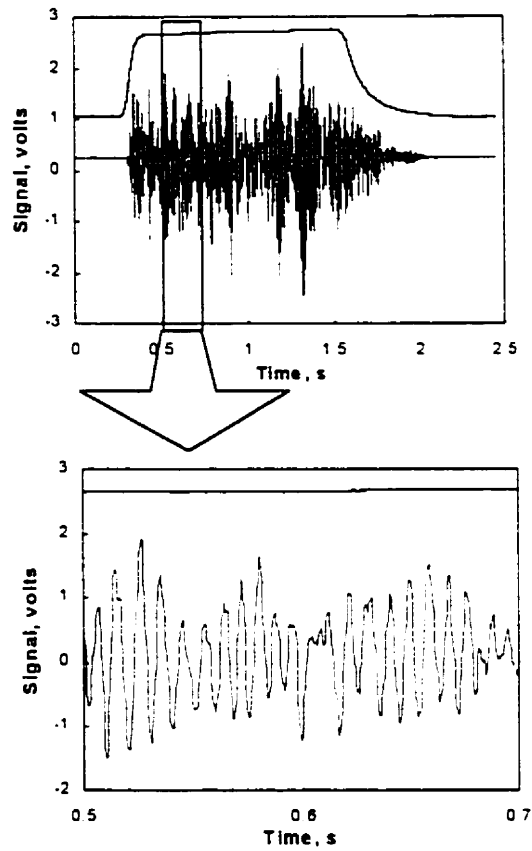


Figure 31. Torque meter signal for 0° attack angle measured at 60-cm from the nozzle.

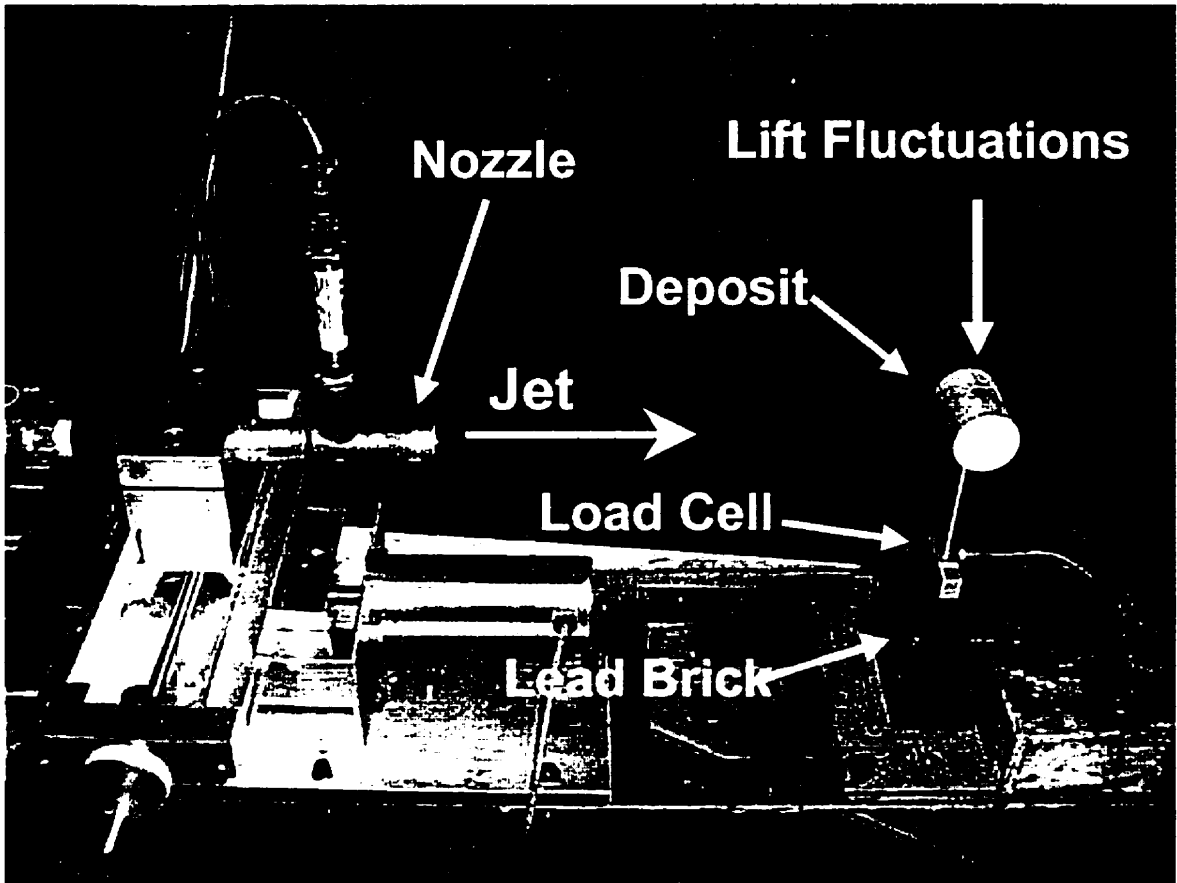


Figure 32. Load cell experimental apparatus: lift force measurement deposit orientation.

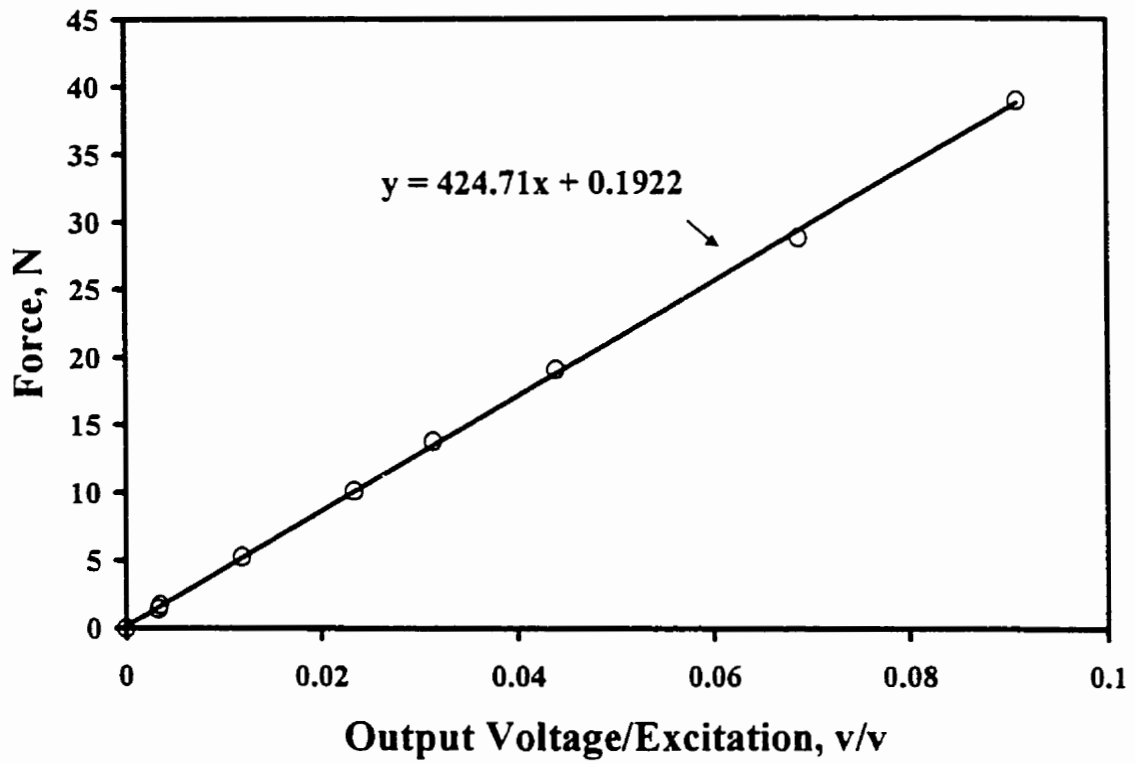


Figure 33. Load cell calibration curve.

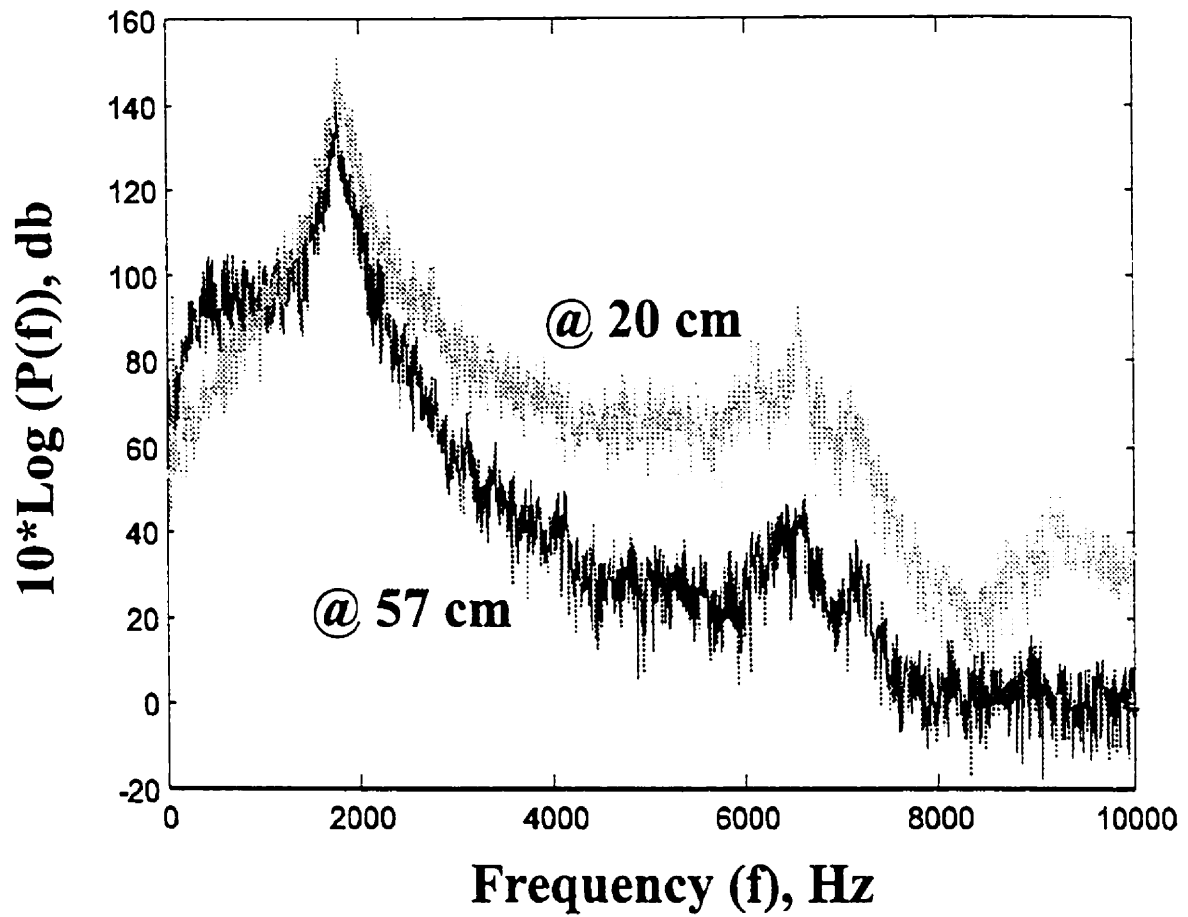


Figure 34. The power spectra of the load cell signals at 20-cm and 57-cm, respectively.

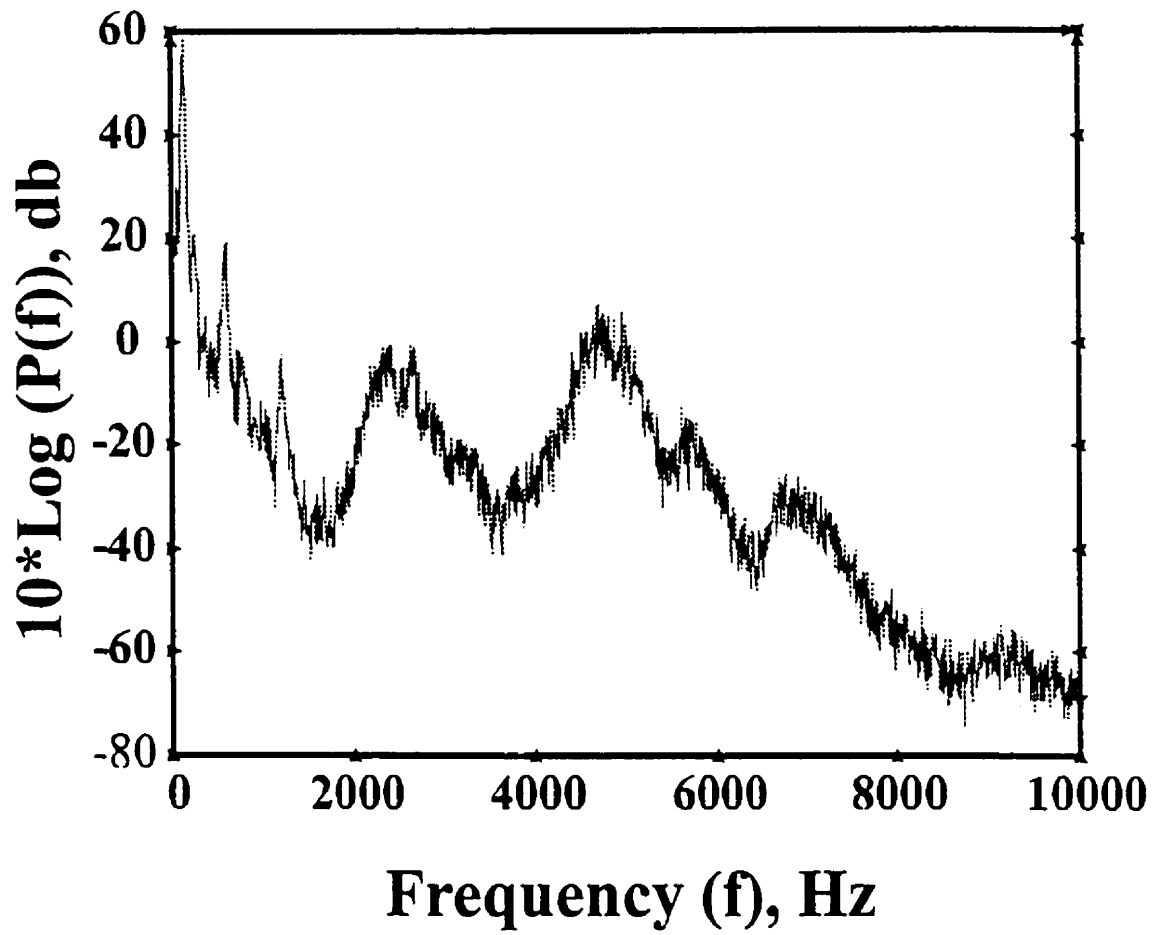


Figure 35. Typical power spectrum of the lift force measured by the torque meter.

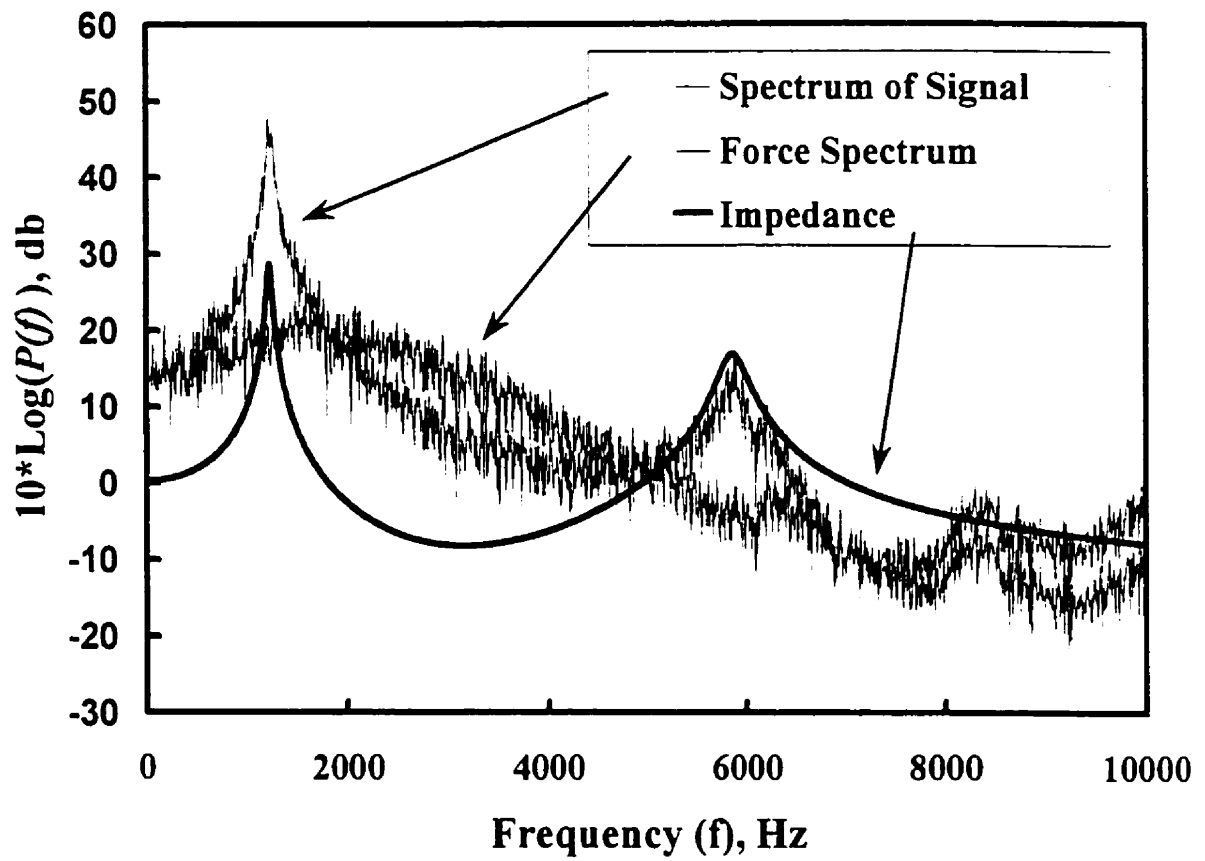


Figure 36. Power spectra of the raw signal and the lift force.

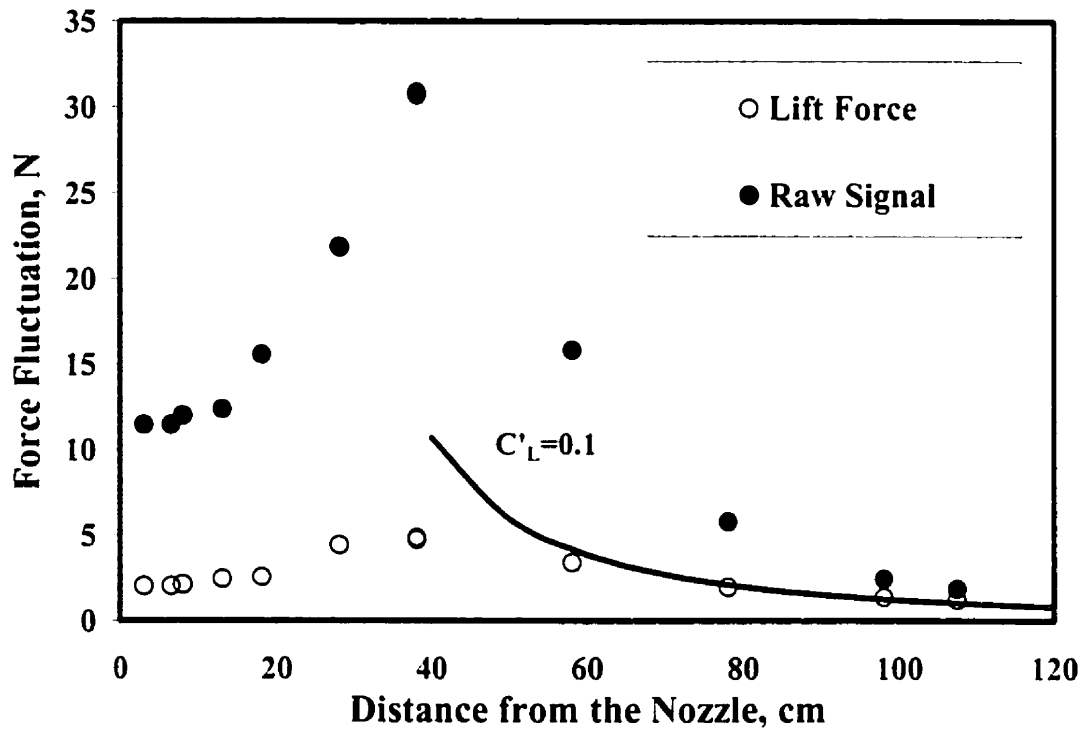


Figure 37. Comparison between the lift force fluctuations and the raw signal exerted on 3.8-cm cylindrical deposits (the effect of vibration is included).

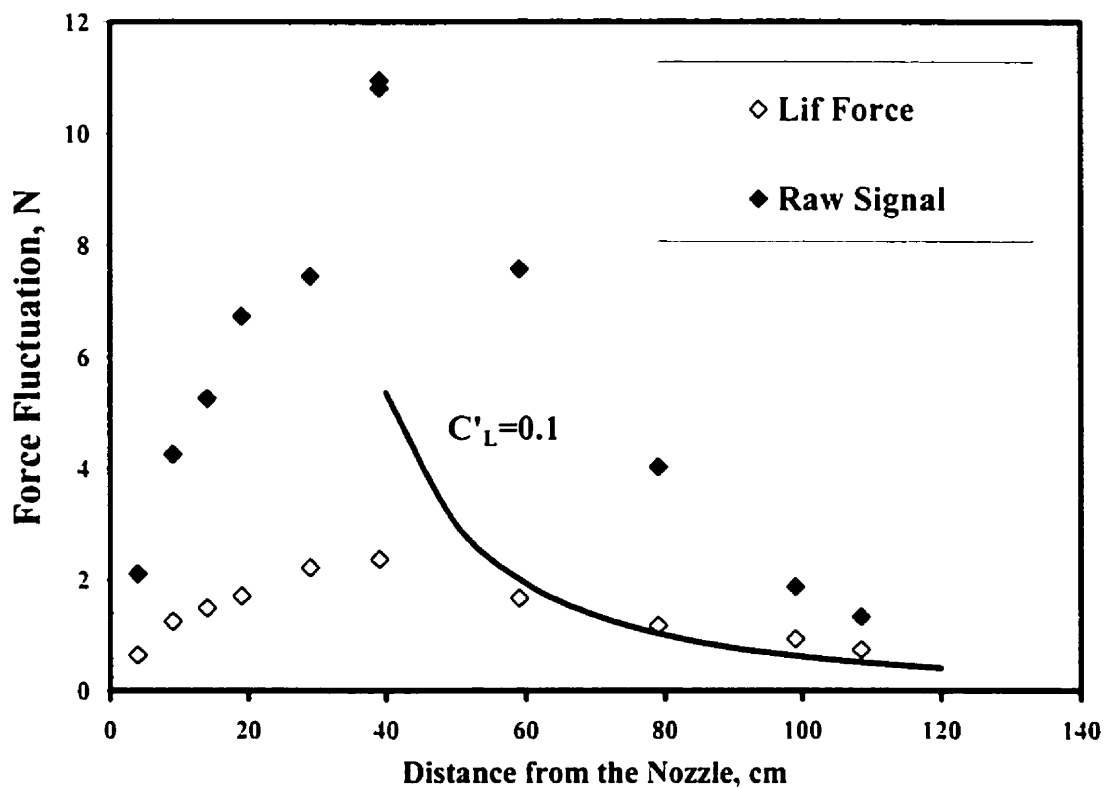


Figure 38. Comparison between the lift force fluctuations and the raw signal exerted on 1.9-cm cylindrical deposits (the effect of vibration is included).

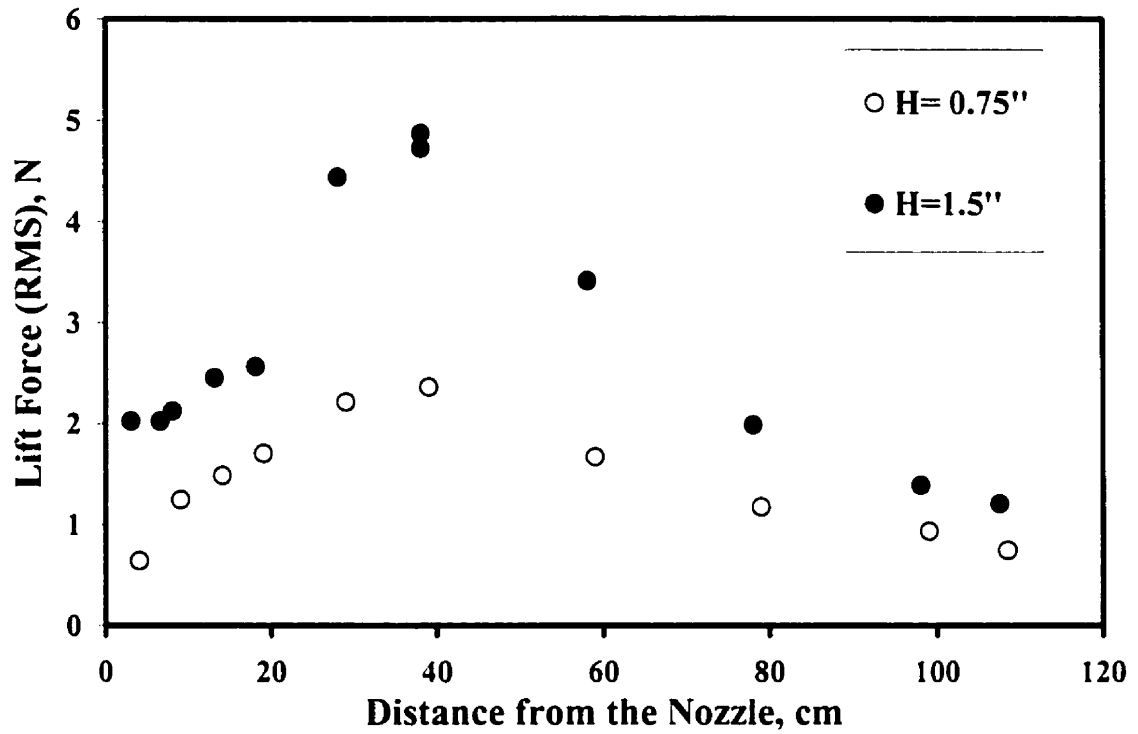


Figure 39. The profiles of the root mean square (r.m.s) of lift fluctuations forces exerted on 1.9-cm (0.75-inch) and 3.8-cm (1.5-inch) cylindrical deposits.

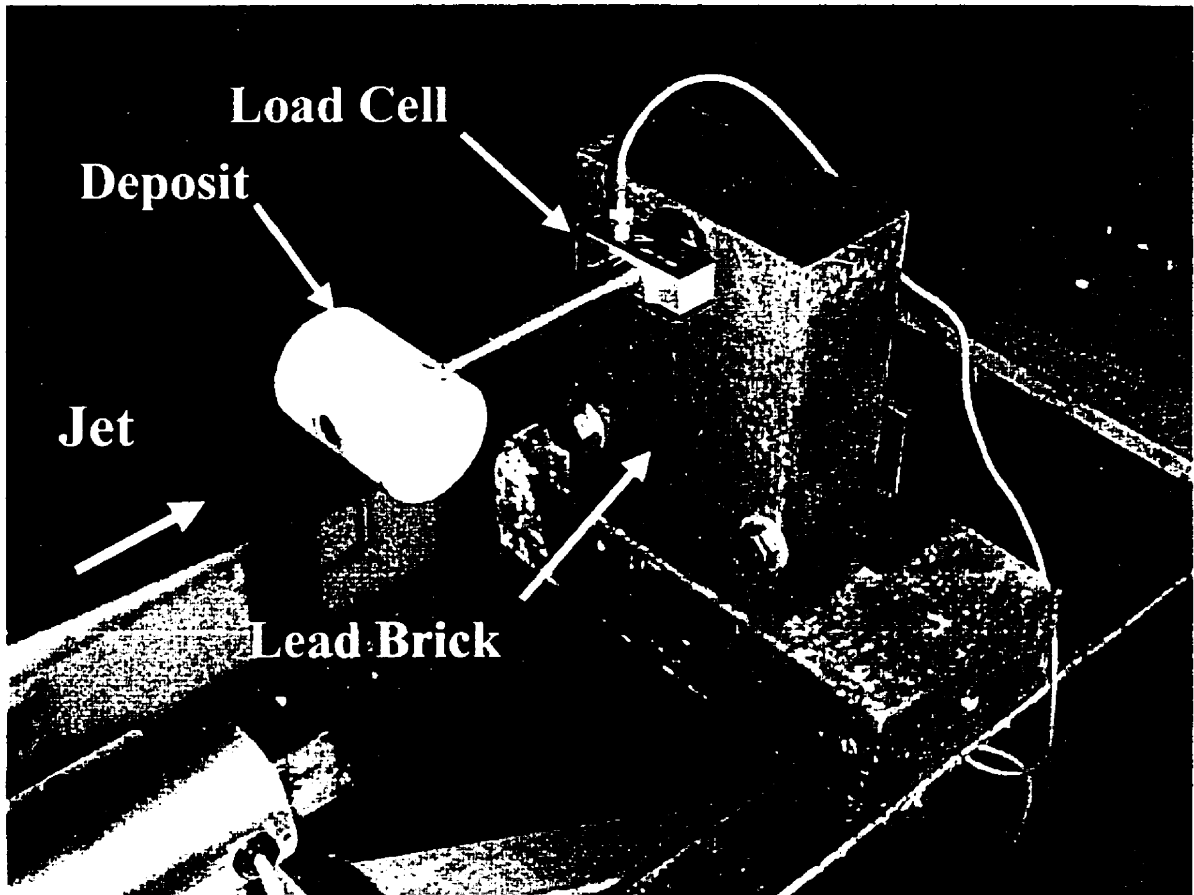


Figure 40. Load cell experimental apparatus: drag force measurement deposit orientation.

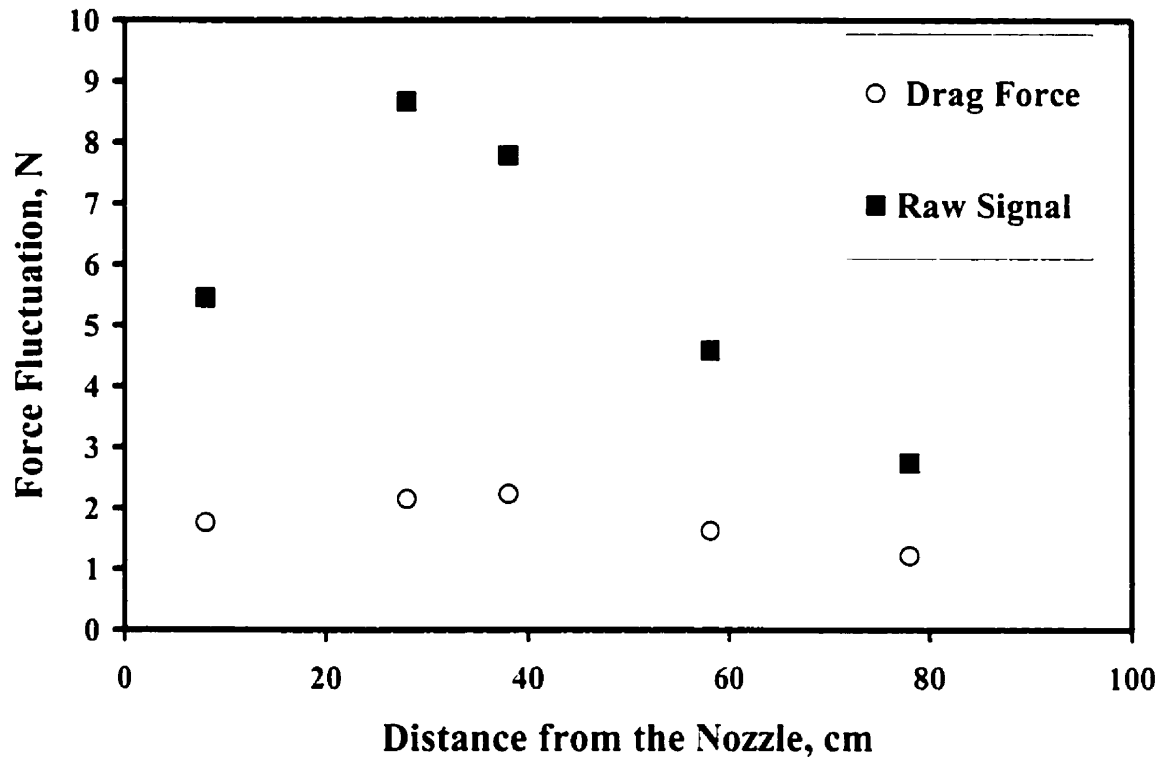


Figure 41. Comparison between the drag force fluctuations and the raw signal exerted on 3.8-cm cylindrical deposits (the effect of vibration is included).

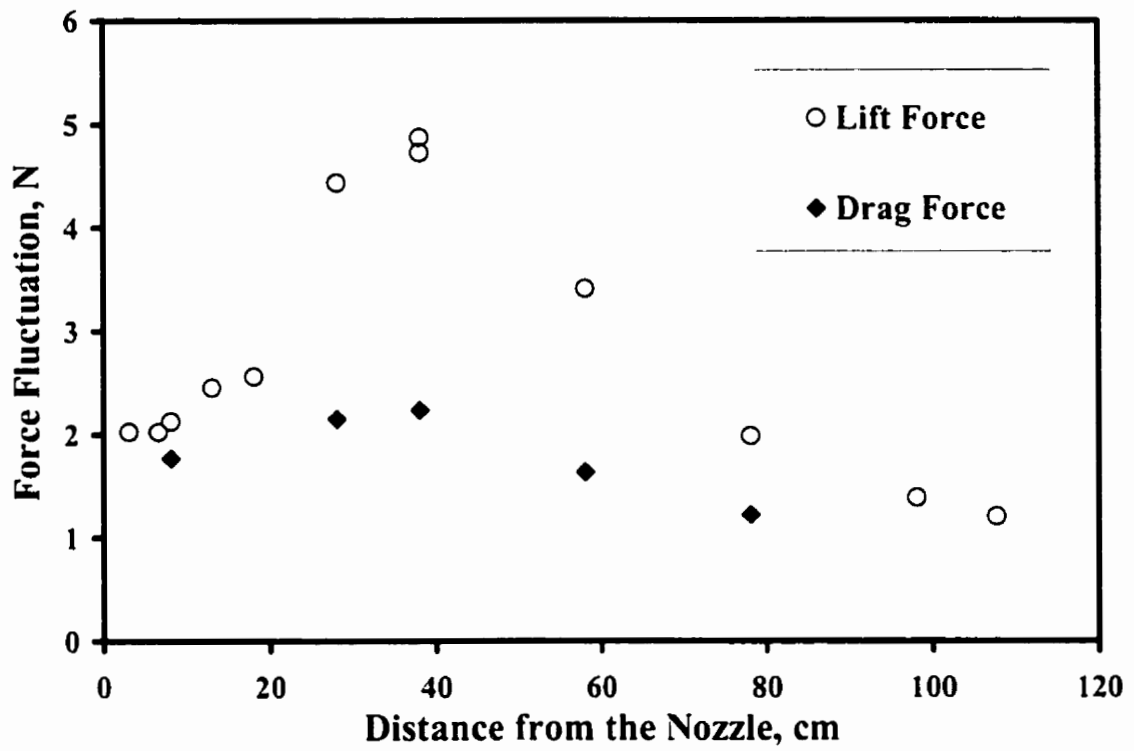


Figure 42. Comparison between the drag force fluctuations and the lift force fluctuations exerted on 3.8-cm (1.5-inch) cylindrical deposits.

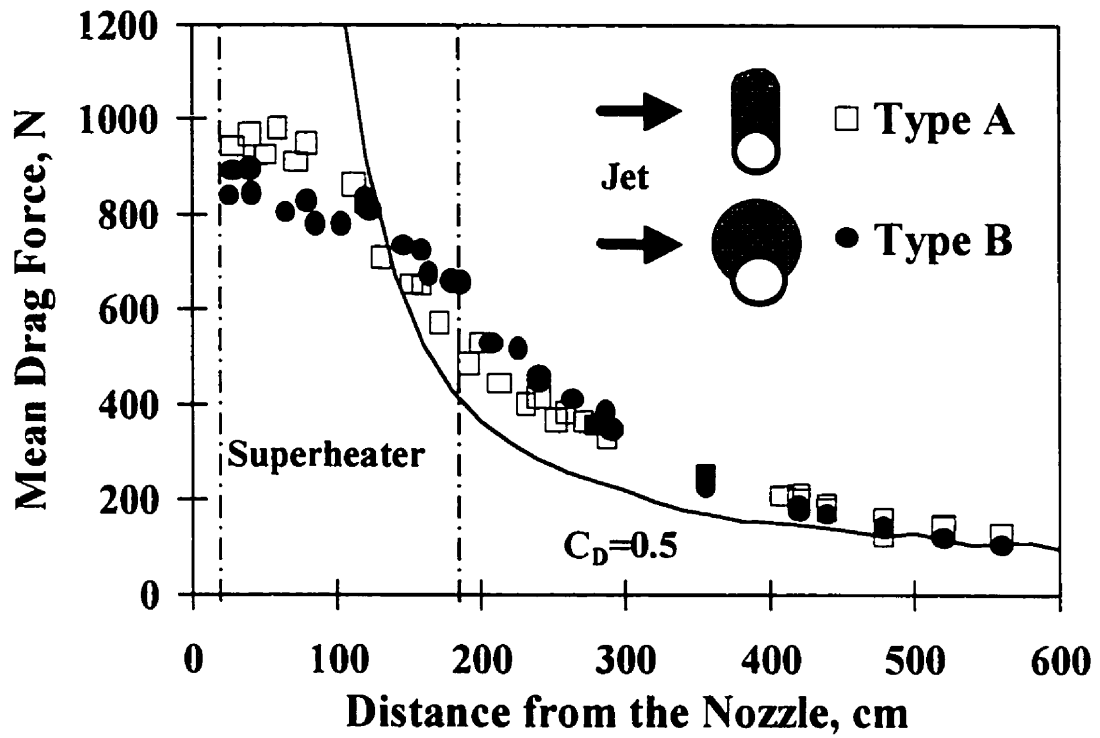


Figure 43. The estimated drag force decay exerted on 15.2-cm (6") deposits in a boiler.

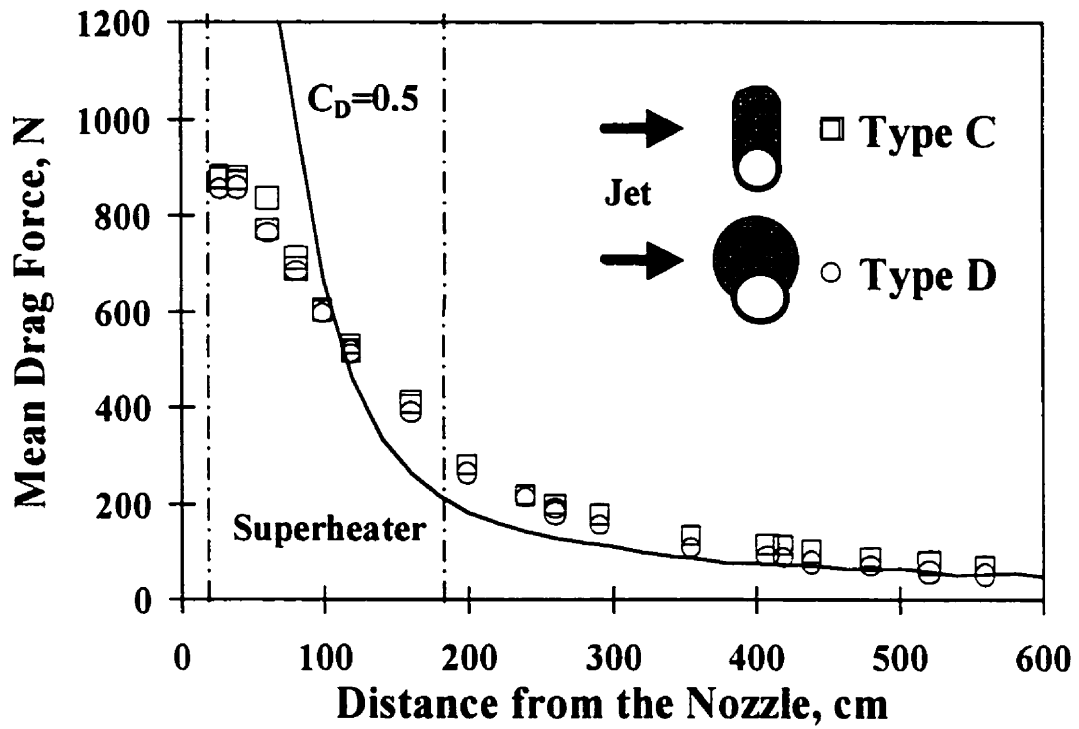


Figure 44. The estimated drag force decay exerted on 7.6-cm (3") deposits in a boiler.

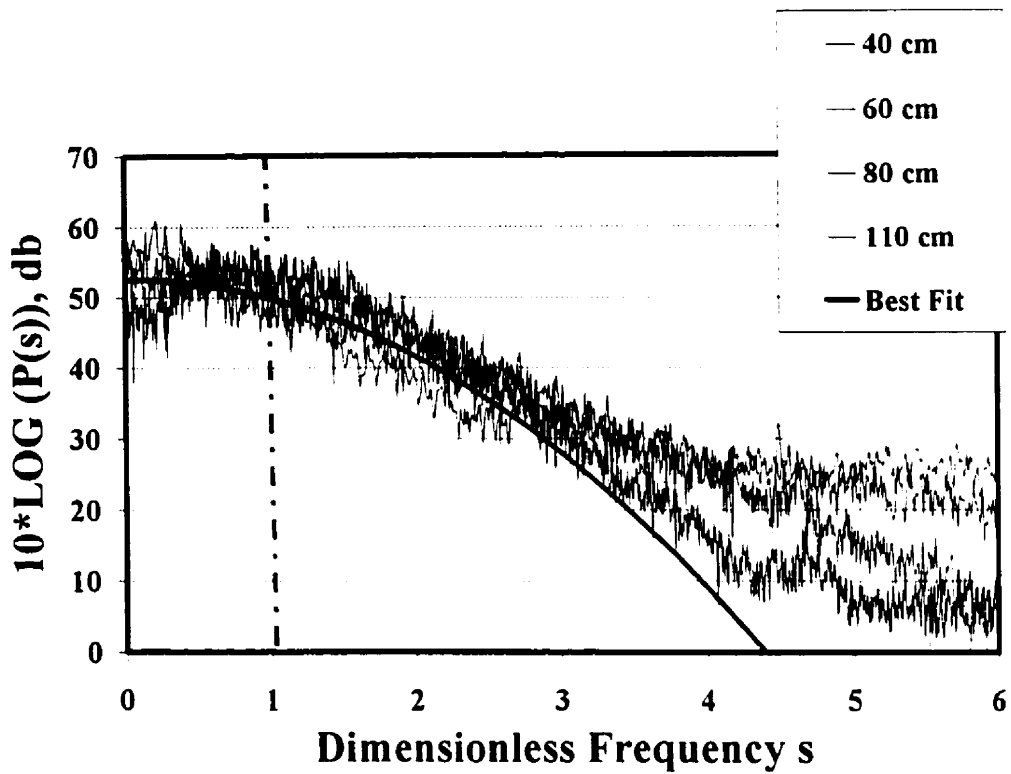


Figure 45. The dimensionless power spectra of the lift force exerted on 3.8-cm cylindrical deposit at different distances (best fit: $p(s) = 177828 * \exp(-s^2 (1.26^2))$).

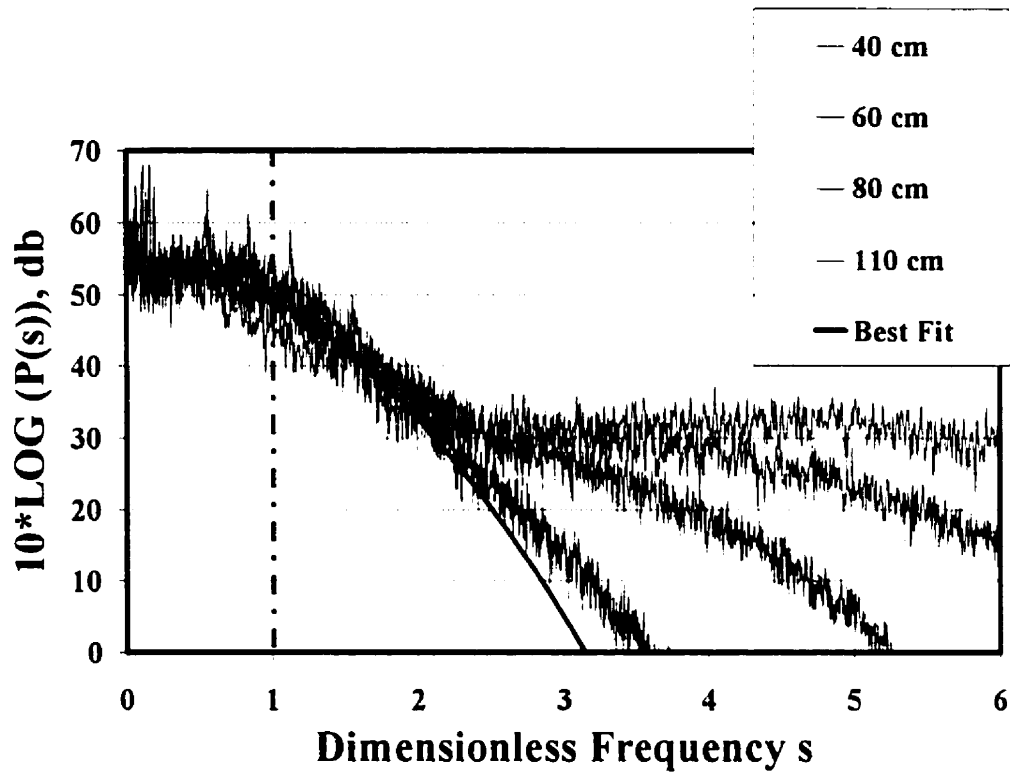


Figure 46. The dimensionless power spectra of the lift force exerted on 1.9-cm cylindrical deposit at different distances (best fit: $p(s) = 316228 \cdot \exp(-s^2 (0.89^2))$).

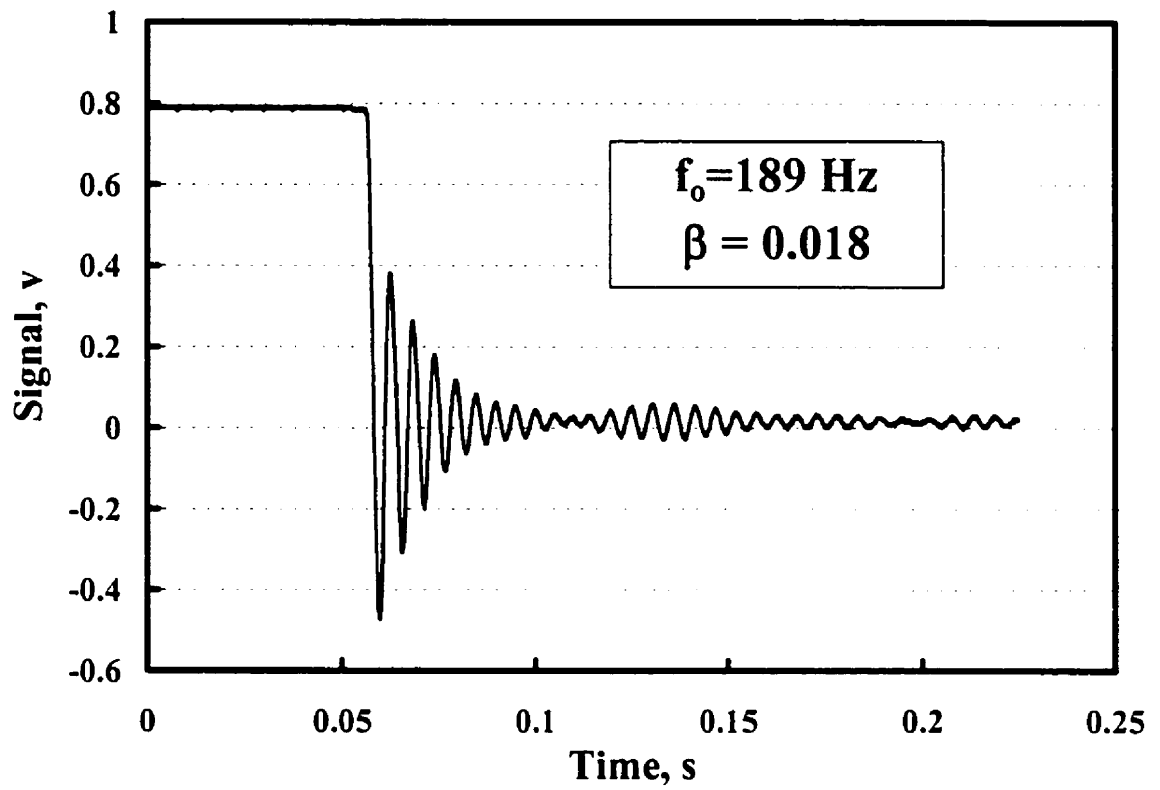


Figure 47. Free vibrations of the torque meter experimental apparatus with type A model deposit (first natural frequency $f_0=189 \text{ Hz}$ and $\beta = 0.018$).

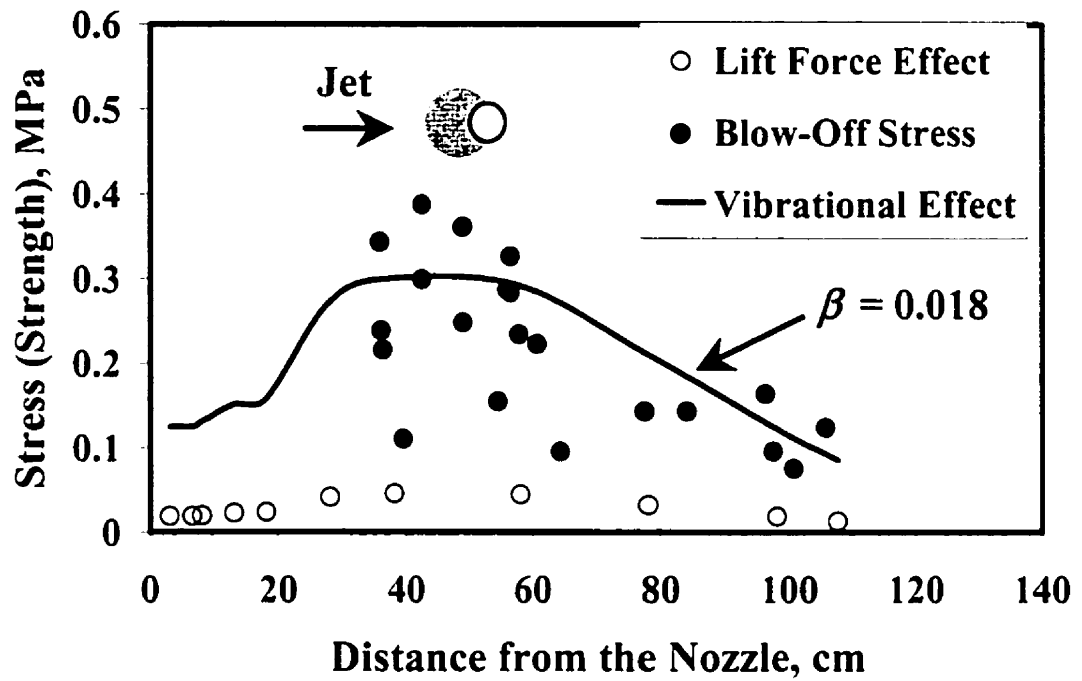


Figure 48. Comparison between the estimated effect of maximum vibration amplification on the stress generated by the lift force and the blow-off data.

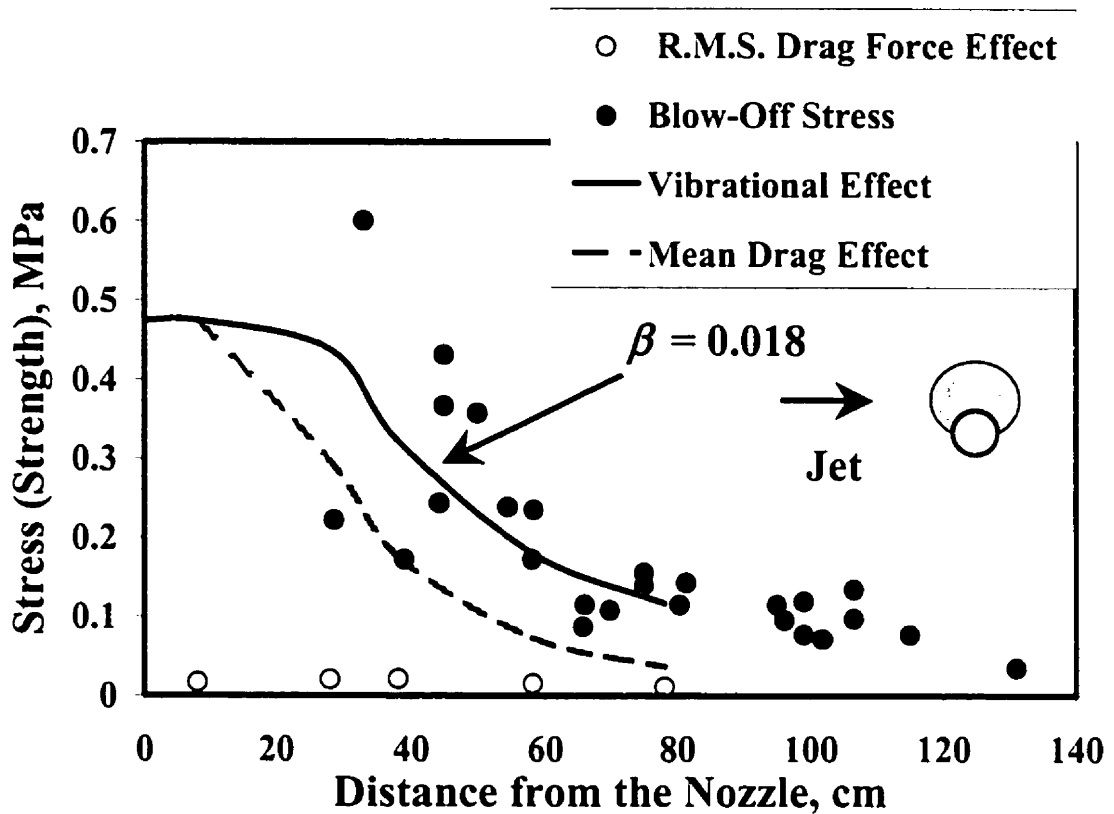


Figure 49. Comparison between the estimated effect of the maximum vibration amplification on the stress generated by the drag force and the blow-off data:
Mean Drag Effect: stress generated due to the Mean Drag Force.
Vibrational Effect: stress generated by the drag force by taking into account the maximum amplification of drag fluctuations due to the flow-induced vibrations (force: mean drag + amplified drag force fluctuations due to vibrations).
R.M.S. Drag Force Effect: Stress generated by R.M.S. of drag fluctuations.
In the Vibrational Effect and Mean Drag Effect stress calculations, the r.m.s of lift fluctuations as lateral forces are taken into account (Equation (19), combined stress).

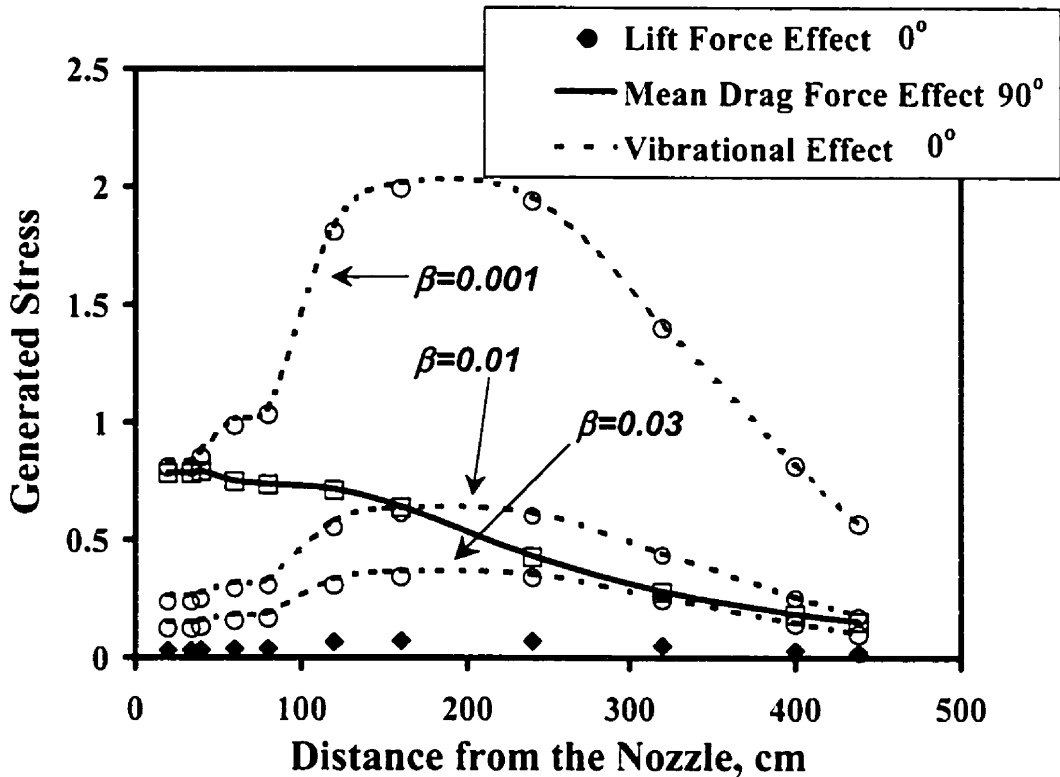


Figure 50. The comparison between the maximum stress generated at the 90° and 0° attack angle orientations at the tube-deposit interface of a 15.2-cm (6-inch) thick deposit in a recovery boiler. The effect of lateral flow-induced-vibrations for the 0° attack angle orientation and damping coefficients, $\beta=0.03$, 0.01 and 0.001 is shown by dashed curves. Curves represent the data calculated by using Equation (15). The data shown by “o” and “□”, represent the maximum stress calculated by Equation (19)(combined stress).

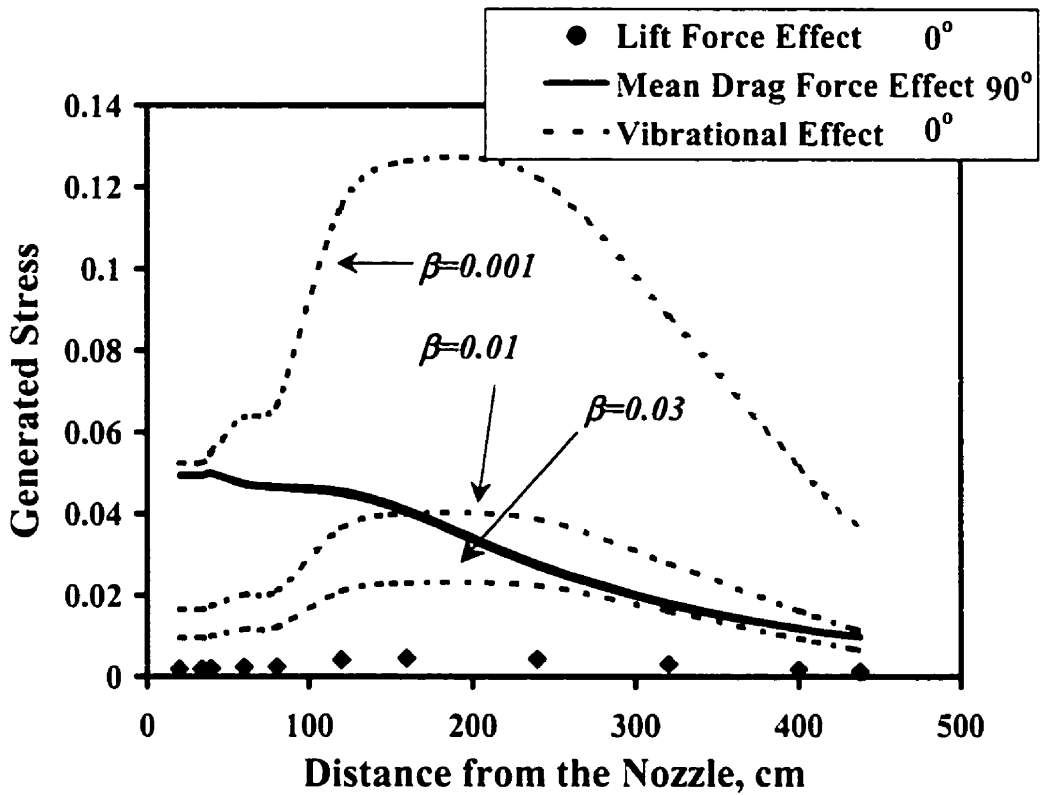


Figure 51. The comparison between the maximum stress generated at the 90° and 0° attack angle orientations at the tube-deposit interface of a 5-cm (2-inch) thick deposit in a recovery boiler. The effect of lateral flow-induced-vibrations for the 0° attack angle orientation and damping coefficients, $\beta=0.03$, 0.01 and 0.001 is shown by dashed curves. Curves represent the data calculated by using Equation (19) (combined stress).

APPENDICES

APPENDIX A¹:

ELASTIC ANALYSIS OF THE DEPOSIT

In order to estimate conditions for deposit removal by a debonding mechanism, consider a piece of solid deposit, covering front side of a tube in a sector $\pm\alpha_0$ of the tube circumference (Figure 7). Moments and forces, produced by a sootblower on the deposit, cause stresses at the tube-deposit interface. The outer layers of a deposit may be very hard and strong in comparison with the inner layer. Therefore, if a deposit is removed by debonding, the adhesion layer should be weaker than the bulk of deposit. As a reasonable approximation, the bulk of solid deposit may be considered as absolutely rigid and the weaker layer at the interface as a deformable material. In this case, the forces affecting the deposit cannot deform the bulk of the deposit, but can cause its small displacement with respect to the tube. This displacement may be presented as a combination of a rotation with respect to the tube axis by some small angle ϕ and a translation by small distance Δ .

¹ This analysis was done by Dr. Andrei Kaliazine, and was published in Appendix A in reference [31].

If the thickness of the elastic adhesion layer is δ , then, from purely geometrical considerations, the strain deformation components in the layer which are caused by rotation are:

$$\begin{aligned} \varepsilon_{rr} &= 0 \\ \varepsilon_{r\theta} &= \varepsilon_0 \end{aligned} \quad \text{where} \quad \varepsilon_0 = \frac{\phi}{\delta} R \quad (\text{A1})$$

where ε_{rr} and $\varepsilon_{r\theta}$ are the strain deformation components.

Similarly, the strain deformation components, caused by the translational displacement in the transverse direction are:

$$\begin{aligned} \varepsilon_{rr} &= -\varepsilon_1 \sin \alpha \\ \varepsilon_{r\theta} &= \varepsilon_1 \cos \alpha \end{aligned} \quad (\text{A2})$$

$$\varepsilon_1 = \frac{\Delta}{\delta}$$

The stress and the strain are related by the general stress-strain relationships:

$$\begin{aligned} \sigma = \sigma_{rr} &= (2G + \lambda)\varepsilon_{rr} + \lambda(\varepsilon_{\theta\theta} + \varepsilon_{zz}) \\ \tau = \sigma_{r\theta} &= G\varepsilon_{r\theta} \end{aligned} \quad (\text{A3})$$

where $\varepsilon_{\theta\theta}$ and ε_{zz} are the strain deformation components, $\sigma = \sigma_{rr}$ and $\tau = \sigma_{r\theta}$ are the stress components, G is called the shear modulus of elasticity and λ is called Lamé's constant.

These constants are related to the Young's modulus E and Poisson's ratio ν as follows:

$$G = \frac{E}{2(1+\nu)}, \quad \lambda = \frac{E\nu}{2(1+\nu)} \quad (\text{A4})$$

According to (A3), strain deformation components (A2) and (A1) cause the following stresses in the adhesion layer:

$$\begin{aligned} \sigma = \sigma_{rr} &= -G(2+\nu)\varepsilon_1 \sin \alpha \\ \tau = \sigma_{r\theta} &= G(\varepsilon_0 + \varepsilon_1 \cos \alpha) \end{aligned} \quad (\text{A5})$$

If a sootblower jet, when it hits the deposit, produces a transverse force F and moment M , (F and M stand for linear density of force and moment) then from the conditions of equilibrium:

$$\begin{aligned} M &= R^2 \int_{-\alpha_0}^{\alpha_0} \tau d\alpha \\ F &= -R \int_{-\alpha_0}^{\alpha_0} \sigma \sin \alpha d\alpha + R \int_{-\alpha_0}^{\alpha_0} \tau \cos \alpha d\alpha \end{aligned} \quad (\text{A6})$$

Substituting equations (A5) into (A6) we get:

$$\begin{aligned} \frac{M}{2R^2} &= G\varepsilon_0\alpha_0 + G\varepsilon_1 \sin \alpha_0 \\ \frac{F}{2R} &= G\varepsilon_0 \sin \alpha_0 + G\varepsilon_1 \left((3+\nu)\frac{\alpha_0}{2} - (1+\nu)\frac{\sin(2\alpha_0)}{4} \right) \end{aligned} \quad (\text{A7})$$

From these equations the coefficients of deformation ϵ_0 and ϵ_1 can be determined. The distributions of radial and shear stresses along the tube-deposit interface can then be calculated using (A5):

$$= \frac{F}{R} (2 + \nu) \sin \alpha \frac{\frac{M}{FR} \sin \alpha_0 - \frac{\alpha_0}{2}}{\alpha_0 \left((3 + \nu) \frac{\alpha_0}{2} - (1 + \nu) \frac{\sin(2\alpha_0)}{4} \right) - 2 \sin^2 \alpha_0} \quad (\text{A8})$$

$$\tau = \frac{F}{R} \frac{\frac{M}{FR} \left((3 + \nu) \frac{\alpha_0}{2} - (1 + \nu) \frac{\sin(2\alpha_0)}{4} - \sin \alpha_0 \cos \alpha \right) + \frac{\alpha_0 \cos \alpha}{2} - \sin \alpha_0}{\alpha_0 \left((3 + \nu) \frac{\alpha_0}{2} - (1 + \nu) \frac{\sin(2\alpha_0)}{4} \right) - 2 \sin^2 \alpha_0}$$

Analysis of these equations shows that stress distribution at the interface is a function of the angle α , which depends on two dimensionless parameters α_0 and FRM :

$$\sigma_{\max} = \frac{\sigma}{2} + \sqrt{\left(\frac{\sigma^2}{4} + \tau^2 \right)} \quad (\text{A9})$$

or

$$\sigma_{\max} = \frac{F}{R} \psi_{\max}(\alpha_0, M / FR) \quad (\text{A10})$$

The parameter α_0 defines which part of the tube is covered with deposit; parameter FRM characterizes the external forces applied to the deposit. The latter parameter is generally

about 1 for relatively thin deposit layers because the bulk of a thin deposit is located at the distance R from the tube axis. This parameter becomes larger for thicker deposits. An example of the calculated stress distribution is shown in the Figure A2 for the case $2\alpha_\eta=180^\circ$ (half of the tube circumference is covered with deposit) and $FM/R=2$. The maximum tensile stress is generated at the edge of the deposit and is about $\sigma=1.5F/D$, that is about 2 times smaller than maximum stress at a flat interface (shown for comparison in Figure 8 by a dashed line).

Now consider the case when F is exerted on the deposit along the jet axis (in this case F is the drag force): The displacement may be presented as simply a translation by small distance η . In this case equation A2 becomes:

$$\begin{aligned}\varepsilon_{rr} &= \varepsilon_2 \cos \alpha \\ \varepsilon_{r\theta} &= -\varepsilon_2 \sin \alpha \\ \varepsilon_2 &= \frac{\eta}{\delta}\end{aligned}\tag{A11}$$

Similarly equations (A.5) and (A.6) become:

$$\begin{aligned}\sigma = \sigma_{rr} &= G(2 + \nu)\varepsilon_2 \cos \alpha \\ \tau = \sigma_{r\theta} &= -G\varepsilon_2 \sin \alpha\end{aligned}\tag{A12}$$

$$F = R \int_{-\alpha_0}^{\alpha_0} \sigma \cos \alpha \, d\alpha + R \int_{-\alpha_0}^{\alpha_0} \tau \sin \alpha \, d\alpha\tag{A13}$$

Substituting equations (A.12) into (A.13):

$$F = RG\varepsilon_2 \left((3 + \nu)\alpha_0 + (1 + \nu)\frac{\sin 2\alpha_0}{2} \right) \quad (\text{A14})$$

The stresses become:

$$\sigma = \frac{F}{R} \frac{(2 + \nu) \cos \alpha}{\left((3 + \nu)\alpha_0 + (1 + \nu)\frac{\sin 2\alpha_0}{2} \right)}$$

$$\tau = \frac{F}{R} \frac{\sin \alpha}{\left((3 + \nu)\alpha_0 + (1 + \nu)\frac{\sin 2\alpha_0}{2} \right)} \quad (\text{A15})$$

The principal stress can be calculated again from equation (A9).

In case that both of these forces are exerted on the deposit, the combined principal stress can be calculated:

$$\sigma_{\max} = \frac{\sigma_L + \sigma_D}{2} + \sqrt{\left(\frac{\sigma_L + \sigma_D}{2}\right)^2 + (\tau_L + \tau_D)^2} \quad (\text{A16})$$

where the subscripts L and D represent the stresses generated by the lateral and axial (Drag) forces, respectively.

APPENDIX B:

CALCULATION OF JET PEAK IMPACT

PRESSURE BASED ON NOZZLE

CHARACTERISTICS

The peak impact pressure (PIP) of the jet can be calculated based on the nozzle characteristics and the distance from the deposit [13]. The axial profiles of velocity V_x and enthalpy H_x for a fully expanded axisymmetric jet have been calculated and confirmed experimentally [39]:

$$\frac{V_x}{V_e} = 1 - \exp \left(\frac{-1}{\left\{ \left(k_v \frac{x}{r_e} \sqrt{\frac{\rho_\infty}{\rho_e}} \right) - 0.7 \right\}} \right) \quad (\text{B1})$$

$$\Delta H = \frac{H_x - H_\infty}{H_e - H_\infty} = 1 - \exp \left(\frac{-1}{\left\{ \left(k_h \frac{x}{r_e} \sqrt{\frac{\rho_\infty}{\rho_e}} \right) - 0.7 \right\}} \right) \quad (\text{B2})$$

where k_v and k_h are the coefficients for turbulent transfer of momentum and energy, ρ is the gas density, r_e is the radius of nozzle exit, x is the axial distance along the jet centerline, H is the total enthalpy equal to $h + V^2/2$, and the subscripts e and ∞ represent the exist and ambient conditions, respectively.

The parameters k_v and k_h account for the entrainment of the surrounding fluid. For a supersonic jet with an exit Mach number greater than one ($M_e > 1$), k_h is equal to 0.102 and k_v can be calculated from [39]:

$$k_v = 0.063(M_e^2 - 1)^{-0.15} \quad (\text{B3})$$

The nozzle geometry and the ratio of the area at the nozzle exit A_e to the throat area A_t are the controlling parameters of the exit Mach number:

$$\frac{A_e}{A_t} = \frac{1}{M_e} \left(\left[\frac{2}{1+\gamma} \right] \left[1 + \frac{(\gamma-1)(M_e^2)}{2} \right] \right)^{\frac{\gamma+1}{2(\gamma-1)}} \quad (\text{B4})$$

where $\gamma = C_p / C_v$ is the ratio of the gas specific heat at constant pressure, C_p , to gas specific heat at constant volume C_v .

Equation (B2) can be written in terms of the local temperature, T_x , at the jet centerline by using the relation between the enthalpy and temperature ($dH = C_p dT$):

$$T_x = T_\infty - [\Delta H(T_e - T_\infty)] + \left\{ \frac{V_e^2}{2C_p} \left(\Delta H - \left(\frac{V_x}{V_e} \right)^2 \right) \right\} \quad (\text{B5})$$

where V_x is the local axial velocity from equation (B1).

The local Mach number, M_x , can be calculated from:

$$M_x = \frac{V_x}{(\gamma R T_x)^{0.5}} \quad (\text{B6})$$

where R is the gas constant.

For a fully expanded jet $\rho_x = \rho_e$, therefore, for $M_x < 1$, the PIP at any axial location, P_{ax} , can be calculated based on the ambient pressure P_∞ :

$$\frac{P_{ax}}{P_\infty} = \left(1 + \frac{(\gamma - 1)M_x^2}{2} \right)^{\frac{\gamma}{\gamma - 1}} \quad (\text{B7})$$

For $M_x > 1$, a normal shock wave appears in front of the nozzle, and reduces the optimum PIP to a value equal to P'_{ax} :

$$\frac{P'_{ax}}{P_\infty} = \left[\frac{\frac{(\gamma + 1)M_x^2}{2}}{\left(1 + \frac{(\gamma - 1)M_x^2}{2} \right)^{\frac{\gamma}{\gamma - 1}}} \right] \left[\left(\frac{2\gamma M_x^2}{\gamma + 1} \right) - \left(\frac{\gamma - 1}{\gamma + 1} \right)^{\frac{-1}{\gamma - 1}} \right] \quad (\text{B8})$$

Therefore, for a fully expanded jet, the PIP at any location along the jet axis can be calculated by solving equation (B1) and equation (B5) in conjunction with either equation (B7) or (B8), depending on the local Mach number.

To estimate the effective jet diameter D_{ef} at any location along the jet axis, the jet integral momentum equation can be used:

$$\int_0^{\infty} 2\pi r_x \rho_x V_x^2 dr_x = M_0 = \frac{\pi D_{ef}^2}{4} \rho_x V_x^2 \quad (B9)$$

where M_0 , ρ_x and r_x are the free jet momentum flux, the gas density and the radial distance at the axial location x from the nozzle, respectively.

The free jet momentum flux M_0 in the axial direction is preserved. That means if M_e is the momentum flux at the nozzle exit, then it is equal at all other sections:

$$M_0 = \frac{\pi D_{ef}^2}{4} \rho_x V_x^2 = M_e = \rho_e \frac{\pi D_e^2}{4} V_e^2 \quad (B10)$$

where ρ_e and D_e are the gas density at the nozzle exit and the nozzle exit diameter.

Therefore, the effective jet diameter D_{ef} at the axial location x from the nozzle can be estimated as:

$$D_{ef} = D_e \frac{V_e}{V_x} \sqrt{\frac{\rho_e}{\rho_x}} \quad (B11)$$